# MEASUREMENT AND MODELING OF THE EFFECTS OF PULSED LASER DEPOSITED COATINGS ON CATHODOLUMINESCENT PHOSPHORS

By

William Joseph Thomes, Jr.

A DISSERTATION PRESENTED TO THE GRADUATE SCHOOL
OF THE UNIVERSITY OF FLORIDA IN PARTIAL FULFILLMENT
OF THE REQUIREMENTS FOR THE DEGREE OF
DOCTOR OF PHILOSOPHY

UNIVERSITY OF FLORIDA

2000

This work is dedicated to the memory of my grandfather,
Gilbert Walter Thorpe,
who passed away in the course of my graduate studies.

## ACKNOWLEDGMENTS

There are so many people whom I wish to thank that it is hard to decide where to begin. First, I would like to thank my fiancée, Cynthia, for her loving support all these years. She has seen me through the ups and downs of graduate school and has always been there to pick me up when I was down or to share in my joy. She also provided invaluable editorial advice and revisions for this dissertation. I would also like to thank my family for their love throughout my life. Even when I was not sure that it was possible to make it all the way to the end, they believed in me and provided the encouragement to stick it out no matter what happened.

Dr. Paul Holloway deserves a special word of thanks for providing guidance during my graduate education. His door was always open, and he never hesitated to discuss my work with me and give me some direction when needed. He is truly one of the greatest teachers that I have been fortunate enough to come across in my educational pursuits.

Special thanks are also due to Dr. Carl Seager and Dr. Dave Tallant for providing me with the opportunity and the funding to come to Sandia National Laboratories to conduct many of my experiments with them. I am especially grateful to Carl, who, in addition to providing me access to all of the equipment in his labs so that I could measure my samples, was a mentor and a friend during my stay in New Mexico. Without his help

and guidance, much of the work contained in this dissertation would not have been possible.

There are many others who made my stay in New Mexico a memorable one. Although I cannot mention them all in the space allotted to me, I would like to point out a few. John Hunter was everything I could have asked for in a friend, and never once did he hesitate to allow me to stay at his house a little longer when I said, "I think they want me to stay one more month." I would also like to thank my many other friends out in New Mexico, including John, Shasta, Jerry, and Shawna. Thanks are due to Jonathan Campbell for sedimenting all of my phosphor screens, helping me learn all the quirks of the lab equipment, introducing me to everyone at the lab, and teaching me about all of the fascinating things that New Mexico has to offer (including green chiles). I'd also like to thank Guild, who always seemed to be in a good mood, for his help with the SEM work.

Many thanks go to those in Florida who have made these past four years memorable ones. I wish to thank the entire Holloway group past and present, especially Billie, Jay, Bo, Chris, Sean, Troy, Loren, Caroline, Bill, Mark, and Ludie (without whom we might all be lost). I am grateful to the following for not only providing me with their friendship, but also for performing measurements on my samples: Eric Lambers for AES measurements, Wish Krishnamoorthy for TEM analysis, and Dr. Kumar for help with the PLD of the coatings used in this work.

I'd also like to thank all of my friends in Cuong Nhu, especially Chi-Wah, who suffered with me for many years under some of the best senseis in the martial arts. I will never find another set of instructors who provide the type of training that I found in Sensei Mark's and Sensei Joyce's classes.

Although I have made every attempt to include all those who deserve acknowledgement in these pages, I am sure that there are some who have not been mentioned. I regret the omission, but after many long days of putting this dissertation into its final form, it's surprising that more of you are not missing. Please know that each of you is appreciated.

TABLE OF CONTENTS

ACKNOWLEDGMENTS ..... iii

ABSTRACT ..... ix

CHAPTERS

1 INTRODUCTION ..... 1

2 LITERATURE REVIEW ..... 5

Introduction ..... 5
Field Emission Display (FED) ..... 6
Cathodoluminescence (CL) ..... 8
Phosphors ..... 14
$Y_2O_3$:Eu ..... 15
$Y_2SiO_5$:Tb ..... 17
Efficiency ..... 18
Charging ..... 19
Cathodoluminescent Degradation ..... 25
Coatings for Phosphors ..... 31
Pulsed Laser Deposition (PLD) ..... 35
Motivation for this Work ..... 38

3 EXPERIMENTAL PROCEDURES ..... 61

Introduction ..... 61
Sedimentation of Phosphor Screens ..... 61
Pulsed Laser Deposition (PLD) of Coatings ..... 63
Characterization Techniques ..... 66
Steady-State Cathodoluminescence ..... 67
Pulsed Cathodoluminescence ..... 69
Ellipsometry ..... 71
Transmission Electron Microscopy (TEM) ..... 74
Auger Electron Spectroscopy (AES) ..... 76
Scanning Cathodoluminescence (CL) in a Scanning Electron Microscope (SEM) ..... 77

4 EXPERIMENTAL RESULTS ..... 88

Introduction ..... 88
Cathodoluminescent Spectra ..... 88
Beam Energy Effects on Luminescence ..... 92
Pulsed Cathodoluminescence ..... 93
Coating Thickness and Uniformity ..... 97

5 MODELING OF RESULTS ..... 174

Introduction ..... 174
Energy Loss in Dead Layer ..... 174
Incident Angle Contributions and Coating Uniformity ..... 177
Path Length of Electrons in the Coating ..... 184
Calculation of the Cathodoluminescence from Coated Phosphors ..... 185
New Energy Loss Equation ..... 188
Backscattering Coefficients ..... 190
Index of Refraction ..... 192

6 DISCUSSION ..... 233

Introduction ..... 233
Initial Uniform Coating Model ..... 233
Validity of the Energy Loss Model ..... 236
Backscattering Coefficient ..... 241
Scattering ..... 242
Surface Recombination and Charging ..... 243
Surface Segregation ..... 244
Surface Roughness ..... 245

7 SUMMARY AND CONCLUSIONS ..... 247

APPENDICES

A MATHCAD DATA AVERAGING PROGRAM ..... 252

B LUMINESCENCE DUE TO THE INCIDENT ANGLE OF THE ELECTRONS ..... 256

C NONUNIFORM COATING SHAPE ..... 260

D STOPPING POWER ..... 263

E MATHCAD PROGRAM FOR MgO (4 min) / $Y_2O_3$:Eu ..... 265

F MATHCAD PROGRAM FOR MgO (8 min) / $Y_2O_3$:Eu ..... 270

G MATHCAD PROGRAM FOR $Al_2O_3$ (1.2 min) / $Y_2O_3$:Eu ..... 275

H MATHCAD PROGRAM FOR $Al_2O_3$ (2.4 min) / $Y_2O_3$:Eu ..... 280

I MATHCAD PROGRAM FOR MgO (4 min) / $Y_2SiO_5$:Tb ..... 285

J MATHCAD PROGRAM FOR MgO (8 min) / $Y_2SiO_5$:Tb ..... 290

K MATHCAD PROGRAM FOR $Al_2O_3$ (1.2 min) / $Y_2SiO_5$:Tb ..... 295

L MATHCAD PROGRAM FOR $Al_2O_3$ (2.4 min equiv.) / $Y_2SiO_5$:Tb ..... 300

M MATHCAD PROGRAM FOR $Al_2O_3$ (5 min) / $Y_2SiO_5$:Tb ..... 305

BIBLIOGRAPHY ..... 310

BIOGRAPHICAL SKETCH ..... 322

Abstract of Dissertation Presented to the Graduate School
of the University of Florida in Partial Fulfillment of the
Requirements for the Degree of Doctor of Philosophy

MEASUREMENT AND MODELING OF THE EFFECTS OF PULSED LASER DEPOSITED COATINGS ON CATHODOLUMINESCENT PHOSPHORS

By

William Joseph Thomes, Jr.

August 2000

Chairman: Dr. Paul Holloway
Major Department: Materials Science and Engineering

Coatings have been shown to reduce the degradation of field emission display phosphors and, in certain cases, improve the low voltage luminescence. To study the energy loss mechanisms in coatings and to predict their impact on cathodoluminescence, coatings of MgO and $Al_2O_3$ were pulsed laser deposited onto sedimented screens of $Y_2O_3$:Eu and $Y_2SiO_5$:Tb. The thickness of the pulsed laser deposited coatings (which were characterized by ellipsometry, transmission electron microscopy, and Auger electron spectroscopy sputter profiles) were varied from 7.5 to 50 nm by changing the deposition time and oxygen background pressure. A Si shadow mask was used to cover half of the sedimented powder during deposition. This allowed for comparison of coated with uncoated powder that experienced the same processing. Cathodoluminescence data were collected for beam energies from 0.8 to 4 keV at a constant current density of 0.16 $\mu A/cm^2$.

The coating thickness on the particles was modeled by assuming a uniform deposition flux over a spherical powder surface. Spatially resolved electron energy loss was calculated to predict the cathodoluminescence intensity versus beam energy and incident angle relative to the local surface normal. A modified Bethe stopping power equation was initially used to predict the luminescence from the coated phosphors. This was found to overestimate the attenuation of the luminescence at beam energies below about 3 keV. To provide a more accurate fit to the low energy region, a new energy loss equation based on a form similar to a Makhov power loss equation was introduced. By using the new energy loss equation, the cathodoluminescence intensity of the coated phosphors could accurately be predicted for all energies up to 4 keV.

The model developed in this work was used to fit luminescence losses from as low as 4.71% (at 4 keV) for a 10 nm coating of $Al_2O_3$ on $Y_2O_3$:Eu to as large as 27.4% (at 4 keV) for a 43 nm MgO coating on $Y_2SiO_5$:Tb. No change in the surface recombination rate was observed. The coatings were also found to have no effect on the decay states under pulsed excitation, except those attributed to beam energy loss.

# CHAPTER 1
# INTRODUCTION

Cathode ray tubes (CRTs) have dominated the visual display market since their invention in the 1920s.[1] However, due to their large size, they are not suitable for use in many modern applications that require compact screens. To fill this role, a class of devices known as flat panel displays (FPDs) has been invented. These displays are very thin in comparison to the CRT, which makes them the ideal display media for portable electronic devices. So far, liquid crystal displays (LCDs) have led the market in the field of FPDs.[2] However, new types of FPDs are being developed to improve upon the LCD. At the forefront of the new FPDs is the field emission display (FED). It offers advantages in terms of its wide operating temperature range, wide viewing angle, fast response time, low power consumption, high brightness, high durability, low weight, and scalability.[2-12] For these reasons, the FED is likely to challenge the LCD for dominance in the FPD market.

The FED excites luminescence from phosphors deposited on a glass faceplate, similar to a CRT. However, unlike a conventional CRT that relies on just three electron guns that create beams that are rastered across the phosphor screen, the FED uses thousands of tiny emitters behind each phosphor pixel. The depth of a CRT is determined by the distance necessary for deflection of the electron beam over the entire screen surface. The FED removes this limitation due to the fact that the emitters are

located directly behind the pixels and can be turned on and off, unlike scanning in the CRT, in which the electron gun is continuously on. Therefore, the device can be made very thin (the typical spacing between the emitter array and phosphor screen is around 10 mm).

The proximity of the emitters to the pixels also allows much lower voltage to be used in the FED (4 or 5 keV, compared to 25 keV in a CRT). The problem with using a lower voltage, however, is a reduction in the luminescence intensity from the phosphors. To counteract this loss in intensity, the current from the emitters is increased. The increased current helps regain the lost luminescence, but it also leads to more rapid degradation.[13]

Due to the operating conditions of FEDs (low voltages and high currents), phosphor degradation is one of the limiting factors in the lifetime of the device. Coatings have been shown to greatly improve the degradation resistance of the phosphors.[14] One of the drawbacks to using coatings is that they also cause a reduction in the cathodoluminescence from the phosphor. Under certain circumstances, however, coatings have been shown to improve the low-voltage efficiency of phosphors.[15] If the efficiency of the phosphors is increased at low voltages, then the power consumption of the device and the rate of degradation can be reduced.

The focus of this work has been on examining the effects on cathodoluminescence of wide-bandgap oxide coatings, specifically MgO and $Al_2O_3$, deposited by pulsed laser deposition onto two commercially available phosphors, $Y_2O_3$:Eu and $Y_2SiO_5$:Tb, used in FEDs. A review of the literature available on selected aspects of the cathodoluminescent process is given in Chapter 2. Also included in the chapter is a discussion of the

mechanisms behind the degradation process and how the use of coatings can slow or eliminate this loss. Near the end of the chapter, the characteristics and merits of pulsed laser deposition are presented, along with the reason for choosing this technique to deposit the coatings.

The experimental procedures used to deposit the coatings and collect the cathodoluminescence from the phosphors are discussed in Chapter 3. This chapter also includes a description of ellipsometry, transmission electron microscopy, Auger electron spectroscopy, and scanning electron microscopy, all of which were used to characterize the coatings.

Results of the cathodoluminescent measurements on the coated samples showed that the coatings attenuated the luminescence from the phosphors. The effect was larger at lower voltages due to the interaction volume of the electron beam. Thicker coatings were found to produce a larger reduction in the cathodoluminescent intensity. These results are discussed in Chapter 4.

A model was developed to explain the loss in luminescence based on a dead layer approximation. The model relied on calculation of the energy loss of the electron as it travels through the coating. Resultant energy after passing through the coating was then used to find the luminescence. This model allows for calculation of the cathodoluminescence over the entire energy range up to 4 keV. Spatially resolved energy loss was found using a cosine dependent coating based on a uniform deposition flux onto spherical phosphor powders. An improved energy loss equation was incorporated to account for the extended range of the low energy electrons. Calculated results from this model were found to accurately predict the cathodoluminescence from the coated

phosphors for all measured thicknesses. Derivation of the model is given in Chapter 5. A discussion of the applicability of the model is presented in Chapter 6.

The conclusions from this work are given in Chapter 7. Appendices A through M contain the various Mathcad programs used during the calculations.

# CHAPTER 2
# LITERATURE REVIEW

## Introduction

Electronics have become an ever-increasing part of everyday human life. The ability to process information is continually advancing as new and faster ways of computing are developed. One important aspect of this trend is the ability of the machine to transmit data to a human operator. Shown in Figure 2-1 are the many different means of interfacing between a computer and a person. It can clearly be seen that visual communication is currently one of the fastest means of data transfer, at around 300 Mb/sec. Many different types of visual signal media can be used to accomplish this goal.

Historically, cathode ray tubes (CRTs) have dominated the visual display market. However, new types of displays have recently evolved. Most of these new technologies have been designed to serve a more specific purpose that allows them to compete with the CRT. For example, the development of smaller, more portable electronic devices created a need for compact screens. Liquid crystal displays (LCD) have filled this role thus far, with a 90% market share in 1995.[2] However, in demanding applications such as military uses, medical instruments, vehicles, and dusty environments, to name a few, the weaknesses of the LCD (one of which is its inability to operate over wide temperature ranges) can have severe consequences. It is in these areas that new devices are being developed to challenge the dominance of the LCD. All of these new devices can be

lumped under the general heading of flat panel displays (FPDs) because of their slim profile when viewed from the side. Each type of display has certain advantages and disadvantages when used for different applications. Table 1 lists the various FPDs and some of the attributes of each. Portable applications are not the only market for FPDs; their strengths over other visual media will allow them to compete in all arenas of display technology, from tiny head-mounted displays to huge billboard-size screens.

Among the various types of FPDs, field emission displays (FEDs) offer many advantages, such as wide viewing angle, fast response time for video refresh rates and "instant-on" capability, low power consumption, high brightness, durability, wide operating temperature range, low weight, and scalability to a larger size. Each of these attributes makes FEDs desirable for a wide variety of applications.[2-12]

## Field Emission Display (FED)

Cathode ray tubes (CRTs), the displays found in all conventional televisions, rely on cathodoluminescence for their operation. Figure 2-2 shows the basic design of a CRT. An electron gun accelerates electrons toward a phosphor screen. These electrons are deflected by means of plates or magnetic fields and are then raster scanned across the screen. Red, green, and blue phosphors are deposited on the screen in small holes known as pixels. (Actually, each hole that contains a single color phosphor is called a subpixel. Three subpixels together, one of each color, make up a pixel.) In a full color display, three separate guns are used, each specific to an individual color.

One of the biggest problems with CRTs is their depth, which is needed in order to have sufficient distance of travel for deflection of the 20 keV electron beams across the

entire screen. FEDs remove this size restriction by using thousands of individual electron sources behind each subpixel. Figures 2-3 and 2-4 show typical FED setups. Electrons are extracted from very sharp tips by tunneling when high fields are present. These electrons are then accelerated toward the faceplate, which contains the phosphors. The emitter tips are usually located only about 10mm away from the phosphor screen, thus allowing the display to be extremely thin.

Emitter arrays can consist of up to thousands of tips per pixel. They are usually made from molybdenum, tungsten, platinum, or silicon[2], although carbon has recently been found to be an effective cathode material as well. Carbon emitters are not grown like traditional tips and are either diamond thin films or are in the form of nanotubes.[4, 12, 16-18] Regardless of the type of material chosen for the emitters, electron extraction from the tip is carried out in the same fashion. By applying an appropriate bias, dependent upon the type of material and the specific device setup, electric fields can be generated to cause tunneling of electrons out of the tip. This process is accurately described by the Fowler-Nordheim tunneling theory for electrons.[6, 7, 9, 19-21] Figure 2-5 depicts the field with and without applied bias. As can be seen from the picture, with an applied bias, the potential energy barrier on the surface has been reduced in height and has a finite width. The applied field is magnified at the tip because of its extreme sharpness (its radius is approximately 50 nm). This results in more tunneling current at lower voltages. Due to the finite barrier and large effective fields near the surface, it is possible for the electrons to quantum mechanically tunnel out of the tip and enter the vacuum as field-emitted electrons.[22] For a more detailed discussion of the use of the Fowler-Nordheim equation and suggestions for improving the description of electron

emission from sharp tips, the reader is referred to the previously-cited paper by Cutler and associates.[19]

One of the challenges faced in applying this technology in a commercial flat panel display is achieving uniform emission from the thousands of tips. To combat the problem of nonuniform emission, resistors have been fabricated in series with the tips to help control tip-to-tip nonuniformity in current.[23] This has provided a partial solution to the problem, but it is not a perfect solution. The best method would be to fabricate a constant-current source to the tip to regulate current more effectively. A group from Japan has reported doing this using silicon tips grown as part of a metal-oxide-semiconductor field-effect-transistor (MOSFET structure).[23] Using such a device structure allows for uniform and precise control of electron emission. With these advances in cathode technology, research attention is shifting to the improvement of other aspects of the FED.

The phosphor screen is an integral part of the FED. In terms of the phosphors, some of the hurdles that still need to be overcome in order to realize a commercially viable full color display include: better low voltage efficiency, enhanced chromaticity, reduced saturation, and lower degradation.[3]

## Cathodoluminescence (CL)

When some materials are impacted with certain forms of energy, they will emit photons in excess of thermal radiation. This process is known as luminescence, and it can be categorized based on the type of excitation source. These categories include photoluminescence, cathodoluminescence, chemiluminescence, triboluminescence, X-ray

luminescence, and electroluminescence, among others.[24, 25] Photoluminescence refers to excitation by photons, usually from a UV lamp. Cathodoluminescence is excitation from a beam of energetic electrons, also known as cathode rays. Chemiluminescence results from energy released during a chemical reaction. Triboluminescence is a result of mechanical energy, such as friction or fracture, and can also be seen during processes such as grinding. X-ray luminescence comes from X-ray excitation, as the name suggests. Finally, electroluminescence is produced by an electric field resulting from an applied voltage across the material. It should be noted however, that thermoluminescence does not refer to thermal excitation from the ground state. Instead, this term is used to describe the thermal stimulation of electrons from excited state traps that can then recombine and produce luminescence. The applied heat does not actually excite the electrons; this occurred during a prior excitation event. Rather, the heat only gives the electrons the energy needed to surmount the energy barrier holding them in the trapped state.[25]

In addition to the characterization of luminescence based on the different types of excitation, there is a distinction made according to the length of the delay between the excitation and emission of photons. Materials can exhibit either fluorescence or phosphorescence. "Fluorescence" is the term used when the emission of photons occurs within about $10^{-8}$ seconds after excitation. "Phosphorescence" pertains to any material that displays luminescence for longer than this. These phosphorescent materials are called phosphors, and they can display luminescence lifetime ranging from $10^{-7}$ seconds to hours after the excitation source is removed.[24]

Phosphors have many technologically important roles, especially in the display industry. They are responsible for converting incident electrons into light in devices such as CRTs and FEDs. However, their luminescent decay rate must be considered in determining their suitability in a particular application. In a display, the phosphor must continue to luminesce long enough to display an image, but also extinguish quickly enough to allow for fast video refresh rates. This is accomplished by choosing suitable phosphor materials and processing, which allows the decay time of the phosphor to be tailored.[26] This is not usually a concern because most phosphors display a suitable response time without any special processing. However, in applications such as the new high-definition TVs, in which very fast video refresh rates are needed, the decay times of various phosphors under different types of processing will need to be taken into consideration.

When an electron beam enters a solid, it will undergo collisions with the host atoms. These collisions are either elastic or inelastic. During elastic collisions, the incident electron interacts with a nucleus of the atom and is deflected with little or no energy loss. If the electron is deflected back toward the surface, it can be lost from the solid as a backscattered electron. Inelastic collisions involve interaction between the incident electron and the electrons of the atom. In these collisions, the incident electron loses part of its energy to the atom. When the electrons in an atom return from the excited state to their ground state, a host of signals can be produced. Among them are Auger electrons, X-rays, secondary electrons, photons, and phonons (thermal effects such as electroacoustic signals).[24] For this study, the generated photons (cathodoluminescence) are of primary interest.

The incremental energy lost (dE) over a distance of travel (ds) due to an inelastic collision can be found from the Bethe equation[14, 24, 27-30]:

$$\frac{dE}{ds} = \frac{-785\rho Z}{A * E} \ln\left(\frac{1.166E}{J}\right) \qquad [2.1]$$

where A is the atomic weight in g/mol, Z is the atomic number, E is the electron energy, $\rho$ is the density in g/cm$^3$, and J is the mean ionization potential in eV. The latter is the average energy loss per interaction (for all possible energy loss processes), and for $Z > 13$ it can be expressed as:

$$J = 9.76Z + \frac{58.5}{Z^{0.19}}. \qquad [2.2]$$

These equations have been shown to be accurate for $E > 6.34$ multiplied by the mean ionization potential.[14, 24, 28-30] Below this energy, the modification by Rao-Sahib and Wittry needs to be considered[30]:

$$\frac{dE}{ds} = \frac{-785 * \rho * Z}{1.2588 * A * \sqrt{E * J}}. \qquad [2.3]$$

This equation corrects for the low energy region while mimicking the behavior of the original Bethe equation at high energy. This new equation can be used for energies as low as approximately 500 V. Attempting to reduce this limit even further, Joy and Luo suggested a new expression for the mean ionization potential using an energy dependent term[14, 29, 31]:

$$J' = \frac{J}{1 + k\left(\frac{J}{E}\right)} \qquad [2.4]$$

where J' is the new mean ionization potential, J is still the average energy loss per interaction, and k is a fitting parameter. The constant k varies from 0.7 to 0.9, but it is usually around 0.85.

The stopping power equations cited above provide a measure of how the electrons lose energy in the solid, but they do not give an accurate indication of the interaction volume. During the electron's trip through the lattice, it will also undergo elastic collisions. These will not result in an energy loss, but rather will lead to a change in the direction of the electron's travel. Equation 2.1 can be integrated to find the length of an individual electron "random walk" trajectory. This is known as the Bethe range. However, the interaction volume will be much smaller due to scattering. Typically, the interaction volume is known as the Gruen, electron beam, or penetration range. It can be expressed as:

$$R_e = \left(\frac{k'}{\rho}\right) E_0^{\alpha} \qquad [2.5]$$

where $\rho$ is the density, $E_0$ is the electron beam energy, $k'$ depends on the atomic number and is a function of energy, and $\alpha$ depends on the atomic number and E. Various equations have been given for the solution to this problem, but the one most widely accepted was proposed by Kanaya and Okayama:

$$R_e = \left(\frac{0.0276A}{\rho Z^{0.889}}\right) E_0^{1.67} \qquad [2.6]$$

measured in μm, where $E_0$ is in keV, A is in g/mol, $\rho$ is in g/cm$^3$, and Z is the atomic number.[24] Figure 2-6 demonstrates how this interaction volume moves deeper into the material as the beam energy is increased.

Every incident electron gives off energy to the lattice in multiple steps. Therefore, it is possible for one electron to generate a multitude of secondary electrons. The number of electron-hole pairs generated per incident electron is known as the generation factor; it can be expressed as:

$$G = \frac{E(1-\gamma)}{E_i} \qquad [2.7]$$

where γ represents the fractional electron beam energy lost due to backscattered electrons. $E_i$ is the ionization energy, the energy needed to form a single electron-hole pair. The ionization energy is related to the bandgap of the material by:

$$E_i = 2.8E_g + M \qquad [2.8]$$

where M is between 0 and 1 eV, depending on the material in question. For a more detailed discussion, the reader is referred to Yacobi and Holt's work on the subject.[24]

Once the incident electron has transferred its energy to the solid, this energy can be used to produce visible light. Luminescence from inorganic phosphors usually takes place at an impurity, which is referred to as an activator.[24, 32, 33] However, not all impurities are activators. Those that do not lead to luminescence are referred to as quenchers or killers.[32] Since the activators are an imperfection in the crystal lattice, they will usually exhibit energy levels between those of the conduction and valence bands of the host lattice. These states can become populated either through direct excitation or trapping of secondary electrons generated in the host lattice. When the activator returns to its ground state through recombination of an electron and hole, the energy can be released as luminescence.[24, 25, 32-36] This is known as a radiative transition. When the atom relaxes without the emission of a photon, it is called a nonradiative transition.

Competition between these two types of transitions determines the intensity of the emitted light.[25]

When an electron and hole radiatively recombine, the emitted photon will be characteristic of the energy levels involved, which is determined by the electronic states of the activator. The photon energy (hν) is given by:

$$h\nu = E_f - E_i \qquad [2.9]$$

where $E_f$ and $E_i$ are the energy of the final and initial states, respectively. In the literature on the subject, this energy is often referred to instead by its wavelength equivalent. There is a simple relation relating the two:

$$\lambda \cong \frac{1.2398}{E} \qquad [2.10]$$

where E is the photon energy in eV and λ is in μm.[24, 36] For most materials, the recombination of the electron and hole will be the rate- limiting step to the luminescent process.[37]

**Phosphors**

Phosphors are responsible for converting incident energy into photons (light). Without them, visual display media would not be possible. There are a plethora of different materials that exhibit this behavior. The following is only a partial list of phosphors that can be used to generate the three primary colors (red, blue, and green) of a common display. For red light, there are $Y_2O_2S$:Eu, $Y_2O_3$:Eu, CaS:$Eu^{2+}$, SrS:$Eu^{2+}$, and $YVO_4$:Eu. For green light, there are ZnS:Cu:Au:Al, $Zn_2SiO_4$:Mn, $Y_2SiO_5$:Tb, $Gd_2O_2S$:Tb, $La_2O_2S$:Tb, ZnO:Zn, $Y_3(Al,Ga)_5O_{12}$, $Y_2GeO_5$:Pr, $Y_2O_2S$:Pr, $ZnGa_2O_4$:Mn, $Y_3Al_5O_{12}$:Ce, and $SrGa_2S_4$:Eu. For blue light, there are ZnS:Ag:Cl, $Zn_2SiO_4$:Ti,

$Y_2SiO_5$:Ce, $ZnGa_2O_4$, and $SrGa_2S_4$:Ce.[3, 38] For this work, $Y_2O_3$:Eu and $Y_2SiO_5$:Tb were chosen to be representative of the red and green groups, respectively. This allowed for examination of not only the coating effects, but also the consequences of the underlying host material. The attributes of each will be discussed below.

**$Y_2O_3$:Eu**

$Y_2O_3$:Eu shows a main emission peak in the visible spectrum at 611 nm (red) under cathodoluminescent excitation. This results from a $^5D_0 - {}^7F_2$ transition of the $Eu^{+3}$ site.[25, 39-43] Figure 2-7 shows such a transition. Eu is a rare earth ion and is characterized by an incompletely filled 4f shell. The $4f^6$ shell is shielded by the filled $5s^2$ and $5p^6$ shells.[25, 41] Shielding allows the Eu ion to retain its atomic character and have energy levels close to that of a free ion.[25, 44] As a result, the emission is very sharp at the transmission wavelength.[44] This is also the reason that Eu is usually able to keep its characteristic luminescence, regardless of the host material. There are two possible crystallographic configurations for the Eu atoms, either $C_2$ or $C_{3i}$.[39-41] Figure 2-8 shows these. The main emission from the phosphor is due to transitions in the $C_2$ sites. Energy absorbed into the $C_{3i}$ sites is effectively transferred into the $C_2$ site for recombination.[40] In the literature, $C_{3i}$ symmetry is often referred to as $S_6$ symmetry.[39]

Of importance in the $Y_2O_3$ host is the charge transfer to the luminescent center. The highest occupied levels of the ground state in the host lattice are the 2p orbitals of oxygen, while the lowest unoccupied levels are a mixture of the 3s orbitals of oxygen and the 4d orbitals of yttrium. When electrons are promoted to an excited state under electron bombardment, they can be transferred into the $^5D$ levels of Eu.[25] The configurational

coordinate diagram can be used to represent such a transition. For a fixed central atom, the diagram represents the potential energy (E) curves of the atom as a function of the distance between it and its neighbors (R). Figure 2-9 shows such a diagram. The solid lines in the figure represent the ground states and excited states of the activator, while the dashed line represents another excited state of the activator known as the charge-transfer state. The parabolic shape results from the assumption that the restoring force on the neighboring atoms is proportional to their displacement from equilibrium. The charge-transfer state is one which excited electrons can easily be fed into because of allowed transitions from the ground state of the activator or from the host lattice. The luminescent state is not directly accessible because the transitions are forbidden. In Figure 2-9 (a), the minimum in the charge-transfer band causes excited electrons to be effectively transferred into the luminescent states. This is the case for $Y_2O_3$:Eu. If, however, the charge-transfer band had a minimum located closer to the ground state bands, as shown in Figure 2-9 (b), then excited electrons would be effectively transferred into the ground state through nonradiative relaxation. Due to the location of the charge-transfer band in $Y_2O_3$:Eu, excited electrons populate the luminescent states, giving this phosphor its high quantum efficiency.[45]

The efficiency of different FED phosphors are shown in Table 2.[2] $Y_2O_2S$:Eu has a larger efficiency than $Y_2O_3$:Eu, but it has other disadvantages in terms of degradation that make it a less desirable material for FED applications.[14]

**$Y_2SiO_5$:Tb**

$Y_2SiO_5$:Tb is a green phosphor with a main emission at 538 nm.[46] This is a result of a $^5D_4$-$^7F_5$ electron transition on the $Tb^{3+}$ site, as shown in Figure 2-7. The other three peaks seen in a typical Tb-doped spectrum are the result of transitions to the other $^7F_n$ states.[47] As with the Eu atom in yittria, the Tb in $Y_2SiO_5$ is well shielded by electrons in the outer shells. In a similar fashion, this usually makes the resulting spectrum invariant to host lattice composition.[44, 48] It also makes the transitions exhibit little spread in the emitted wavelength.[44] Also similar to $Y_2O_3$:Eu, $Y_2SiO_5$:Tb has a charge-transfer band that efficiently deposits excited electrons into the luminescent states, as shown in Figure 2-9 (a). In the $Y_2SiO_5$:Tb system, this is the $4f^75d$ band of Tb, and it results in a relatively high quantum efficiency.[25]

One of the properties that makes $Y_2SiO_5$:Tb favorable over other green phosphors is its saturation behavior. In a FED application, as compared to a CRT, lower voltages are used (hundreds to a few thousand volts versus 10 to 20 kV). To regain brightness, higher currents are employed (up to 1000 $A/cm^2$ versus 0.5 $A/cm^2$).[11, 43] Most phosphors will begin to show saturation effects as the current is increased, especially at these low voltages.[3] This is speculated to result from ground state depletion.[49, 50] As the ground state of the activators becomes depleted, the probability of exciting an electron into a luminescent state is reduced. The result is an increase in the nonradiative recombination rate, which leads to a reduction in the efficiency of the phosphor (see section on efficiency in this chapter). However, this is not as prevalent in $Y_2SiO_5$:Tb because of the fast decay rate of the excited state. Because the excited electrons recombine so quickly, they refill the ground state and are thus available for excitation again.[49, 50] Because

$Y_2SiO_5$:Tb shows little or no saturation effects, it is gaining considerable interest in the display market.

## Efficiency

A phosphor is "a solid which converts certain types of energy into electromagnetic radiation over and above thermal radiation."[25] In other words, when an electron beam strikes a phosphor, it can impart some of its energy to exciting electrons into higher energy levels. The rest of the energy is lost in collisions with the host material. The excited electrons can then recombine with a hole in a radiative or nonradiative transition. Radiative transitions give off electromagnetic radiation, whereas nonradiative transitions transfer energy to Auger electrons, ionizations, or phonons.[25]

Efficiency is defined as the brightness per unit of input power and is measured in lumens per watt.[3, 25, 39, 51] In a phosphor, charge transfer to a luminescent center is critical to achieving high efficiency. If the electron and hole are not effectively transferred to the luminescent impurities, then they will have a high probability of recombining nonradiatively. This is one of the major problems in FEDs, where lower voltages are used, as compared to CRTs. As the accelerating voltage is decreased, the efficiency also decreases.[11, 35, 51-53] Table 3 and Figure 2-10 depict this situation. From the table, it is apparent that the reduced efficiency at low voltage is one of the primary disadvantages to FED operation. In order to regain high brightness, larger currents need to be used. These larger currents, in turn, lead to saturation effects and enhanced phosphor degradation and thus short device lifetime.[3]

Many researchers have attempted to devise ways of improving efficiency in this low voltage (under 4 kV) range. One method involved placing the phosphor material directly on top of the gate electrode, as seen in Figure 2-11. Other researchers have tried using quantum confinement to enhance luminescence by spatially confining electrons and holes. This method usually requires phosphor particles smaller than 10 nm in diameter, as compared with the 5 μm phosphors currently in production.[54-59]

The problem with most of the aforementioned approaches is that they tend to be very difficult to implement. The fundamental problem to solve in order to improve efficiency is that of how to transport charge to luminescent centers while decreasing the probability of the charge reaching nonradiative sites. In order to realize this goal, charging in the phosphor during electron bombardment needs to be controlled.

## Charging

Surface recombination refers to the return of excited electrons to the ground state by recombination with an available hole at the phosphor surface. Due to the disruption in the phosphor lattice at the surface, there will be a large number of defects in this region. These defects provide efficient nonradiative pathways for electron-hole recombination. In order to alleviate this problem, surface passivation is often used to regain luminescence. Surface passivation involves coating the surface with another material so that charge is effectively radiated and not allowed to reach the nonradiative surface states.[60-63] These surface states become critical when considering charging of the phosphor. This is especially important in a FED environment, where low voltages are used. As the accelerating voltage of the incident electrons is decreased, the generation of

electron-hole pairs will occur closer to the surface due to the lower penetration of the incident electrons.[50] Figure 2-6 shows a schematic of the electron beam penetration into the phosphor at various beam energies. From the figure, it can be seen that at lower voltages the electrons are localized closer to the surface. Therefore, surface states will have a larger influence on the generated secondary electrons at these lower electron beam voltages.

While surface recombination is possible, other effects can occur upon electron bombardment of phosphors. Yoo and Lee attributed decreased luminescence on the basis of trapped electrons on the surface. They postulate that low energy incident electrons are trapped on the surface. These trapped electrons create an electrostatic potential barrier for subsequent primary electron bombardment and therefore decrease luminescence.[63]

Ozawa further contributes to this explanation with what he calls secondary bound electrons. When an incident electron enters a material, it creates secondary electrons in the near surface region during interaction with the host. If these electrons are within the mean free path of secondary electrons, then they can be ejected from the material. The secondary electron coefficient ($\delta$) is the number of ejected secondary electrons per incident electron. Typical values range from 1.5 to 3 for a primary beam energy of about 1 keV, meaning that more secondaries escape the surface than enter it. These leave behind holes, which give the surface a net positive charge. If the secondaries do not have sufficient energy to escape or reenter the crystal, then they can become trapped a short distance above the surface. An electron cloud is thus produced above the surface, known as a space charge, and it acts as a barrier for subsequent incident electrons.[35]

Bennewitz and associates studied the surface potential by looking at desorption of $F^+$ ions from a $CaF_2$ sample under 1 keV electron bombardment. In their work, they point out that the positive surface potential is a result of secondary electron loss from the near surface region. Therefore, it does not depend strongly on the primary beam current, but only on the secondary electron distribution. The primary beam current will influence this potential when there are current pathways to the surface from other pathways, such as desorption of positive ions from the surface, or a leakage current between the irradiated spot and the sample holder.[64]

Seager et al. have postulated that instead of trapping electrons outside the surface, internal fields lead to charging during electron beam bombardment.[52] Utilizing secondary electron emission energies and carbon Auger peak shifts during irradiation with electron beams of energies from 0.5 to 5 keV, they were able to provide evidence of surface charging. Four phosphors were studied: ZnS:Ag, $SrGa_2S_4$:Eu, ZnO:Zn, and $Y_2O_3$:Eu. All were powders sedimented onto ~1 $cm^2$ Au foil. Particle diameters varied from 1 to 10 μm, and the layers were about 5 to 10 particles thick. When the researchers changed the potential of the plate that the samples were mounted on, surface potential on the front of the sample (closest to the beam) varied. Figure 2-12 shows results for $Y_2O_3$:Eu, which is representative of the other phosphors. The figure shows that the energy of the C Auger electrons changed linearly with application of the applied bias. This suggests that the backing plate bias led to a change in the surface potential that altered the escape energy of the Auger electrons. Similar shifts were seen for the secondary electrons. Thus, it is possible to change the potential of the phosphor with application of a backing plate bias.

Seager et al. also used dual electron beams to irradiate the sample during excitation. The second electron flood beam was used to control surface potential of the phosphor. Their results led them to believe that secondary electrons are not recaptured and used to build an electron cloud, as postulated by Ozawa, Yoo, Lee, and others; rather, an internal mechanism is responsible for bringing the phosphor into a steady state condition. They postulated that this internal mechanism is a buildup of positive charge near the surface, with a corresponding negative charge near the end of range of the incident electrons.

One problem with the experiments of Seager et al. is the fact that the potential of the front surface of the phosphor was unpinned. This made application of a known field within the phosphor difficult. To circumvent this problem, Seager applied a metallic mesh to the front surface of the phosphor to pin the surface potential at electrical ground. Electric fields were then applied across the phosphor layer to either enhance or retard the cathodoluminescence, depending on polarity.[65] Two phosphors -- $Y_2O_3$:Eu and $Y_2SiO_5$:Tb -- were sedimented onto brass plates. Total thickness of the phosphor layer was around 25 μm. Metal mesh with square holes (7.5 μm) was attached to the top surface of each sample. These grids allowed electric fields to be induced within the phosphor layer while still allowing incident electrons to reach the phosphor surface. Figure 2-13 shows this sample configuration. It was found that the maximum voltage that could be applied before breakdown was between 400 and 450 V. This voltage is important because it gives a measure of the dielectric strength of the material.

Initial results suggested that internal fields could be used to sweep generated charges away from or toward the surface. This would, in turn, lead to an increase or

decrease in cathodoluminescence because of losses to surface recombination.[65] However, further experimentation led to the conclusion that the results seen could be caused by surface potential fluctuations. Instead of changing the internal fields of the material, these fluctuations caused the energy of the incident electrons to be altered. The most likely explanation for the unpinned potential of the surface is that there was an air gap between the phosphor and grid as a result of the roughness of the powder.[66] Thus, intimate contact is needed if the internal fields of a material are to be altered in a controlled fashion. Coatings applied directly to the phosphors could provide such a situation.

Recently, Pantano et al. published an explanation of charging that takes into account the internal fields, with the addition of allowing for a negative surface potential. They rely on a model proposed by Cazaux[67] which depends on the stored charges per unit area, $q_+$ and $q_-$, and the charge densities, $\rho_+$ and $\rho_-$:

$$q_+ = J_0 \delta t \qquad \rho_+ = \frac{J_0 \delta t}{d_s}$$

$$q_- = J_0 (1 - \eta t) \qquad \rho_- = \frac{J_0 (1 - \eta t)}{d_p}$$

where $J_0$ is the incident primary-beam current, $\delta$ is the secondary-electron emission coefficient, $\eta$ is the backscatter coefficient, t is the time, $d_s$ is the thickness of the positively charged surface layer, and $d_p$ is the penetration depth of the incident electrons.[68] If $1 - \eta > \delta$, the total negative charge $q_-$ will exceed $q_+$ in time and the surface will charge up negatively. The negative surface charge will then act as a potential barrier for incoming electrons. This can only occur for $\delta < 1$, such as for beam energies below

about 1 kV. The reduced energy of the incoming electrons will limit the luminescence from the material. If $\delta > 1 - \eta$, the positive surface charge $q_+$ will exceed the negative end of range charge $q_-$. This process will be self-regulating because as the positive surface potential increases, the low energy secondary electrons will not have enough energy to escape. The result is a limited, but stable, positive surface.[68] Under such conditions, the excited electrons generated within the phosphor are swept toward the surface, where there is a high probability of nonradiative recombination.

One possible method from the presented models above for affecting the luminescence is to change the velocity of the incoming electrons. Yoo and Ozawa claim that charge buildup on the surface produces such a velocity change.[35, 63] Internal fields could also build up similar surface fields if $\delta < 1$, as shown in the models by Seager and by Pantano et al. As a consequence, incident electrons are repelled by an electrostatic potential at the surface, which lowers their velocity. Due to their lower incident energy, the electrons that make it into the material have less energy with which to excite luminescence. Based on calculations of the dielectric strength of the phosphors, as discussed below, however, this does not seem to be a reasonable model.

Dielectric strength is a measure of the maximum electric field that can be applied across a dielectric before breakdown. The equation is as follows:

$$\xi_{max} = \left(V/d\right)_{max}$$

where $\xi$ represents the electric field, V represents the voltage, and d represents the distance. Most materials have a dielectric strength of $10^5$ to $10^7$ V/cm.[69, 70] For $Y_2O_3$:Eu, it has been reported that breakdown occurred at 450 V over a 25 μm film.[65] This would correspond to a dielectric strength of $1.8*10^5$ V/cm, which is within the

expected range. The value calculated is lower than the bulk dielectric strength because the numbers were taken from a powder sample. Therefore, the number has a larger contribution from the lower surface dielectric strength than from the higher bulk dielectric strength. Given the above dielectric strength and that the penetration depth of the electrons within the phosphor surface is on the order of 1000 Å (probably an overestimate), breakdown would be expected at around 1.8 V. Even if one assumed a dielectric strength one order of magnitude larger, breakdown would be expected at 18 V. When this is compared to the energy of the incident electrons (500 – 4000 V), it does not seem possible that these small voltages could be affecting the velocity of the incident electrons enough to cause a large decrease in luminescence.

Considering the above argument, the most plausible explanation of charging is that internal fields are causing excited secondary electrons to be swept toward the surface, where they have a high probability of nonradiative recombination or emission. These internal fields are a result of a positive surface charge due to secondary electron emission and a negative charge region near the end of range of the primary electrons. In order to reduce charging in phosphors, the internal fields need to be minimized or removed so that generated secondary electrons remain in the bulk of the phosphor, where they have a higher probability of radiative recombination. This, in turn, will lead to a higher overall efficiency.

### Cathodoluminescent Degradation

One of the main problems that needs to be overcome in order to make an FED device for mass production is that of increasing FED lifetime. This is especially

important for a low voltage device. As the accelerating voltage of the electrons is reduced, the brightness of the device decreases rapidly, due to a loss in efficiency. To attempt to regain the original luminescence, higher currents are used.[43] In turn, these higher currents cause operational problems in the device. Besides saturation, as discussed earlier, degradation is greatly enhanced due to the high current densities employed. When the lifetime of the device is considered, the degradation of both the phosphor and field emitters needs to be taken into account. Both can lead to a reduction in the cathodoluminescence seen from the FED.

In a CRT, it is relatively easy to maintain a good vacuum over the lifetime of the device. This is due to two reasons. First, the relatively small surface-to-volume ratio of CRTs makes it easy to initially pump the device. Second, there is a large area over which to apply a getter material, giving a large ratio of active getter area to system volume. The FED does not have either of these benefits. Due to its closely spaced anode and cathode, it has a large surface-to-volume ratio. This makes it difficult to initially pump the device due to the conductance between the plates. There is also little area over which to apply the getter material.[71] Some improvements to the pumping could be realized by increasing the gap between the plates, but this creates problems with the focusing of the electrons and would require the insertion of a focusing grid into the device. Placing the getter between the anode and cathode could help with the pumping, but this too would cause problems with the actual operation of the display.[71] New techniques are being explored for gettering, such as placing a non-evaporable getter around the sides of the package or attaching a getter to the back with small holes to allow pumping. Although

these might help in the maintenance of the vacuum within the FED, the role of gases needs to be considered when examining the device operation.

There are two main sources of background gas in a FED device, those resulting from desorption from the device structure and those released from the phosphor due to electron beam impingement. Gases released from the phosphors depend on the specific material in question and will be discussed later in this section. All other gases are mainly a result of outgassing from the structural components of the device, such as the spacers, cathode, and black matrix. Other sources of background gas are present -- for example, permeation -- but these usually contribute a negligible amount to the overall composition of gases in the device. The main outgassing products inside a FED are $H_2$, $H_2O$, CO, $CO_2$, and hydrocarbons such as methane, ethane, and propane.[72, 73] Depending on the relative amount of these gases and the specific material, various processes can lead to decreased cathodoluminescence. If the environment is dominated by carbon-containing gas molecules, then carbon deposition on the phosphor surface will most likely result.[74-76] Under steady-state conditions, gas molecules are constantly physisorbing on and desorbing off the phosphor surface. When an electron beam is present, it can impart energy to these molecules and cause them to crack (i.e., break the bonds holding them together) to atomic species. The carbon is then free to form bonds with the surface, while the other components combine with each other and are released back to the gas phase. The rate at which this will occur depends on the residual vacuum pressures of the specific atoms and molecules. As the carbon layer grows, it will substantially reduce the luminescence from the phosphor particle in the electron beam exposed area.[74-76] After

exposure in such an environment, a dark spot is usually present that can be seen with the naked eye.

If hydrogen and water, rather than carbon compounds, dominate the FED environment, then degradation is still present, but it often will be a result of a change in the internal efficiency of the phosphor.[77] Although different materials degrade in different ways and at different rates, certain generalizations can be made for various types of phosphors. Some of the most efficient high voltage phosphors currently known contain sulfur. Examples include $Y_2O_2S$:Eu for red, ZnS:Ag:Cl for blue, and ZnS:Cu:Al:Au for green. Under the electron beam, dissociation of residual gas molecules can occur. These atoms can then form bonds with the atoms in the outer layer of the phosphor. Due to the volatile nature of the sulfur compounds such as $SO_x$, $H_2S$, etc., they desorb back into the vacuum. As a result, sulfur is leached from the surface.[13, 78-83] It would be expected that this phenomenon would be limited to the near surface region, however, the lack of sulfur causes a diffusion gradient that brings more sulfur to the surface region.[68] As the sulfur is removed, the particle surface is converted into its oxide equivalent. Swartz et al. showed that when ZnS is subjected to an electron beam, its surface is converted into the non-luminescent ZnO.[13, 78, 80, 82] Trottier demonstrated that $Y_2O_2S$:Eu is transformed into the less efficient $Y_2O_3$:Eu on the surface under an electron beam. In addition to the decrease in luminescence, a peak shift was observed for $Y_2O_2S$:Eu that was due to the emission from the $Y_2O_3$:Eu layer.[13, 14] These types of degradation reactions have been termed electron-stimulated surface chemical reactions (ESSCR) because of their mechanism.[13, 14]

It would seem, based on the mechanism discussed above, that oxide-based phosphors would not be susceptible to electron beam degradation. However, this is not the case. Oxides usually degrade because of electron-stimulated desorption on the surface. This causes the introduction of lattice defects in the material.[68, 84] Because they are a disruption in the lattice symmetry, defects tend to increase the nonradiative recombination rates. As the rate of nonradiative transitions increases, the efficiency of the phosphor decreases and, thus, so does the cathodoluminescent brightness. Although this is fundamentally a surface phenomenon, the electron interaction proceeds deep into the material. Once the outermost surface is changed, an activity gradient exists to drive the diffusion of species in subsurface regions. Thus, the damage continues into the phosphor. Compounds most affected by this are ones in which the cation and anion have Pauling electronegativity differences greater than 1.7, a category that includes many oxides.[68] In a way, this is similar to the sulfide case described above. Even though ESSCR causes the majority of the degradation in sulfide-based materials, defect introduction is occurring simultaneously to further decrease the luminescence.

In all of the scenarios discussed, the electron beam caused the degradation to take place. It seems natural, therefore, that the length of exposure determines the extent of degradation. By convention, this is measured as the coulomb load to which the phosphor has been exposed. It can be expressed as:

$$\text{Coulomb load (Coulombs/cm}^2\text{)} = (I * t) / A$$

where I is the sample current (Coulombs/sec), t is the time of exposure (sec), and A is the area of the beam spot ($cm^2$). For this reason, this type of degradation is often referred to as Coulombic aging.[85-87] There have been different formulas presented to represent the

loss in luminescence with Coulomb load, but the one most widely referenced was derived by Pfanhl at Bell Labs. It simply states that the intensity as a function of dose can be expressed as:

$$I(N) = \frac{I_0}{(1 + C'N)}$$

where I is the cathodoluminescent intensity at any given dose N (number of electrons/$cm^2$), $I_0$ is the initial cathodoluminescent intensity, and C′ is the burn parameter ($cm^2$).[14, 71] The burn parameter C′ will often be replaced by a quantity $1/Q_{50\%}$ in which $Q_{50\%}$ is equal to the charge dose, for which the initial intensity of the phosphor is halved.[88] Not all phosphors behave in such an ideal way. Sometimes a phosphor will show an initial rapid decrease in luminescence that is followed by a slight rise and eventual inflection and further decrease in intensity. To account for this rise, Cappels and associates have derived an equation that uses two decay curves similar to the equation above.[89] In essence, their equation is just the superposition of two simple inverse decay curves.

Holloway, et al. modeled the degradation they observed in sulfide-based phosphors based on an ESSCR sulfur removal rate. Their model predicted that the concentration of sulfur on the surface is exponentially dependent on the dose. It is a more in-depth study of the exact mechanisms behind the degradation process. Their equation is as follows:

$$\frac{I}{I_0} = e^{(-K'r_\pi N)}$$

where K′ is a constant, $P_{rg}$ is residual gas pressure, and N is the electron dose. However, they pointed out that within experimental error, the data could be made to fit their equation or Pfahnl's.[13]

At the beginning of this section, it was mentioned that the electron beam can not only degrade the phosphor, but can lead to degradation of the emitter tips as well. Usually, this is an indirect contamination due to volatile species being ejected from the phosphors. It is well established that sulfide-containing phosphors "poison" the emitter tips during excitation with an electron beam.[11, 90-93] This is suspected to be a result of the ejected volatile species traveling through the vacuum and reacting with the emitters. Upon reaction, these species can change the work function of the tip material. Due to the change in work function, the emission characteristics will be altered.[3, 94] Therefore, not only a sulfide, but any phosphor has the potential to degrade the cathode emitter tips. Consequently, the more volatile species have a much larger effect on field emission from the cathode than their more stable counterparts. For this reason, oxides have received considerable attention. However, due to efficiencies lower than sulfides or oxysulfides, they represent a trade-off in performance.

### Coatings for Phosphors

Key issues in designing phosphors for low voltage FED applications are improved efficiency and reduced degradation. Many researchers have attempted to use coatings to accomplish these goals.

In CRT manufacturing, an aluminum backing layer is applied to the phosphor screen. Usually, a lacquer film is first deposited to provide a planer surface on which to

deposit the aluminum film. Then the lacquer is baked out. The aluminum reflects generated light back toward the front of the device to improve brightness and contrast. Even though the aluminum is an effective energy barrier for the incoming electrons, it is not a problem due to the high voltages used in CRTs.[71, 95]

Many groups have looked at coating for protecting phosphor particles from electron degradation. Some of the earlier work in this area was performed by Kingsley and Prener. They used sol-gel processes to coat ZnS:Cu particles with non-luminescent ZnS layers. Thickness of the layers was determined based on weight gain and size distribution of the powder after processing. Figures 2-14 and 2-15 show results of their work. As can be seen from the figures, the coatings did not change the slope of the luminescence versus voltage curves; they only changed the turn-on voltage. The turn-on voltage is found by taking an extrapolation from the linear portion of the luminescence versus voltage curve. The voltage at which the linear extrapolation crosses the axis (i.e., when the intensity is zero) is the turn-on voltage. The fact that the coatings only changed the turn-on voltage suggests that the coating did not alter the luminescent states in the phosphor, but only caused a decrease in the incoming electron energy. (A layer that exhibits this type of behavior is often referred to as a "dead layer" because the energy lost in the layer is no longer available to excite luminescence.) Using this assumption, Kingsley and Prener were able to model the decrease in luminescence with a Makhov power loss equation with corrections for the spherical surface and surface recombination.[96] The Makhov power loss equation is given by:

$$P(x, j_0, V_0) = j_0 V_0 \exp\left(- X^2 - X^{0.9}\right)$$

where P is the beam power per unit area, $j_0$ is the beam current density at the surface, $V_0$ is the accelerating potential, and X is a normalized depth in the material given by:

$$X(x,V_0) = \frac{x}{\rho^{-1} * C * V_0^n}$$

where ρ is the density, C and n are materials constants, and x is the depth in the material.[96]

As noted above, sulfide-based coatings may be degraded under electron beam exposure due to ESSCR at the surface. For this reason, other materials have been studied as potential capping layers. Bechtel reports on the use of a phosphate coating to improve the degradation characteristics of ZnS-based phosphors.[97] Dmitrienko suggests the use of stable oxides such as $SiO_2$, MgO, or $Al_2O_3$, however, he notes that the optimal thickness and deposition techniques still need to be determined.[98]

One of the first studies to show the protection offered by applying coatings to phosphors was done by Trottier and Fitz-Gerald. They demonstrated that coatings of $TaSi_2$ and Ag deposited by pulsed laser ablation onto $Y_2O_2S$:Eu, a highly efficient red phosphor, could be effective at reducing the degradation of this phosphor. Figure 2-16 shows the results from their work. The pulsed laser deposited coatings of $TaSi_2$ and Ag were compared against wet-chemistry coatings of $SiO_2$ and phosphate. The pulsed laser coating was better at slowing degradation and exhibited far less loss in brightness after aging to 20 C/cm$^2$. Of the two laser ablated coatings, $TaSi_2$ protected the underlying phosphor better than Ag. This is believed to be due to Ag migration or volatilization under the electron beam.[14, 99]

Recent interest in phosphor coatings has concentrated not only on their protective properties, but also on their use to increase cathodoluminescent efficiency at low

voltages. The group of Yang and Yokoyama showed that coating $Cu_xS$ on ZnS:Ag:Cl led to an increase in the efficiency of the phosphor.[100] However, sulfides are susceptible to ESSCR in a FED environment. It seems that wide-band oxides are the preferred choice for increasing the efficiency of the phosphors.[101] The group of Kominami et al. showed that coating ZnS:Ag:Cl with $In_2O_3$ led to improved efficiency at voltages below 500 eV. They attributed this to an increase in the conductivity of the phosphor, which allowed charge to be dissipated. An increase in the phosphor lifetime was also reported.[102] Villalobos and associates coated $SiO_2$ on ZnS:Ag particles using a newly designed spray coating process, in which the host particle is suspended in a liquid mixture and then sprayed into a hot zone where the coating gels on the surface. The particles are then heat treated as a final step. Using this technique, increases in both the brightness and degradation resistance were reported.[103]

Attempts to model these phenomena have been made by groups at the Georgia Institute of Technology.[15, 93, 104] They used a 1-D discrete computer model to calculate the efficiency of the phosphor with varying thicknesses of coating applied. A correction term was added to account for surface recombination velocity and the band offset of the coating compared to the host material. Experimental results were collected for $SiO_2$ coatings on ZnS:Cu:Al deposited by sol-gel methods. If the pH was kept around 6.5 and the silica concentration at 1 wt%, then enhancement of the cathodoluminescent efficiency was possible below around 2 keV. However, the enhancement was only seen for coatings less than 40 nm thick. Beyond this value, electron stopping in the coating was reported to overshadow the surface recombination gains.[15, 93, 104]

It should be noted that processing of the phosphors will have an impact on their cathodoluminescent response. Many commercially available phosphors have undergone a series of growth, grinding, and annealing steps. Many researchers have shown that improved cathodoluminescence is possible by tailoring these processes to produce a more uniform and less defective particle surface.[105, 106] The reader should be aware of this when examining some reports on the effects of coatings. Some authors will apply coatings to phosphors that have been grown in their own laboratory. The coated phosphors will then be compared against commercially available materials of the same composition. This is an unfair comparison because the commercial powders may have a lower CL response than the laboratory-grown phosphors. Thus, it is difficult to separate the effects of the coating from those of the phosphor processing.

Another issue to consider when coating phosphors is the consequences of the coating on the ability to apply the phosphor to the anode faceplate. Certain materials will cause aggregation of the phosphor particles in the slurry before screening, while others will help them stay dispersed. In order to create screens with the highest possible brightness, dispersion of the particles needs to be maintained, and thus the coatings must help maintain this condition.[107]

### Pulsed Laser Deposition (PLD)

Advances in PLD have made it an increasingly popular method for applying coatings to materials.[108, 109] In this technique, short laser pulses are used to evaporate material from a target. Several different things happen during the laser pulse. Lowndes describes these as "rapid heating and vaporization of the target; increasing absorption by

the vapor until breakdown occurs to form a dense plasma; and absorption of the remainder of the laser pulse to heat and accelerate the plasma."[110] The particles in this plasma undergo collisions, which in turn produce a highly directional expansion away from the target. All of this is occurring in the Knudsen layer above the target.[110] These evaporated materials undergo gas phase collisions and are subsequently deposited onto a substrate. By controlling the ambient gas mixture, background pressure, substrate temperature, and laser energy and duration, films can be grown to desired specifications. Due to the method of ablation, the flux of material leaving the target is strongly peaked in the direction perpendicular to the target surface.[110, 111] However, recent advances in the use of target rotation and apertures have made uniform deposition over larger areas possible.[112]

Of particular interest are the advances being made in the application of PLD to optical materials. An example includes the deposition of ultrathin (<10 nm) indium tin oxide (ITO) films. ITO is one of the most widely used transparent conductive coatings in electro-optic applications.[113] PLD is particularly good for growing oxides due to the fact that the material transfer from target to substrate is normally stoichiometric, meaning that the deposited film has the same composition as the target.[110, 114] This is a result of the high initial rate of heating and highly nonthermal target erosion.[110] Large bandgap semiconductors and dielectric materials usually have large optical absorption at short wavelengths. Therefore, large amounts of the laser energy are deposited in a small volume close to the surface. As a result, the sublimation temperature of the material is attained at depths greater than the thermal diffusion distance of the constituents. Target

components are not able to segregate, therefore they leave the target in proportion to their bulk concentrations. This results in deposits with the same composition as the target.[39]

By varying the conditions under which thin film phosphors are deposited, their optical properties can be improved. $Y_2O_3$:Eu is a good example of these effects. It has been shown that by increasing the oxygen partial pressure during deposition, rougher films are produced. This leads to an increase in brightness due to forward scattering by anomalous diffraction.[39, 115] Microcrystallites of II-IV compounds such as CdTe and CdS have been grown in a similar fashion.[116] Temperature of the substrate can also affect film properties. Models suggest that higher substrate temperature will lead to rougher films.[117] The type of substrate will also determine whether amorphous, polycrystalline, or epitaxial single-crystal films are grown.[110] In one experiment, $Y_2O_3$:Eu was grown on bare (100) Si wafers and on diamond-coated Si wafers. The diamond coating was prepared using a hot filament chemical vapor deposition. The phosphor films were grown under identical conditions on the two substrates. There was a substantial improvement in luminescent brightness from the diamond-coated substrate. This was attributed to the higher roughness of the surface; see Figures 2-17 and 2-18.[41, 118]

Sapphire substrates have also been used to improve the brightness of $Y_2O_3$:Eu thin films. The increase in brightness is believed to be due to the low absorption and low refractive index of red light in sapphire and to the improved growth of grains with unidirectional orientation on the (0001) sapphire substrates.[119]

Finally, $Y_2O_3$:Eu films have been epitaxed onto $LaAlO_3$ substrates. These are good substrates because the lattice mismatch is only 0.8% with an orientation of

[110]$Y_2O_3$||[100]$LaAlO_3$ and [-110]$Y_2O_3$||[010]$LaAlO_3$. Z-contrast scanning transmission electron microscopy (STEM) was used to demonstrate the absence of precipitates of Eu in the deposited films.[120] This is advantageous in a luminescent film because the activators are thus spread out.

Besides its use to deposit phosphor thin films, PLD has also been used to coat phosphor powders to improve luminescence and reduce degradation. Fitz-Gerald deposited $Y_2O_3$:Eu onto powders of $SiO_2$ and $Al_2O_3$. The powders were agitated in a fluidized bed setup so that the deposited coating would be uniformly distributed over the powder surface.[121-123] The photoluminescent spectra showed the 612 nm peak from the $^5D_0$-$^7F_2$ transition in $Y_2O_3$:Eu; so the coatings were effectively deposited onto the core particles.[122] Transmission electron microscopy (TEM) was used to confirm that the coatings were continuous.[123] Next, coatings of TaSi and Ag were deposited on $Y_2O_2S$:Eu, a highly efficient red phosphor, to help reduce degradation under electron beam excitation. As discussed in the previous section, degradation curves clearly showed the advantage of these two coatings for protecting the phosphor.[14, 99]

**Motivation for this Work**

Coatings have been shown to be effective in slowing the degradation of phosphors, especially at the low voltages and high currents of a FED environment. Improvements in the efficiency of cathodoluminescence at low voltages have also been demonstrated. Thus far, most of the work on coatings has focused on putting a coating around the entire phosphor particle, using such techniques as sol-gel processing or spray pyrolysis. These steps add considerably to the cost of making the powder and must be

monitored closely to ensure proper results. In this work, the commercially available phosphors $Y_2O_3$:Eu and $Y_2SiO_5$:Tb were sedimented onto Mo substrates and coated using pulsed laser deposition. This is a much simpler process that can be applied to large area screens using existing coating techniques.

To ensure that all results observed were due to the coating and not the processing of the screen (such as deposition, CL geometry, etc.), half of the screen was masked during deposition. This allowed side-by-side comparison of coated and uncoated phosphor material. Coatings of MgO and $Al_2O_3$ were deposited at various thicknesses to examine their effects on cathodoluminescence. These materials were chosen because they both have large work functions compared to the host materials. This should lead to enhanced efficiency due to repulsion of electrons from the particle-coating interface and thus a lower surface recombination velocity.

Phosphor powders were chosen for this study instead of thin films because they represent real world devices. Thin films provide an excellent surface on which to study the basics of electron interactions, but they can introduce other problems. Lattice mismatch between the luminescent film and substrate can lead to a drastic reduction in cathodoluminescence. This can be alleviated in some instances by the careful choice of substrate. (For example, $LaAlO_3$ for growth of $Y_2O_3$:Eu.[124]) However, this is often a difficult challenge. There is also the problem of a much lower intensity due to greater internal reflection in the thin film.[39] Because the initial intensity from the thin films is low, detecting changes in the brightness becomes more difficult. Because phosphor powders are used in FED devices and offer high initial brightness, they were chosen for this study.

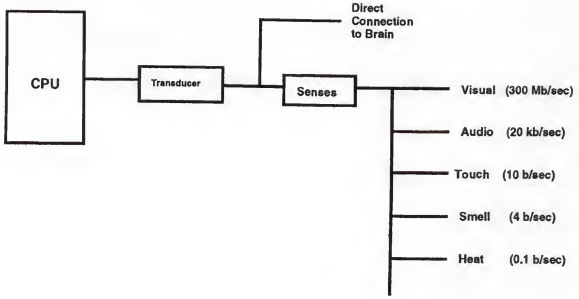


Figure 2-1 The different means of interfacing between a human and a computer. Also shown are the speeds of each type of transfer.[6]

Table 1

The different types of flat panel displays and the advantages of each.

| Technology | Type | Size | Power | Advantages | Barriers |
|---|---|---|---|---|---|
| **AMEL** | emissive | small | moderate | Rugged, high-resolution, high-brightness | Pixel size limit, lack of suitable phosphor for full-color. |
| **OEL** | emissive | small | low | High luminous efficiency, low drive voltage | Lithography incompatibilities, instability, short lifetime, limited temperature range |
| **Plasma** | emissive | large | high | Mature technology, high brightness | High-power, slow refresh rates, limited military market |
| **Laser Projection** | light valve | large, scaleable | moderate | High brightness, display size is scaleable | Still in early stages of development, no full-scale prototype |
| **MEMS Projection** | light valve | large, scaleable | moderate | Some commercially available (TI-DMD), scaleable | Development of new technologies costly, digital artifacts may be a problem |
| **Reflective LCD** | light valve | small to medium | very low | Very low power, bistable | Limited temperature range, manufacturability, durability |
| **FED** | emissive | small to medium | low | Low power, high brightness, wide viewing angle | Manufacturability, lifetime |

Reproduced from reference 8.
The acronyms in the table stand for the following:
AMEL – Active Matrix Electroluminescent
OEL – Organic Electroluminescent
LCD – Liquid Crystal Display
FED – Field Emission Display

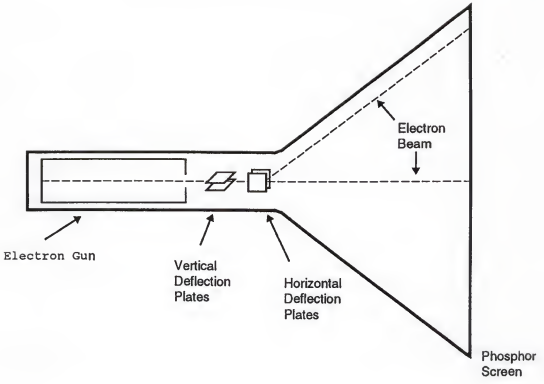


Figure 2-2 Typical cathode ray tube (CRT), consisting of an electron gun and deflection plates to raster the electron beam across the phosphor screen.[6]

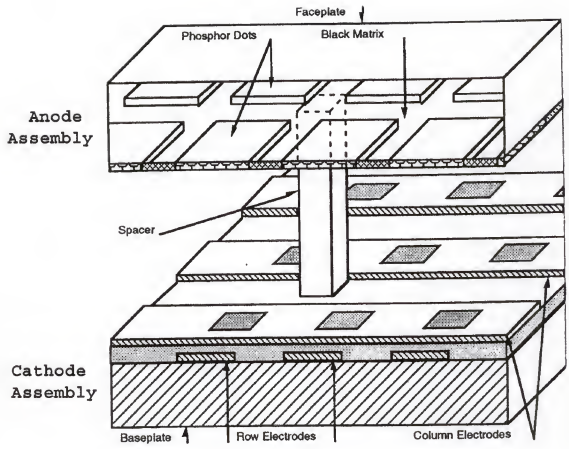


Figure 2-3 A typical FED setup, consisting of the cathode assembly, which houses the field emitter tips, and the anode assembly, a glass plate on which the phosphors are deposited. Spacers are used to separate the two halves of the device.[6]

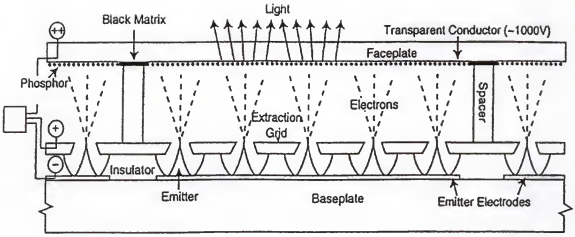


Figure 2-4 Schematic cross section of a typical FED. Not drawn to scale.[9]

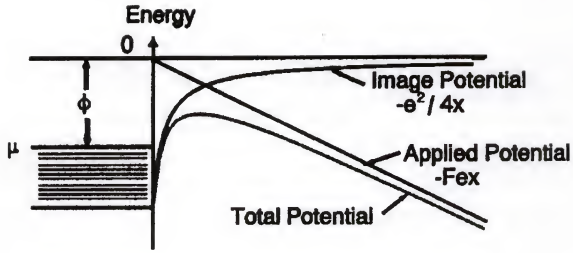


Figure 2-5 Potential energy curves of an electron near a metal surface. The "Image Potential" is with no external field. An externally applied field that is electrically negative to the surroundings can be represented by the "Applied Potential" curve. The resultant "Total Potential" will then be the superposition of the two curves. Due to the lower energy barrier at the surface, electrons in the metal have a finite probability of quantum mechanically tunneling into the vacuum.[22]

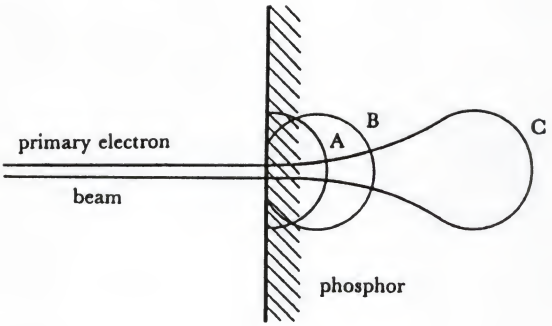


Figure 2-6 Electron penetration in a phosphor at various beam energies. Incident beam energy is increasing from A to B to C. This also demonstrates how the interaction volume moves closer to the surface as the beam energy is decreased. When surface recombination is considered, the interaction volume in A will clearly have a stronger influence from the surface than that in C. As a result, surface effects become more pronounced at lower beam voltages.[35]

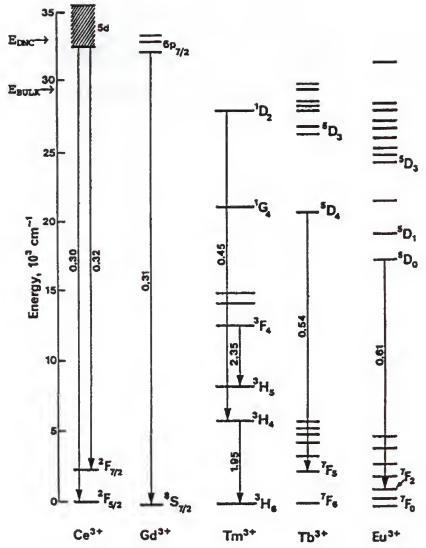


Figure 2-7 Expected transitions in various rare-earth dopants used for FED phosphors.[47]

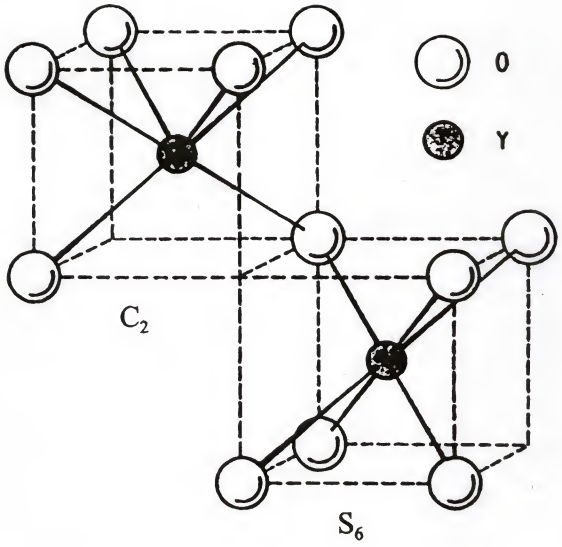


Figure 2-8 The two different crystallographic configurations of Eu in a $Y_2O_3$ host lattice. The $S_6$ symmetry is often referred to as $C_{3i}$ symmetry.[41]

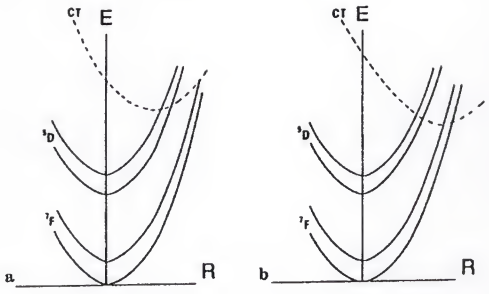


Figure 2-9 The dashed curves represent the charge-transfer (CT) state. In (a), the CT state helps feed the emissive $^5D$ levels because of its position relative to the $^7F$ ground state. This is the situation found in $Y_2O_3$:Eu and $Y_2SiO_5$:Tb. In (b), the offset of the CT state causes the electrons to be returned to the ground state, thus reducing the luminescence of the material.[25]

Table 2

Composition, color and efficiency at low-voltage operation of selected FED phosphors

| Composition | Color | Efficiency (lm $W^{-1}$) |
|---|---|---|
| 500 V | | |
| ZnO:Zn | Green | 10.7 |
| $Gd_2O_2S$:Tb | Green | 7.9 |
| $Y_3Al_5O_{12}$:Tb | Green | 2.0 |
| $Y_2O_2S$:Eu | Red | 3.5 |
| $Y_2O_3$:Eu | Red | 2.2 |
| $YVO_4$:Eu | Red | 0.4 |
| 300 V, 131 μA | | |
| CaS:Ce | Green | 3.10 |
| $SrGa_2S_4$:Eu | Green | 3.00 |
| $La_2O_2S$:Tb | Green | 5.20 |
| $Gd_2O_2S$:Tb | Green | 3.52 |
| $Y_2O_2S$:Eu | Red | 2.20 |
| $Y_2O_3$:Eu | Red | 1.57 |
| $Y_2SiO_5$:Ce | Blue | 0.25 |
| $Y_2SiO_5$:Tb | Green | 1.05 |
| LaOBr:Tb | Green | 1.95 |
| LaOCl:Tb | Green | 0.36 |
| LaOBr:Tb | Blue | 0.54 |
| LaOBr:Tm | Blue | 0.17 |

Reproduced from reference 2.

Table 3

Classification of FED structures

| Type | Anode voltage (kV) | Anode-cathode separation (mm) | Advantages | Disadvantages |
|---|---|---|---|---|
| High -voltage | 4-10 | 2-3 | • CRT phosphors & processes applicable<br>•High efficiency | •Focussing electrodes required<br>•Spacers with a high aspect ratio<br>•Breakdown |
| Medium -voltage | 1-4 | 0.2-0.8 | •Simple structure<br>•Fair efficiency | • Spacers with a relatively high aspect ratio |
| Low -voltage | 0.4-1 | 0.1-0.2 | •Simple structure<br>•High reliability<br>•Low cost | •Limited efficiency |

Reproduced from reference 11.

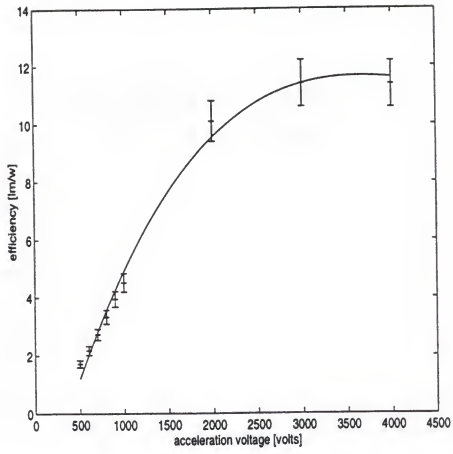


Figure 2-10 Efficiency versus acceleration voltage for $Y_2O_3$:Eu.[38]

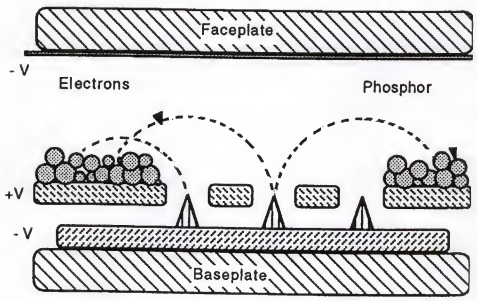


Figure 2-11 FED with phosphor on the gate electrode to double the light output from the device.[6]

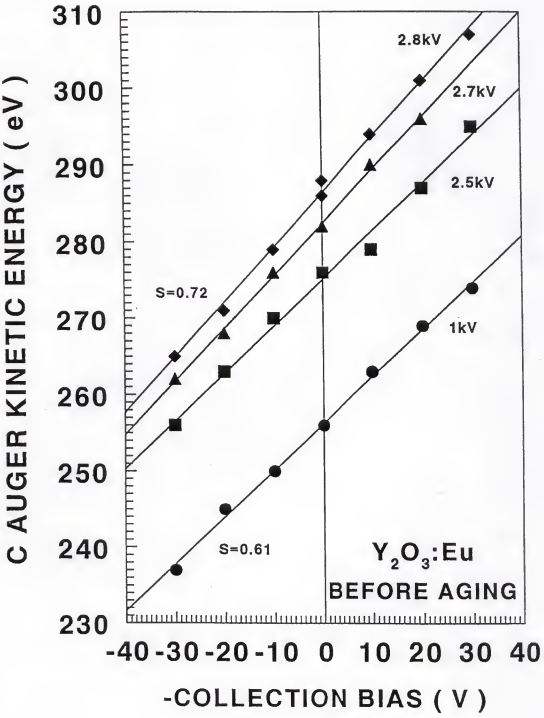


Figure 2-12 Carbon Auger peak shifts after changes in the bias of the sample mounting plate.[52]

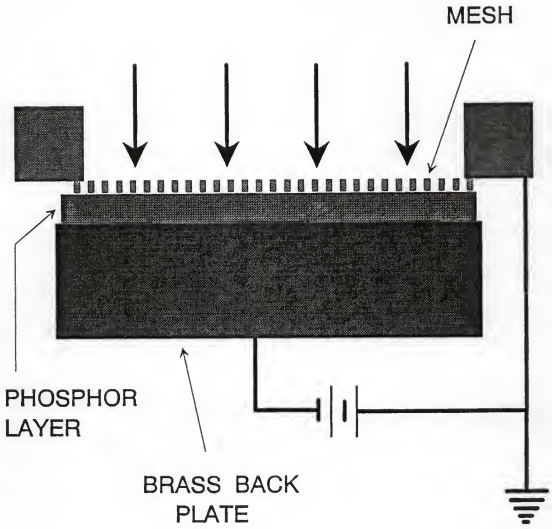


Figure 2-13 Setup for metal mesh placed on the phosphor surface for taking internal field measurements under electron excitation.[65]

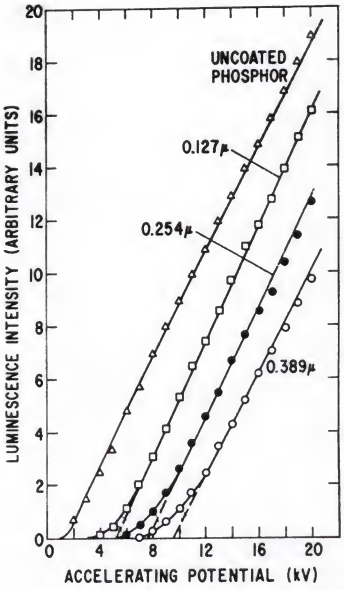


Figure 2-14 Luminescence versus accelerating potential for ZnS-coated (0.127 μm, 0.254 μm, or 0.389 μm thick) ZnS:Cu. The similar slope of the lines suggests that the coating did not alter the luminescent states of the phosphor, but only decreased the incoming electron energy.[96]

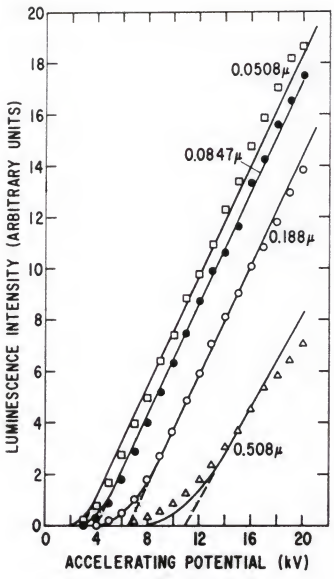


Figure 2-15 Luminescence versus accelerating potential for ZnS-coated (0.0508 μm, 0.0847 μm, or 0.188 μm thick) ZnS:Cu. The similar slope of the lines suggests that the coating did not alter the luminescent states of the phosphor, but only decreased the incoming electron energy.[96]

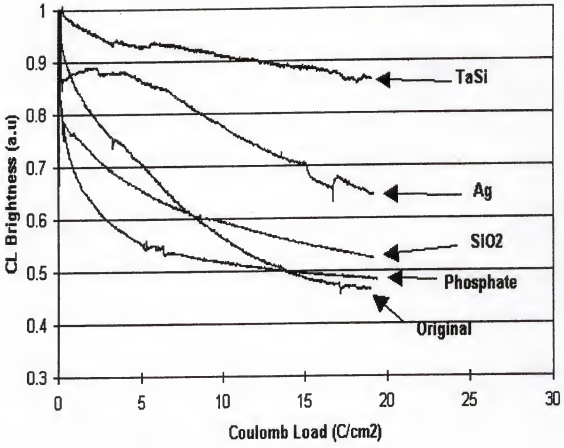


Figure 2-16 Cathodoluminescence degradation of $Y_2O_2S$:Eu with various coatings. The $SiO_2$ and phosphate coatings were applied by wet chemistry techniques, while the Ag and TaSi coatings were deposited by pulsed laser ablation in a fluidized bed setup. "Original" refers to the uncoated powder.[14]

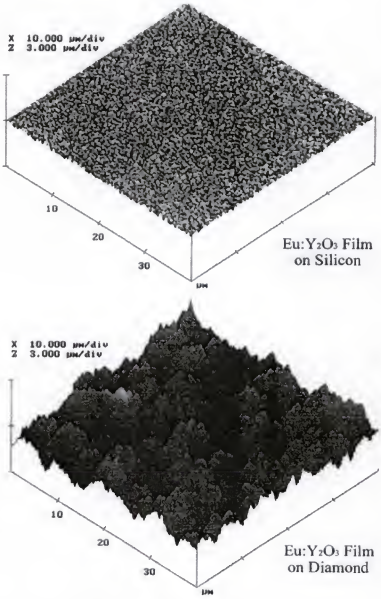


Figure 2-17 Atomic force microscopy (AFM) images of $Y_2O_3$:Eu film grown on bare Si substrates and on diamond-coated Si substrates. The images clearly show the higher roughness of the films on the diamond-coated material.[41]

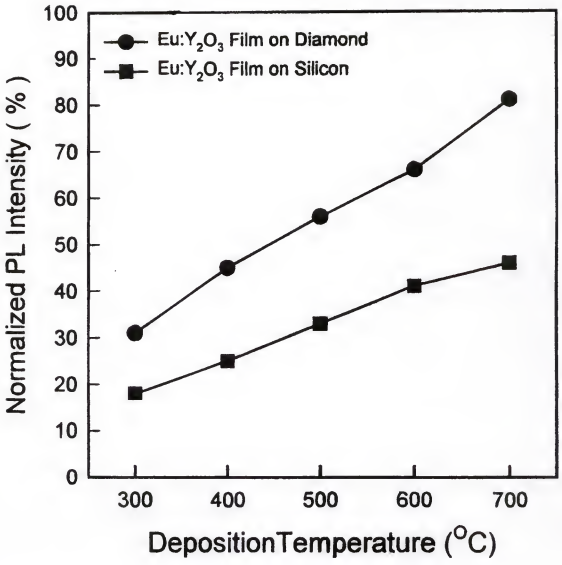


Figure 2-18 Photoluminescence from $Y_2O_3$:Eu films grown on bare Si and diamond-coated Si substrates. The curves show the higher luminescence attained with the diamond-coated substrate. This is attributed to the higher roughness of these films.[41]

# CHAPTER 3
# EXPERIMENTAL PROCEDURES

## Introduction

The effects of coatings on field emission display (FED) phosphors were studied in this work. Coatings of $Al_2O_3$ and MgO were deposited by pulsed laser deposition (PLD) onto screens of $Y_2O_3$:Eu and $Y_2SiO_5$:Tb. These screens were prepared by sedimentation from a phosphor slurry. During deposition of the coatings, a Si shadow mask was used to provide coating on only half of the sample. This allowed for direct comparison of coated and uncoated phosphor material.

Many different types of characterization techniques were used to measure the samples. Cathodoluminescence measurements were taken under steady-state and pulsed conditions to examine the response of the phosphors to an electron beam. Ellipsometry, transmission electron microscopy (TEM), and Auger electron spectroscopy (AES) were used to determine the thickness of the coatings. Finally, AES and a scanning electron microscope (SEM) with a fiber optic attachment used for measuring CL maps were used to examine coating uniformity.

## Sedimentation of Phosphor Screens

The phosphor screens of $Y_2O_3$:Eu and $Y_2SiO_5$:Tb were prepared by sedimentation of the powder from a slurry. The apparatus consists of plastic beakers with a hole drilled

in the bottom. Attached through this hole is a connector that allows for a tube to be inserted onto the bottom of the beaker. A vise-style clamp on this tube controls the flow of the liquid out of the container. Samples are held down on the bottom of the vessel by spring clips that are attached along the bottom edge.

The first step in the sedimentation process is preparing the slurry mixture. The phosphor is weighed and added to a magnesium nitrate hexahydrate and isopropyl alcohol mixture. This is then placed in a sonicator for 30 minutes to ensure complete dissociation of the phosphor throughout the slurry. Natural heating also takes place during the agitation, which helps hold the powder in suspension. At this time, the substrates are cleaned by rubbing them with a methanol-soaked swab and then immersing them in methanol and placing them in the sonicator for about five minutes. After cleaning, the substrates are attached to the bottom of the beaker. The hose is then attached and clamped off. With all of this in place, the slurry is poured into the beakers. It takes many hours for the phosphor to settle out of solution and coat the samples. Usually, the beakers are covered and left overnight. In the morning, the liquid is slowly drained from the beaker by loosening the clamp on the hose. The samples are then air dried in the container for several hours.

Both of the phosphors used for this work, $Y_2O_3$:Eu and $Y_2SiO_5$:Tb, were standard Nichia powders. These were chosen because they were readily available and would be typical for use in a FED. Molybdenum was chosen as a substrate material for all of the samples because of its good electrical conduction and high melting temperature. (Originally, gold was used as a substrate material because it is inert to most materials and

has a very high electrical conductivity. Unfortunately, the gold would not endure the 750° C temperature needed during the pulsed laser deposition of the coating materials.)

**Pulsed Laser Deposition (PLD) of Coatings**

Since PLD has been shown to be particularly good for growing oxides due to the fact that the material transfer from target to substrate is generally stoichiometric[110, 114], it was chosen as the means of depositing the $Al_2O_3$ and MgO coatings for this work. The apparatus used consists of a stainless steel chamber pumped by a Pfeiffer Balzers TPU 450 H corrosive turbomolecular pump with a TCP305 controller and backed by a MD41 diaphragm pump. A Leybold Trivac mechanical pump model # D4A was used for roughing the chamber. To control background pressure, a gate valve was used between the pump and chamber to adjust the pumping speed. Precision leak valves provide further control of pressure through backfilling of the chamber with a variety of gasses. Ablation energy comes from a KrF ($\lambda$=248 nm) 1 Watt Lambda Physik Lasertechnik LPX300 excimer laser. Pulse width was set at 10 nanoseconds and laser energy kept at about 350 mJ for all depositions. Pulse frequency was variable between 1 and 100 Hz, but 10 Hz was chosen for all experiments. Laser light enters through a viewport on the side of the chamber. Control of the laser dimensions and position is accomplished with collimating and focusing lenses located on an optics bench positioned between the laser and vacuum chamber.

Directly across from the laser entry viewport inside the chamber is the target holder. The holder is positioned so that the laser strikes at 45° from the surface normal, which in turn generates a plume perpendicular to the target surface.[110, 111] The target

holder is connected to a rotary motion feedthrough to allow target rotation during deposition, thus allowing better utilization of the targets. Target rotation also helps minimize deposition of large particulates from the target onto the growing film.[125] Substrates are mounted on a sample holder located directly across from the target. Target-to-substrate distance was set such that the samples were located near the end of the plasma plume, which was around 3 centimeters in the chamber used for this work. Plasma expansion models suggest that this is the optimal position for the substrate.[114] The sample was not rotated during deposition. Heating of the samples was accomplished using a quartz lamp located within the sample holder. This allowed for a range of 150°C to 1000°C, although 750°C was used throughout these experiments. A stainless steel heater plate was used to transfer heat to the substrates, which were mounted to this plate. A thermocouple attached to the plate provided accurate control of the deposition temperature throughout the run.

The $Al_2O_3$ and MgO targets were made from their powders. First, approximately five grams of the powder was placed in a hardened stainless steel die. The die used was designed to produce targets an inch and a half in diameter. A hydraulic press was used to compress the powder in the die to around 120 psi for 4 minutes. The green powder compacts of these two materials were found to hold together very well. Both materials came out of the die without excessive force, so no lubrication of the die was necessary. Had such lubrication been used, it could have been a source of contamination for the target. For similar reasons, no flux was used to help hold the compacts together, although a flux is occasionally added to increase the sintering of the powder in the compact. During firing of the compacts, the flux is supposed to evaporate, but if it does not, it can

also be a source of contamination. The compacts were then placed in a tube furnace at 1200°C for 12 hours. This anneal is used to greatly increase the density of the target. Finished targets were then silver pasted onto holders used to attach them to the rotary arm of the target holder.

Phosphor screens were attached to the stainless steel heating plate of the sample holder by silver paint. A piece of Si was placed over half of the screen to act as a shadow mask. A spring clip attached to the side of the sample holder was used to hold the mask in place. The target and substrate were then inserted into the vacuum chamber. Once sealed off, the chamber was evacuated to a base pressure of around $1*10^{-5}$ Torr. Temperature of the substrate was then raised to 750°C. At this point, the gate valve was partially closed and the precision leak valve opened to adjust the background pressure of oxygen in the system. Oxygen was fed to the leak valve from ultra-high purity compressed gas cylinders. A MKS model 247C mass flow controller set at 80 sccm was used between the gas cylinder and leak valve. Background pressure of 50 mTorr was used for the majority of the experiments, with 200 mTorr used for the remainder (as noted later in the experimental results section).

Contrary to most other deposition techniques, such as electron beam, thermal evaporation, and sputtering, PLD does not show a strong decrease in deposition rate with increasing pressure above a few mTorr. This is due to the inherent quasi-free jet expansion of the plume during pulsing. The particles in the plume impart momentum to the background gas molecules. Therefore, the background gas and plume travel together toward the substrate. This greatly reduces the scattering of deposition species due to

collisions with gas molecules. The result is a very long mean-free path for the particles, which allows deposition at higher pressures.[111]

Control of the coating thickness was achieved by closely monitoring the deposition time. Materials ablate at different rates, so the coating time had to be adjusted for each of the material systems used. For the system used for this work, it was found that the deposition rate at 50 mTorr was around 65 Å/min for $Al_2O_3$ and 18.2 Å/min for MgO.

## Characterization Techniques

Many different characterization techniques were used to determine the coatings' thickness and effect on the luminescence of the phosphor. The techniques include steady-state and pulsed cathodoluminescence (CL), ellipsometry, transmission electron microscopy (TEM), Auger electron spectroscopy (AES), and scanning CL in a scanning electron microscope (SEM).

Figure 3-1 shows the energy distribution of electrons emitted from a sample surface under electron bombardment. Electrons in various energy regions on this curve are measured in some of the aforementioned characterization techniques. The secondary electrons are used for secondary electron (SE) imaging in the SEM. The Auger electrons are measured in AES. The elastically backscattered electrons are used for diffraction analysis in the TEM.

**Steady-State Cathodoluminescence**

Cathodoluminescence (CL) is the process of generating light by electron beam excitation of a phosphor material. Incident electrons impart some of their energy to the phosphor material through electron excitation. These excited electrons can then recombine with an available hole (the absence of an electron) to produce visible light.[25, 35]

Cathodoluminescence measurements were carried out in a stainless steel vacuum chamber pumped with a CTI-Cryogenics cryopump and a Varian ion pump. Roughing was accomplished using a rotary-vane mechanical pump. Base pressure for this combination of pumps was between $5*10^{-9}$ and $1*10^{-8}$ Torr with no bake-out. Although baking the chamber would have allowed for a lower pressure by removing some of the desorbed gas on the walls, it was not an option due to a fiber optic feedthrough. However, these pressures are more than adequate for taking CL measurements. Electron excitation was from a Kimball Physics EFG-7F electron gun with a EGPS-7H power supply and RGDU-3C raster generation unit. The electron gun was capable of energies up to 5 keV and currents from 0.01 to 500 μA. Focus was set to maintain a spot size of approximately 2 mm.

Phosphor luminescence was collected using a fiber optic connected to an Ocean Optics S2000 spectrometer. This spectrometer uses a diffraction grating and a charge couple device (CCD) array detector, which allows luminescent spectra to be collected over the entire visible wavelength range. To further improve wavelength resolution, a homemade slit was fashioned on the end of the fiber before it entered the spectrometer. This greatly reduced the broadening of the luminescent peaks. This is especially helpful

in materials with closely spaced peaks that can become indistinguishable due to peak overlap.

To improve signal-to-noise in the collected spectra, the raster unit was utilized to redirect the electron beam off-axis. Due to the electron gun design, the filament used to generate electrons within the gun is visible through the exit aperture. This causes a bright white spot of light on the sample directly in front of the gun. Using a mechanical manipulation system, this filament light can be redirected away from the area of interest on the sample. This greatly reduces the background signal detected by the spectrometer. By setting the appropriate bias on the raster unit, voltage was applied to deflection plates on the electron gun to redirect the electron beam to the center of interest on the sample.

Accurate current measurement requires the collection of secondary as well as primary electrons. For this reason, a +100 V bias from a Fluke 343A DC Voltage Calibrator power supply was applied to the electrically isolated sample carousel. A Keithley 619 Electrometer/Multimeter was connected in series between the power supply and the carousel to measure the current. Background subtraction was used to account for any stray currents present in the system. A switch was installed between the meter and carousel to allow the carousel to be shorted to ground. This is necessary during measurement of the luminescence because the sample bias will impart extra energy to the incoming electrons.

The sample carousel held samples perpendicular to the incident electron beam. Samples were inserted such that the uncoated half of the powder screen was above the coated half, instead of beside it. In this arrangement, the electron beam could be moved from an uncoated to a coated area by adjusting the vertical position of the carousel.

Using only vertical repositioning assured that the electron beam-to-sample and sample-to-fiber alignment would not be changed. It is critical to keep these alignments constant because changing them will result in a change in the measured luminescence.

**Pulsed Cathodoluminescence**

Pulsed cathodoluminescence measurements are used to study the decay of the luminescence from a phosphor under a pulsed electron beam. The same chamber was utilized as in the steady-state CL measurements above. The Kimball Physics electron gun has a fast pulsing option. A grid located inside the gun is used to blank the beam. By applying a large negative bias to the grid, a potential barrier for the electrons is established. The magnitude of this potential barrier, adjusted through the grid voltage, determines how many electrons can make it past the grid. If an electron has enough energy to surmount this barrier, then it will proceed through the gun as normal. Pulsing is accomplished by sending a positive voltage pulse along the grid supply line to reduce the grid retarding voltage. By selecting the appropriate grid bias, the positive pulse can be used to turn the electron beam on and off. Thus, the characteristics of the positive pulse determine the electron beam characteristics. Kimball Physics supplies a box that can be installed in the grid voltage line for such an operation. This box allows the pulse generator to be connected to the grid line and prevents the grid voltage from being sent back through the line to the pulse generator. Due to the design of the electron gun, the grid voltage (typically 100 to 250 V) is added to the accelerating voltage (typically 0.5 to 4 keV) before being transmitted down the grid line. During operation, it was noticed that

the pulsing box would not give consistent pulsing. To correct this, the circuit was redesigned and a new box built to provide a stable, low noise operation.

A Hewlett Packard (HP) 8112A Pulse Generator was used to provide the positive voltage pulses to turn the electron gun on. Pulse width was set to 10 μs with a delay of 65 ns and a period of 100 ms. Amplitude was adjusted to produce a 16 volt turn-on pulse.

Luminescence was collected using a fiber optic mounted inside the vacuum system. The other end of the fiber was connected to a Hamamatsu Photomultiplier Tube (PMT). A 1150 V power supply was used to power the PMT. A box was used to house the PMT with a fitting for the fiber on the outside. During operation, a thick black piece of fabric was wrapped around the box to reduce the amount of stray light. A holder was designed for the inside of the box to allow filters to be placed between the fiber and PMT. Filters were used to select specific wavelength regions. This gave the ability to study the decay of single peaks (different decay states) of the phosphors. Filters used included a 535 nm bandpass and Corning glass 2-73, 3-70, and 5-58 highpass filters. Figures 3-2 to 3-4 show the transmission of these Corning filters. The output of the PMT was connected through a "T" junction to an oscilloscope and a HP 3478A Multimeter. The multimeter was used to look at the voltage from the PMT due to background light in the chamber, most of which was due to filament light from the electron gun. During actual measurement, the multimeter was disconnected to reduce the amount of noise in the signal. The oscilloscope used was a 500 MHz 2 GS/s Hewlett Packard Infinium Oscilloscope Model 54825A. A built-in disk drive was used to save files and transfer them to another computer.

Sweep rate on the oscilloscope was chosen to ensure that the entire decay pulse was measured. This meant making sure that the after-pulse luminescence returned to background level. Once the sweep rate was set, the sample averaging was adjusted to give 25044 data points per scan. To further improve signal-to-noise, 3000 scans were collected for every set of conditions. The oscilloscope automatically averaged these as they were collected. Therefore, every data file consisted of a 25044x2 matrix of time and intensity. Comparison of multiple files of this size is very computer processor intensive, so further averaging was done. Files were loaded into Mathcad, where a sliding time average was applied. The program takes a preset number of data points and finds an average, which it assigns to that interval. It then moves on to the next interval and repeats the process. In this fashion, the entire data set is averaged to produce a more manageable size. See Appendix A for a more detailed description of the program. Typically, the data interval was set for 25 points and the last 44 points discarded, which produced a 1000 point file.

**Ellipsometry**

Ellipsometry, also known as polarimetry and polarization spectroscopy, can be used to obtain the thickness and optical constants of thin films.[126] Some of the advantages of this technique over others is that it is simple to operate, nondestructive, and requires no vacuum system. Measurements can be taken in a vacuum system, in air, or in a liquid.[36] Figure 3-5 shows the typical experimental arrangement. Collimated monochromatic light is passed through a polarizer (Glan-Thomson calcite prism) and a quarter-wave compensator (mica plate with 45° retardation) to give elliptically polarized

light. This is reflected off the sample surface into a second polarizer (Glan-Thomson calcite prism) that acts as an analyzer. The polarizer and analyzer are then rotated to find the maximum extinction of the reflected light.[127]

It is important to know the angle of incidence of the incoming light and its wavelength and to keep these constant throughout the measurement. Once the initial set of polarizer and analyzer settings is found, the two are rotated to find a second set of extinction conditions. The polarizer is adjusted to 90° plus the original polarizer angle. The analyzer is adjusted to 180° minus the original analyzer angle. Both are then rotated to find maximum light extinction. In order to ensure accurate measurements, the new angles should not differ from the calculated positions by more than four degrees.[128] With these data, the values of psi ($\Psi$) and delta ($\Delta$) can be determined from the relationships:

$$\Psi = \frac{180^0 - (A_2 - A_1)}{2}$$

$$\Delta = 360^0 - (P_1 + P_2)$$

where $A_2$, $A_1$, $P_2$, and $P_1$ are the second and first set of analyzer and polarizer angles, respectively.[127, 128]

Light is an electromagnetic wave and therefore must obey Maxwell's equations. As a consequence, there are certain relations that must be obeyed when light encounters a boundary between two media. First, the angle of incidence must equal the angle of reflectance. Second, in the case of one material on top of another, Snell's Law must hold:

$$n_1 \sin\theta_1 = n_0 \sin\theta_0$$

where $n_1$ and $n_0$ are the complex indices of refraction in material 1 and material 0 and $\theta_1$ and $\theta_2$ are the angles from the surface normal in material 1 and material 0.[36] Third, the Fresnel reflection coefficients are given by:

$$r_s = \frac{n_0 \cos\theta_0 - n_1 \cos\theta_1}{n_0 \cos\theta_0 + n_1 \cos\theta_1}$$

$$r_p = \frac{n_1 \cos\theta_0 - n_0 \cos\theta_1}{n_0 \cos\theta_0 + n_1 \cos\theta_1}$$

where s refers to the light vector component perpendicular to the plane of incidence and p the parallel component.[127] The plane of incidence is defined by the incident and reflected beams and the surface normal.[36] It is these last two relations that are important for the ellipsometry measurement. They are related to the $\Psi$ and $\Delta$ values obtained earlier by the following equation:

$$\frac{r_p}{r_s} = (\tan\Psi)e^{i\Delta}.$$

These equations can also be related to the reflection coefficients through the following:

$$R_s = \frac{r_{01,s} + r_{1sub,s}e^{-2i\beta}}{1 + r_{01,s}r_{1sub,s}e^{-2i\beta}}$$

$$R_p = \frac{r_{01,p} + r_{1sub,p}e^{-2i\beta}}{1 + r_{01,p}r_{1sub,p}e^{-2i\beta}}$$

where the subscripts 0, 1, and sub represent the measurement medium, film, and substrate, respectively. The film thickness, $d_1$, can be found from the equation for the phase angle, $\beta$:

$$\beta = 2\pi\left(\frac{d_1}{\lambda}\right)n_1 \cos\theta_1.$$

It is this equation that relates the index of refraction to the thickness, as well as to the phase changes due to reflection at the interface.[36, 126] There are many computer programs available that use these relations to determine film thickness or index of refraction from the $\Psi$ and $\Delta$ values found from the measured analyzer and polarizer settings. Due to time and space constraints, a more detailed discussion of the equations will not be attempted here. However, it is possible to analyze multiple films using this technique, although such analysis is very complex.[127, 129]

For the current work, two different types of ellipsometry equipment were utilized. The first was a Gaertner Scientific Corp. ellipsometer with a HeNe laser (632.8 nm) and manual polarizer and analyzer. For this apparatus, the angle was set at 70°, and the sample positioned to give reflection into the detector. Once this was set, polarizer and analyzer readings could be collected. The second piece of ellipsometry equipment used was a fully automated rotating analyzer ellipsometer. In this arrangement, a fixed polarizer is used and the analyzer is rotated to determine extinction values. Advantages of the latter include multiple wavelength capabilities and more accurate measurement of the analyzer and polarizer relative positions. The computer program also allows for multiple angles to be used to further improve analysis. Built-in data libraries for most elements and compounds make data analysis much simpler and more precise.

**Transmission Electron Microscopy (TEM)**

TEM is a powerful technique for obtaining information about the atomic structure of a material. The main requirement is that the sample is thin enough to transmit

electrons.[36, 126] Figure 3-6 shows a typical TEM setup. For the current work, TEM was used to determine coating thickness from the Si shadow masks used during deposition. One of the most difficult aspects of using TEM is sample preparation. Since coating thickness was desired in the present study, cross-sectioned samples were prepared. This is done by first thinly slicing the sample using a diamond saw. Two of these thin slices are then laid flat with the coated sides touching. Wax is used to hold the sample together. In order to obtain a region thin enough for electrons to propagate through, the sample is placed in an ion-mill. This machine uses energetic ions to sputter thin the sample. Once a hole appears, the sample is ready for analysis. By looking at regions on the periphery of the hole, films sufficiently thin for analysis yield information about the sample.

In the microscopy, electrons are scattered as they pass through the samples. It is the nature of the scattering that determines the type of information that is obtained. There are two types of scattering events: elastic and inelastic scattering. Elastic scattering is a result of Coulombic interactions of the incoming electron and the potential field of the ion cores, and it results in no loss in energy to the electron. This type of process is known as Rutherford scattering and gives rise to diffraction patterns. The magnitude of the interaction scales with the charge on the nucleus, and thus with the atomic number. Inelastic scattering is the interaction between the primary electron beam and electrons in quantum states around the nuclei or in the solid. Energy is transferred during the scattering, giving rise to spatial variation in the intensity of the transmitted beam dependent upon defects and heterogeneities.[126] By examining the intensity of the transmitted electrons, different layers and their interfaces are visible. From this, the thickness of the coating layer can be determined.

**Auger Electron Spectroscopy (AES)**

AES is a very useful tool for looking at surface compositions. By utilizing ion beam sputtering, composition versus depth is attainable. Figure 3-7 shows a typical AES setup. Ultra-high vacuum (UHV) conditions are needed to reduce surface contamination during analysis. Sample characterization takes place as follows. Energetic primary electrons (~5 keV) are focused by an electron gun onto the sample surface. These primary electrons lose energy as they traverse the sample. Similar to the process described for the TEM, some of this lost energy goes into exciting ground state electrons into empty quantum states of the atoms or into continuum energy states. The atoms have two options for recombining an electron with an available hole and returning to the ground state. These are to produce an (1) X-ray or (2) Auger electron; see Figure 3-8. Both of these processes happen simultaneously, but this analysis is concerned only with the Auger electrons. In addition, for de-excitation energies less than approximately 2000 eV, Auger electron emission dominates over X-ray emission.

Auger electrons get their energy from the atom when it relaxes back to its ground state. Therefore, they are characteristic of the energy levels of that specific atom. Once Auger electrons are ejected from the atom, they must make it through the material and be ejected without energy loss. Figure 3-9 shows the mean free path of various atomic species. Immediately obvious from this graph is the fact that none of the elements listed have an Auger electron escape depth over 30 Å. This is the reason that AES characterizes the near surface region. With the use of computers, data can now be collected directly in N(E) versus E mode and then manipulated to obtain the differential

dN(E)/dE versus E. Historically, the data was collected in differential form due to the use of an ac modulation on the signal and detection with lock-in amplifiers, as shown in Figure 3-7, but with modern detectors and computers, this is no longer necessary. Saving the data in its non-differentiated form presents advantages in noise and processing.[36] However, the differential form is best for viewing the data since it highlights the Auger peaks.[22, 36, 126]

For the current work, a Perkin-Elmer PHI660 Scanning Auger Multiprobe system was utilized. Electron beam energy was kept at 5.0 keV with a 25 μA current. Pressure in the system was around $3*10^{-8}$ Torr during sputter profiling. A 3x3 raster was used on the 3 keV $Ar^+$ ion gun during sputter analysis. Initial surface scans were collected from coated and uncoated parts of the sample to find peaks for analysis during depth profiling. The surface scans of the coated materials can give information about the uniformity of the coating within a thickness range equal to small multiples of the escape depth of the Auger electrons. Depth profiling was used to determine thickness of the coating on powders as compared to complementary coatings on Si masks.

**Scanning Cathodoluminescence (CL) in a Scanning Electron Microscope (SEM)**

Uniformity is also thought to be important to the success of the coatings. A SEM with a fiber optic attached to a spectrometer was used for producing CL maps of the sample surface. The SEM is a useful tool for magnifying the sample surface (about 10X-300,000X).[36] To produce an image, a focused electron beam is rastered across the sample surface. When the electrons enter the sample, they lose energy through inelastic collisions, as discussed above. This inelastic energy loss is transferred to the host lattice

and gives rise to a multitude of different electron energies that leave the surface. Figure 3-1 shows a plot of these different electrons. In addition, other signals can be produced, such as X-rays, light, and heat. Due to the inherent roughness of a sedimented powder screen, there are intensity variations in the CL map of the surface. In order to provide a complementary image of the surface being studied, a secondary electron (SE) image was collected. Uniformity of the coating could then be checked by comparison of the two images. The SE image provided a picture of the different phosphor surfaces. The corresponding surfaces on the CL image could then be located and studied.

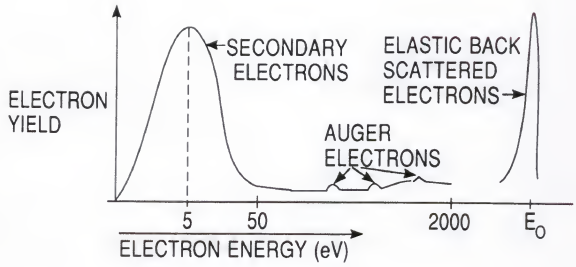


Figure 3-1 Energy distribution of electrons emitted from a sample surface under electron bombardment. The secondary electrons are used in secondary electron (SE) imaging in a scanning electron microscope (SEM). The Auger electrons are used in Auger electron spectroscopy (AES). The elastic energy is used for diffraction analysis in the transmission electron microscope (TEM).[126]

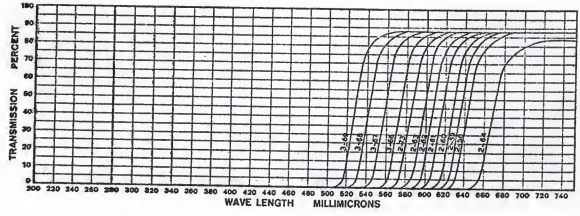


Figure 3-2 Transmission of light through a Corning glass 2-73 filter. Taken from data sheet supplied with filter.

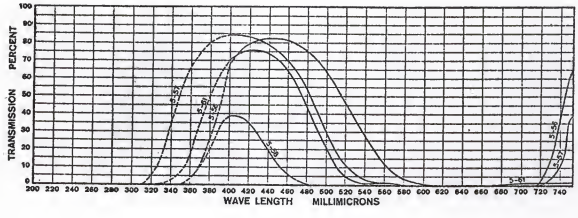


Figure 3-3 Transmission of light through a Corning glass 5-58 filter. Taken from data sheet supplied with filter.

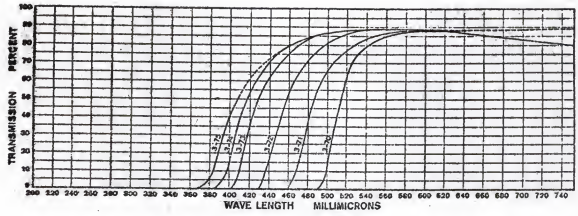


Figure 3-4 Transmission of light through a Corning glass 3-70 filter. Taken from data sheet supplied with filter.

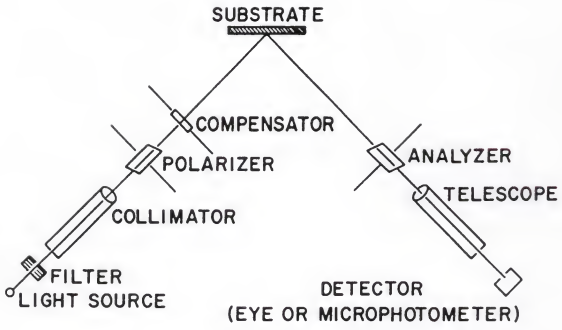


Figure 3-5 Schematic of a typical ellipsometer. Monochromatic light is passed through a polarizer and a quarter-wave compensator to give elliptically polarized light. This is reflected off the sample into the analyzer (a second polarizer). The polarizer and analyzer are rotated to determine maximum extinction of the reflected light.[126]

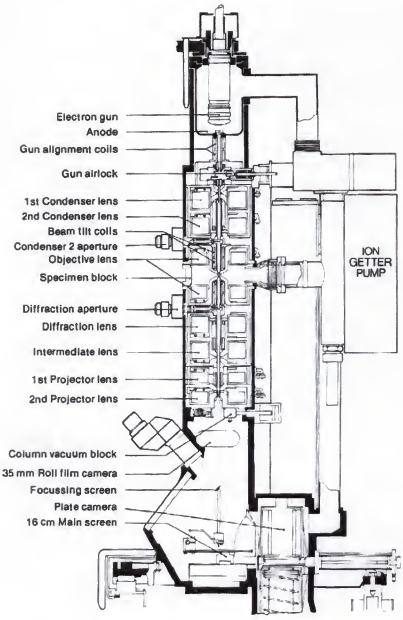


Figure 3-6 A typical transmission electron microscope. The top portion of the instrument above the specimen block is used to generate a focused high-energy electron beam. The apertures and lenses below the specimen block are used to select specific regions of the diffracted electron beam for imaging. Most instruments allow for collection of generated images on a photographic film.[36]

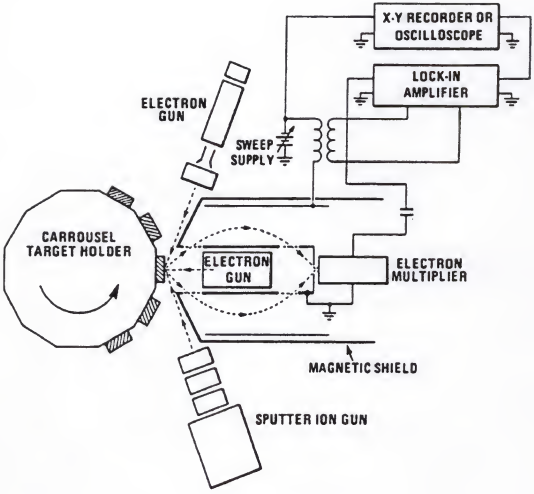


Figure 3-7 A typical Auger electron spectroscopy (AES) setup, based on a cylindrical mirror electron energy analyzer (CMA).[22]

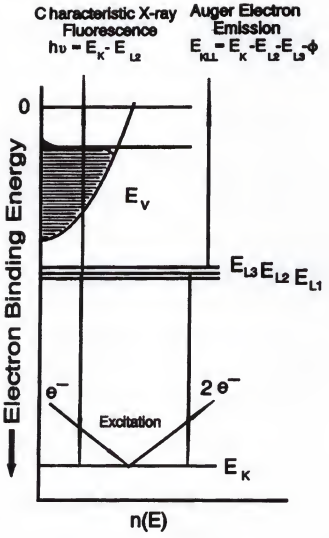


Figure 3-8 Schematic representation of the processes of X-ray fluorescence and Auger electron production. A KLL transition is shown as an example. Initial excitation comes from ejection of a core shell electron by an incident electron. Both processes occur in a material under electron beam bombardment.[22]

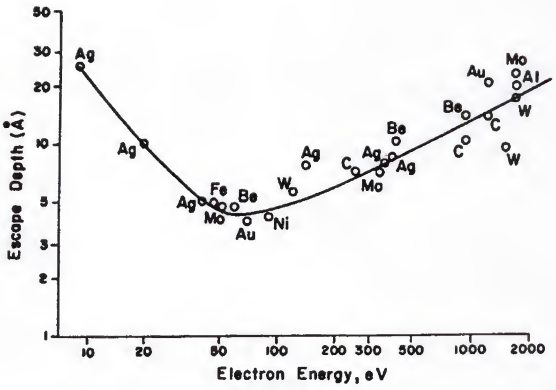


Figure 3-9 Electron escape depth as a function of initial kinetic energy. This is a measure of the average distance the electron will travel before undergoing an inelastic collision with the host lattice. It is also commonly referred to as the electron's inelastic mean free path.[22]

# CHAPTER 4
# EXPERIMENTAL RESULTS

## Introduction

Results are separated into four main categories. These include the steady-state cathodoluminescence (CL) spectra, which show the luminescence over the visible wavelength range and at multiple beam energies. Next, the effects of beam energy on steady-state CL intensities at specific wavelengths are reported. Third, pulsed CL decay curves at various beam energies and wavelengths are reported. Fourth, the coating thickness and uniformity data are presented. A list of all samples is given in Table 4.

## Cathodoluminescent Spectra

Figure 4-1 shows the cathodoluminescent spectra of $Y_2O_3$:Eu as reported in the Phosphor Technology Center of Excellence: Low Voltage Phosphor Data Sheets.[38] This figure shows the relative radiant intensity (i.e., cathodoluminescence intensity) as a function of wavelength at 1 keV and 1 $\mu A/cm^2$. The intensity has been normalized to the value of the 611 nm peak. Figures 4-2 through 4-5 depict the cathodoluminescent spectra for $Y_2O_3$:Eu with coatings of MgO deposited for 4 or 8 minutes, and $Al_2O_3$ deposited for 1.2 or 2.4 minutes, respectively. These curves show the intensity as a function of wavelength from 520 to 720 nm. Spectra are displayed for uncoated and coated samples

at beam energies of 0.8 keV, 1.4 keV, 2.5 keV, and 4 keV. Current density was kept constant at 0.16 $\mu A/cm^2$ for each measurement. From the data, it can be seen that the coating reduces the cathodoluminescent intensity over the entire wavelength range. However, no measurable change occurred in the wavelength dependence of the luminescent peaks, as will be discussed later in this section. Another feature of these graphs is that coatings of the same material deposited for longer times (which were therefore thicker) led to a larger attenuation of the intensity at all beam energies from 0.8 to 4 keV. This can be seen by comparing the intensity ratio of coated to uncoated phosphors at any given beam energy for the same coating material and time.

Figure 4-6 shows a typical cathodoluminescent spectra for $Y_2SiO_5$:Tb from 400 to 720 nm measured at 1 keV, as reported in the literature.[49] The intensity has been normalized to the main emission peak. Figures 4-7 through 4-10 are spectra of uncoated and coated $Y_2SiO_5$:Tb. Coatings of MgO, deposited for 4 and 8 minutes, and $Al_2O_3$, deposited for 2.4 and 5 minutes, are presented. No spectra are reported for the 1.2 minute $Al_2O_3$ coating on $Y_2SiO_5$:Tb because the data files were corrupted. The intensity as a function of wavelength from 460 nm to 680 nm at beam energies of 0.8 keV, 1.4 keV, 2.5 keV, and 4.0 keV are shown. Similar to the $Y_2O_3$:Eu samples, the MgO and $Al_2O_3$ coatings caused a reduction in the cathodoluminescent intensity over the entire wavelength range. Also, coatings of the same material deposited for longer times (which were therefore thicker) attenuated the luminescence more strongly. Wavelength dependence of the luminescent peaks was unaffected by the coatings.

No calibrated light source was available inside the chamber, so luminescence in Figures 4-2 to 4-5 and 4-7 to 4-10 was plotted in arbitrary units. During measurement,

the integration time of the spectrometer was adjusted to provide a main peak intensity signal that was between 80 and 90 percent of the maximum allowable intensity. This helps increase the signal-to-noise ratio. To further improve this ratio, 64 scans were collected and averaged. Sixty-four background spectra scans were also collected and averaged before each run and were subtracted from the luminescent spectra in real time. Averaging of the background spectra is needed in order to keep from introducing noise during subtraction.

All spectra in a given figure have been corrected for any differences in integration time and can therefore be directly compared against one another. However, care must be taken when comparing curves from different figures because not all figures have been normalized to the same overall integration time. This was necessitated by small changes in sample positioning and light collection between experiments. In order to compare curves from different figures, the ratio of the coated to uncoated spectra needs to be used. Since all powders of each type of phosphor are the same, the luminescence of the uncoated side should be the same for all samples of that phosphor. This is one of the main reasons for masking half of the phosphor screen during deposition. Therefore, by comparing the ratio of intensities at different beam energies, the effects of the coating can be obtained. Using this method, it can be concluded from the figures that coatings of a given material deposited for longer times show larger attenuation of the cathodoluminescence intensity, as stated in the previous paragraph.

In order to better understand the beam energy and coating effects on the CL peak positions and relative heights, spectra for beam energies from 0.8 to 4 keV were normalized to the intensity at the main emission peak. These are shown in Figures 4-11

to 4-18. It can be seen that the coatings had no effect on the peak positions and very little effect on relative peak intensities. Various luminescent peaks arise due to transitions from different energy levels (states) within the phosphor activator and host, as discussed in Chapter 2. If the coatings had altered these states, then the energy released during relaxation (recombination of excited electrons with holes to return to the ground state) would be different than that released by an uncoated phosphor. This change in energy would have caused a shift in wavelength of the emitted light. Since no such shift was observed, it can be concluded that the coatings did not alter the electronic configuration of the activators.

In addition to examining peak positions on the normalized graphs, peak height must be considered. If the peak ratios remain the same for all energies, then looking at a single peak is sufficient to see the beam energy effects for the entire spectrum. However, if the ratios change, as in the $Y_2O_3$:Eu samples, then each individual set of peaks must be analyzed because the amount of attenuation will depend upon wavelength. This will be important later when the decay of different luminescent states is measured.

The peak height ratio of the $^5D_1$ / $^5D_0$ transitions (591 nm / 611 nm) in the $Y_2O_3$:Eu samples changed not only with the coatings present, but also for the uncoated phosphor samples. This suggests that the changes are due to the phosphor itself and are not caused by the coating. The most likely explanation for the change in peak height ratios with beam energy is a change in Eu concentration near the surface of the phosphor. Tseng et al. have shown that the $^5D_1$ / $^5D_0$ intensity ratio decreases with increasing Eu concentration.[130] As the beam energy is reduced, the interaction volume moves closer to the surface. Since the $^5D_1$ / $^5D_0$ intensity ratio decreases with decreasing energy in

Figures 4-11 to 4-14, the Eu concentration is higher near the surface than in the bulk of the phosphor. This is consistent with studies on commercially prepared $Y_2O_2S$:Eu[35] and pulsed laser deposited thin films of $Y_2O_3$:Eu[39].

**Beam Energy Effects on Luminescence**

From the luminescent spectra shown in Figures 4-2 to 4-5 and 4-7 to 4-10, it can be determined that coatings attenuate the luminescence from phosphors. By plotting the intensity of luminescence versus beam energy at a specific wavelength for the coated and uncoated phosphor, the decrease in luminescence is more easily seen. By fitting curves to this data, the luminescence at any given beam energy can be predicted. Luminescence intensity values were taken from the spectra in the previous section. To account for any change in peak ratios, graphs were made for both the main peak and the next largest distinctly separate peak. For $Y_2O_3$:Eu samples, these were the 611 nm and 591 nm peaks. For the $Y_2SiO_5$:Tb samples, these were the 547 nm and 487 nm peaks. A large difference is noticeable in the $Y_2O_3$:Eu curves because of a change in the ratio of main to side peak height; see spectra in Figures 4-11 to 4-14 for clarification. Those for $Y_2SiO_5$:Tb are nearly identical because, within the range of experimental error, the normalized intensity does not change with beam energy over the wavelengths of interest.

Curves for $Y_2O_3$:Eu samples are shown in Figures 4-19 through 4-26. Plotted is the intensity, measured in arbitrary units, on a logarithmic scale, versus the electron beam energy from 0.8 to 4 keV, also on a logarithmic scale, for both coated and uncoated samples. Similar curves for the $Y_2SiO_5$:Tb samples can be seen in Figures 4-27 through 4-35. As reported above, no spectra are available for the 1.2 minute $Al_2O_3$ coating on

$Y_2SiO_5$:Tb. However, the intensity of the main 547 nm peak was recorded during measurement of these samples, and these values were used to plot Figure 4-31. This was the only peak recorded during measurement, and therefore there is no corresponding 487 nm luminescence data for this sample. The following expression shows the second order polynomial that was found to give the best fit to the data:

$$\log_{10}(y) = a_0 + a_1 \log_{10}(x) + a_2 [\log_{10}(x)]^2 .$$

Based on these data, two conclusions can be drawn. First, the relative attenuation of the luminescence by the coating decreases at higher energy, i.e., the coated and uncoated data converge at higher beam energy. This presumably is due to the larger interaction volume of the incident electrons at higher beam energy. As a result, the coating consumes a smaller percentage of the electron interaction volume at higher beam energy. Second, coatings deposited for longer times (which are therefore thicker) attenuate the luminescence more strongly. These effects are explained further in Chapter 5.

**Pulsed Cathodoluminescence**

Pulsed cathodoluminescence measurements can be used to do time-resolved studies of a phosphor's luminescence. Through the use of filters, the decay of individual sets of luminescent states can be observed. For $Y_2O_3$:Eu, the two peaks of interest lie at 535 nm and 611 nm; see Figures 4-2 through 4-5. The 535 nm line results from a transition from the $^5D_1$ state to the $^7F_1$ ground state of $Eu^{3+}$ in $Y_2O_3$. The 611 nm emission is the result of a $^5D_0$ state to $^7F_2$ ground state transition. Figure 2-7 shows these energy levels with the 611 nm transition depicted. These peaks were chosen because they represent luminescence from the two lowest lying excited states of $Eu^{3+}$. A 535 nm

bandpass and Corning glass 2-73 filter were used to select these peaks respectively; see Figure 3-2 for the Corning filter transmission versus wavelength.

For similar reasons, the two peaks of interest in $Y_2SiO_5$:Tb were 420 nm and 547 nm. The 420 nm emission arises from the $^5D_3$ to $^7F_5$ transition of $Tb^{3+}$ in $Y_2SiO_5$, while the 547 nm peak comes from the $^5D_4$ to $^7F_5$ state. Figure 2-7 shows these energy states and the 547 nm transition. Corning glass 5-58 and 3-70 filters were used respectively to look at these regions; see Figures 3-3 and 3-4 for transmission curves of these filters.

Even though the set of peaks around 591 nm in $Y_2O_3$:Eu showed slightly different attenuation than the main 611 nm peak, they were not chosen for study under pulsed conditions because these sets of peaks arise from the same initial state as the 611 nm peak. The only difference between the transitions is in the ground state. To examine the effect of different energy state transitions, a transition with the same ground state and a different initial state was studied. Thus, the 535 nm peak of $Y_2O_3$:Eu was the ideal choice. The fact that the ratio of peak height of the 611 nm peak to the 535 nm peak did not change was also beneficial in that only one attenuation curve was required for comparison. Any difference between the curves from the two filters should be a direct result of difference in the initial states of the electrons.

Figures 4-36 through 4-53 were plotted on a log-linear scale. The log scale shows the change in luminescent intensity, while the linear scale shows time. Sample current was not precisely controlled during collection of the pulsed measurements. Instead, the curves were normalized to the intensity at the end of the pulse to account for a difference in current. Pulse width was controlled by the pulse generator and was set at 10 μs. To

get an accurate end-of-pulse luminescence, the raw data files were used (after averaging the 3000 scans together, but before averaging using the Mathcad program; see Chapter 3). Files contained both time and intensity columns, which allowed for finding the correct intensity value. Background intensity found during averaging in Mathcad (see Appendix A) was subtracted from this intensity. This is necessary because the background had been subtracted from the rest of the data, and, if not accounted for, would give erroneous results.

Through the use of filters, spectral resolution of the CL decay measurements is possible. Figures 4-36 to 4-43 show these results for coatings of $Al_2O_3$ and MgO on $Y_2O_3$:Eu. Each coating corresponds to two graphs, one for each of the two filters. The data for the 2-73 filter is shown in Figures 4-36, 4-38, 4-40, and 4-42. These represent the luminescence at 611 nm originating from the $^5D_0$ state. The rise after the end of pulse and the curve maximum are attributed to feeding of this state from higher energy states (the $^5D_i$ states where i is greater than or equal to 1, as shown in Figure 2-7 and discussed in Chapter 2). Therefore, the increase in peak height and maximum at higher incident beam energies suggests that the lifetime of the upper excited states is longer at higher energies. Another interesting characteristic of these curves is that the decay behavior at long times is very similar for different beam energies. All of the beam energy dependence is contained in the peak rise and decay immediately following the end of pulse. The coatings do not have an effect on the decay rate of the luminescent states, except for that due to beam energy effects. Beam energy changes due to the coating will be discussed in Chapter 5.

The 535 nm bandpass filter data is shown in Figures 4-37, 4-39, 4-41, and 4-43. These represent luminescence from the $^5D_1$ states of $Eu^{3+}$. These curves tend to be noisier than the others, especially at lower energies. This is due to their much lower intensity, which is only about three percent of the intensity found at 611 nm (see Figures 4-11 to 4-14.) By injecting more current into the phosphor, the luminescence can be increased, but there is a limit to the amount of current that can be used. As the current is increased, the phosphor will exhibit saturation (see Chapter 2) and the background level will rise. This adds considerably to the noise in the signal and was therefore avoided. At higher energies, this was not a problem because the luminescence could be increased to desired levels before saturation. The rise in intensity after the end of pulse was much lower than for the 2-73 filter data, suggesting that the population of the upper excited states was lower than for the $^5D_0$ state. The curves also peaked sooner, which suggests that the upper excited states decay faster than lower lying states. Beam energy effects for the 535 nm data were similar to those of the 611 nm data. Lower beam energies exhibited less rise after end of pulse, peaked sooner, and decayed quicker initially. The changes in the curves due to the coatings can be attributed to a change in the incident energy of the incoming electrons.

The time-resolved intensity at various beam energies for coatings of $Al_2O_3$ and MgO on $Y_2SiO_5$:Tb are presented in Figures 4-44 through 4-53. As in the $Y_2O_3$:Eu samples, there are two graphs for each coating, one for each filter. The curves from the 3-70 filter represent luminescence originating in the $^5D_4$ state of $Tb^{3+}$ in $Y_2SiO_5$; these are shown in Figures 4-44, 4-46, 4-48, 4-50, and 4-52. As with the yittria samples, some of the curves are noisy at lower beam energies. Also similar is the rise in intensity after the

end of pulse. This is attributed to feeding of the state from higher energy states. The number of electrons transferred shows a strong dependence on beam energy. Lower excitation energy produces a luminescence that peaks at shorter times and at a lower intensity, with a corresponding quicker initial decay. This is similar to the $Y_2O_3$:Eu data, but there is a much larger variation in the $Y_2SiO_5$:Tb samples. Luminescence decay data from the next highest excited state, $^5D_3$ corresponding to 420 nm emission, are shown in Figures 4-45, 4-47, 4-49, 4-51, and 4-53. In contrast to all previous data, these show almost no rise in luminescence after the end of pulse. This suggests either that higher energy states decay on a time scale much shorter than the pulse width of 10 μsec or that $^5D_3$ state emission does not rely on electrons from higher excited states. Although all of these curves start decaying from the end of pulse, beam energy effects are still discernable. Lower incident beam energies result in a larger decay rate. This causes the curves to diverge after the end of pulse. Similar to before, the changes seen as a result of the coatings can be attributed to changes in the incident beam energy. The incident beam energy reduction as a result of the coating will be quantified in Chapter 5.

### Coating Thickness and Uniformity

To determine the effect of the coating on the cathodoluminescence generated in the phosphor particles, an accurate measurement of the thickness and uniformity of the coating is needed. Table 5 shows the thicknesses for all samples. In cases where the thickness was derived from more than one method, both values are included. These are the thicknesses derived for a uniform deposition flux onto a planar substrate, the Si mask in this case. Due to the shape of the phosphor particles, the thickness of the coating will

not be uniform across the surface. However, results derived from the Si masks will be used to determine the thickness on the phosphors in Chapter 5.

For the initial set of samples, MgO (4 min.)/$Y_2O_3$:Eu, MgO (8 min.)/$Y_2O_3$:Eu, $Al_2O_3$ (1.2 min.)/$Y_2O_3$:Eu, $Al_2O_3$ (2.4 min.)/$Y_2O_3$:Eu, and $Al_2O_3$ (1.2 min.) /$Y_2SiO_5$:Tb, the thickness was determined by assuming a linear growth rate of the film during PLD. Films of MgO and $Al_2O_3$ were grown on Si substrates for five minutes under identical conditions as during the coating of the phosphor screens. Ellipsometry was then performed using the single wavelength setup described in Chapter 3. The thickness of the $Al_2O_3$ film was determined to be 325 Å, while the MgO film was only 91 Å. Based on these numbers, the deposition times of the different materials were chosen to produce films of comparable thickness. The extrapolated thickness of the 4 min. MgO coating was 73 Å, 8 min. MgO was 146 Å, 1.2 min. $Al_2O_3$ was 78 Å, and 2.4 min. $Al_2O_3$ was 156 Å.

During the coating of the second set of samples, the 2.4 min. $Al_2O_3$ coating had to be deposited in a new chamber due to a mechanical failure with the turbo pump on the old chamber. Deposition time was adjusted to 5 min. to account for the difference in deposition rate between the two chambers, thereby producing a coating with a thickness comparable to that of a coating grown for 2.4 min. in the old chamber. The coating was otherwise deposited under the same conditions as the rest of the samples.

For the second set of samples, MgO (4 min.)/$Y_2SiO_5$:Tb, MgO (8 min.)/ $Y_2SiO_5$:Tb, $Al_2O_3$ (5 min.)/$Y_2SiO_5$:Tb, and $Al_2O_3$ (5 min. in new chamber)/$Y_2SiO_5$:Tb, the Si mask used to cover the phosphor screen during coating was used to obtain thickness measurements. It was initially hoped that having the masks from each run

would allow for more accurate determination of the coating thickness from the first set of samples, but the new set of samples was inadvertently run at a higher oxygen partial pressure than the first set. The first set of coatings had been deposited at 50 mTorr oxygen background, but the new samples were deposited at 200 mTorr oxygen. The higher pressure resulted in films much thicker than desired.

To characterize the thickness of the coatings on the Si masks from the second set of samples, ellipsometry was taken using both a fixed wavelength and a variable wavelength setup. The variable wavelength equipment provides for higher precision by using multiple wavelengths and angles. The fitting software of the multiple wavelength machine also allowed for the inclusion of a native oxide layer (18 Å was chosen) between the Si substrate and the film during film thickness calculation.

Performing thickness measurements on the single wavelength setup gave results of 268 Å for 4 min. MgO, 494 Å for 8 min. MgO, and 489 Å for 5 min. (in new chamber) $Al_2O_3$. No meaningful measurement could be taken from the mask on the 5 min. $Al_2O_3$ sample because of a thickness gradient across the surface. Next, the multiple wavelength setup (500 to 800 nm in 10 nm steps) was used to try and improve upon the accuracy of the ellipsometric measurements taken at a single wavelength. Results were similar to those found earlier: 290 Å for 4 min. MgO, 549 Å for 8 min. MgO, and 545 Å for 5 min. (in new chamber) $Al_2O_3$. As with the previous measurements, no meaningful data could be collected from the 5 min. $Al_2O_3$ mask.

Since no meaningful ellipsometry data could be collected from the mask used during the 5 min. coating of $Al_2O_3$ on $Y_2SiO_5$:Tb, a Dektak profilometer was used to attempt a measurement from this particular mask. During the coating, a metal spring clip

was used to secure the mask in place. Consequently, there was a small region of uncoated Si on the mask. By scanning from this region out into the coated area, a step profile was generated; this is shown in Figure 4-54. From this, the height of the coating was deduced to be approximately 1100 Å. As noted earlier in this section, however, the thickness varied across the mask surface.

To confirm the validity of the thickness values obtained from ellipsometry, the 5 min. coatings of MgO and $Al_2O_3$ on Si substrates deposited at 50 mTorr (used to extrapolate thickness values for first set of samples) were examined using transmission electron microscopy (TEM). Cross-sections were prepared so that the thickness of the layer could be determined. Figures 4-55 and 4-56 show the results. The measured thickness of the $Al_2O_3$ coating was around 340 Å, which is comparable to the 325 Å value found through ellipsometry. Another important aspect of Figure 4-55 is the uniformity of the layer. The MgO coating in Figure 4-56 showed discontinuous islands and a much rougher interface with the Si substrate. This may be due to the lower deposition rate of the MgO compared to the $Al_2O_3$. No diffuse scattering of the laser was observed during ellipsometry, so the numbers collected from this method are assumed to be accurate. AES data collected on a MgO coated sample, as discussed below, showed no signal from the underlying phosphor material. This suggests that the coating was continuous for that sample. The most likely explanation is that growth started out as islands and switched to layers once the islands had reached a critical density.

As a check of the uniformity of the coating, the 1.2 min. $Al_2O_3$-coated $Y_2O_3$:Eu sample was examined in an SEM using CL and secondary electron (SE) imaging. Figures 4-57 and 4-58 show the uncoated $Y_2O_3$:Eu CL and SE scans, respectively.

Figures 4-59 and 4-60 show the $Al_2O_3$ coated $Y_2O_3$:Eu CL and SE scans, respectively. All scans were collected at 1.4 keV and 2 pA. This low voltage was used so that the effect of the coating could be seen if present. At higher voltages, the interaction volume is so large that the coating's effect on the cathodoluminescence becomes negligible. It is apparent from Figure 4-57 that the CL is not uniform over the entire scan area for the uncoated material. This is most likely due to varying geometry between the surface and detector, which causes the number of collected photons to vary. By comparing the CL image to the SE image (Figure 4-58) taken over the same area, the contrast seen in the CL surface map matches changes in the surface seen in the SE image. From the images, it appears that the CL intensity variations can be correlated with changes in the surface topography. Results for the coated sample show similar behavior.

If changes in the CL intensity can be correlated to the SE image, then to examine the coating uniformity, concentration should be focused on a region that, from the SE image, would be expected to show little contrast in the CL image. If the coating were discontinuous, there should be pinholes of brighter intensity in regions that are otherwise uniform. Since no such bright spots were seen, it can be assumed that the coating is continuous within the resolution of this technique, estimated to be around 0.25 μm.

All of the coating thicknesses have been determined based on measurements taken from layers grown on Si substrates and masks. To examine the coatings on the phosphor powders, sputter Auger was performed for the 8 min. coating of MgO on $Y_2SiO_5$:Tb. Figure 4-61 shows a surface scan of the MgO layer on the Si mask. Only the Mg and O peaks are present, with no trace of the Si (the Cl and C are from surface contamination during handling). This shows that the coating is continuous and uniform

at least over a thickness approximately equal to the escape depth of an Auger electron. Figure 4-62 is a sputter profile using a 3x3 raster on the ion gun. It can be seen that after about 70 minutes, the beam penetrated through the top layer to the underlying Si substrate. This corresponds to a sputter rate of approximately 7.7 Å/min. The carbon signal is seen to drop immediately upon sputtering, which confirms that the C signal in Figure 4-61 is due to surface contamination. Figure 4-63 is a surface scan after sputtering for 95 minutes (the end of the depth profile). No trace of the MgO remains, and only the Si peak is present. Figure 4-64 is a surface scan on the coated $Y_2SiO_5$:Tb powder. As before, only the Mg and O peaks are present. In this case, the absence of a Y peak is indicative of a continuous coating. Again, the small C peak is due to surface contamination during handling. Figure 4-65 is a surface scan of the uncoated $Y_2SiO_5$:Tb powder. The spectrum shows a large drop at electron energies below 100 eV and is noisy, most likely due to sample charging by the electron beam. However, the Y peak is still visible, along with the O peak. Figure 4-66 is a depth profile on the coated area of the powder, using a 3x3 raster on the ion gun similar to the previous measurement. Due to the roughness of the surface and the incident angle of the ion gun, there was shadowing of areas on the sample. This resulted in a less sharp transition from the coating material to the underlying phosphor. A 5 sec. delay was also used between sputtering and collecting the peak heights in order to allow time for the sample to dissipate any stored charge as a result of sputtering. Figure 4-67 shows the surface scan after the 125 min. depth profile. Both the Y and Mg peaks are present. This is due to shadowing of the ion sputter beam during removal of the coating. In the Auger system used for this work, the ion sputter beam is located at a 30° angle from the sample, while

the electron beam is directly above the sample; see Figure 4-68. As a result, when a rough surface is analyzed, the electron beam may sample a small portion of the surface that is not in the direct line of sight of the ion gun. Therefore, a small signal from the original non-sputtered surface is not unexpected during each subsequent Auger analysis.

Due to the gradual transition in the powder sample shown in Figure 4-66, no exact correlation is possible with the mask data shown in Figure 4-62. However, since the transitions in both figures happened after about 60 minutes of sputtering, it is reasonable to assume that the thickness data from the masks can be used to determine the coating thickness on the powder samples. For a more exact representation of the coating on the powder surface, see the discussion of deposition from a uniform flux onto a spherical surface presented in Chapter 5.

Table 4

List of all Samples

| | Laser Energy | Rep. Rate | Pulse Duration | Oxygen Background Pressure |
|---|---|---|---|---|
| MgO (4 min) / $Y_2O_3$:Eu | 350 mJ | 10 Hz | 10 nsec | 50 mTorr |
| MgO (8 min) / $Y_2O_3$:Eu | 350 mJ | 10 Hz | 10 nsec | 50 mTorr |
| $Al_2O_3$ (1.2 min) / $Y_2O_3$:Eu | 350 mJ | 10 Hz | 10 nsec | 50 mTorr |
| $Al_2O_3$ (2.4 min) / $Y_2O_3$:Eu | 350 mJ | 10 Hz | 10 nsec | 50 mTorr |
| $Al_2O_3$ (1.2 min) / $Y_2SiO_5$:Tb | 350 mJ | 10 Hz | 10 nsec | 50 mTorr |
| $Al_2O_3$ (2.4 min) / $Y_2SiO_5$:Tb (actually 5 min in new chamber) | 350 mJ | 10 Hz | 10 nsec | 200 mTorr |
| $Al_2O_3$ (5 min) / $Y_2SiO_5$:Tb | 350 mJ | 10 Hz | 10 nsec | 200 mTorr |
| MgO (4 min) / $Y_2SiO_5$:Tb | 350 mJ | 10 Hz | 10 nsec | 200 mTorr |
| MgO (8 min) / $Y_2SiO_5$:Tb | 350 mJ | 10 Hz | 10 nsec | 200 mTorr |

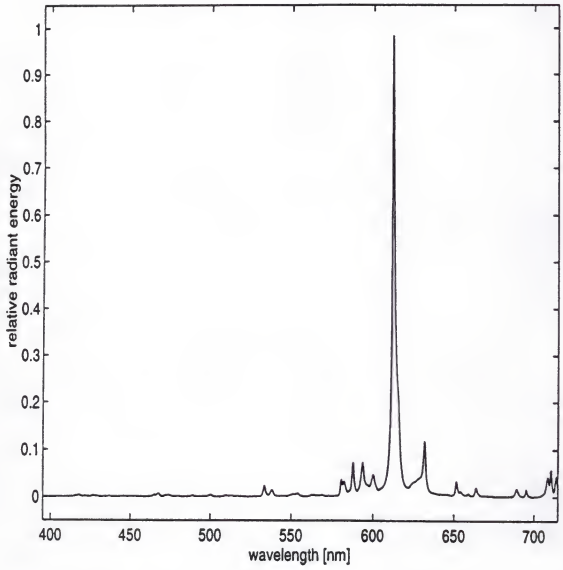


Figure 4-1 Cathodoluminescent spectrum of $Y_2O_3$:Eu over the visible wavelength range from 400 to 720 nm. The main emission peak is at 611 nm. Beam energy was 1 keV with a current density of 1 $\mu A/cm^2$.[38]

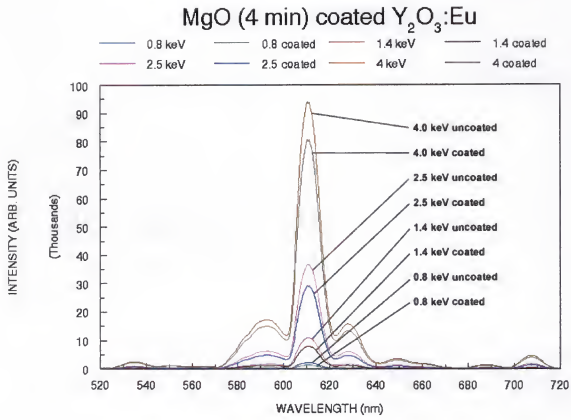


Figure 4-2 Cathodoluminescence intensity as a function of wavelength for a coating of MgO deposited for 4 minutes on $Y_2O_3$:Eu powder. Both coated and uncoated results are shown. The beam current was kept constant at 0.16 $\mu A/cm^2$, while the accelerating voltage was varied from 0.8 to 4 keV.

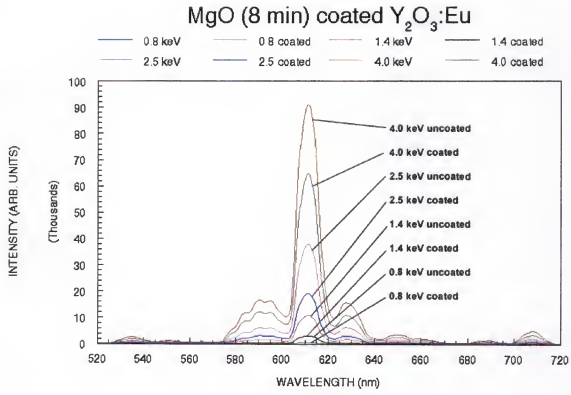


Figure 4-3 Cathodoluminescence intensity as a function of wavelength for a coating of MgO deposited for 8 minutes on $Y_2O_3$:Eu powder. Both coated and uncoated results are shown. The beam current was kept constant at 0.16 $\mu A/cm^2$, while the accelerating voltage was varied from 0.8 to 4 keV.

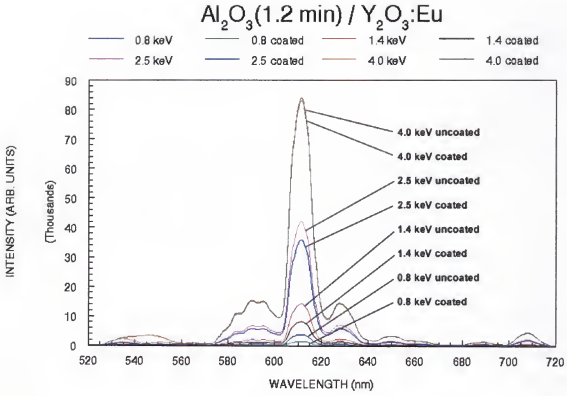


Figure 4-4 Cathodoluminescence intensity as a function of wavelength for a coating of $Al_2O_3$ deposited for 1.2 minutes on $Y_2O_3$:Eu powder. Both coated and uncoated results are shown. The beam current was kept constant at 0.16 $\mu A/cm^2$, while the accelerating voltage was varied from 0.8 to 4 keV.

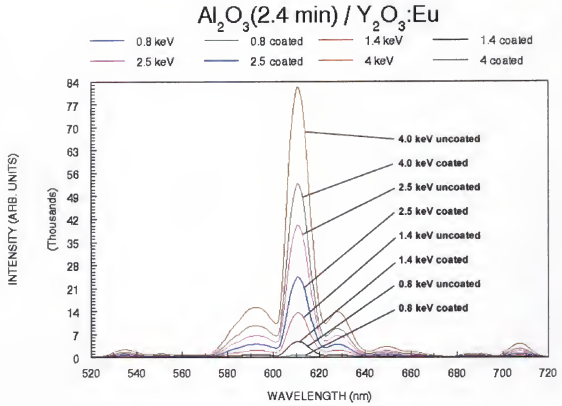


Figure 4-5 Cathodoluminescence intensity as a function of wavelength for a coating of $Al_2O_3$ deposited for 2.4 minutes on $Y_2O_3$:Eu powder. Both coated and uncoated results are shown. The beam current was kept constant at 0.16 $\mu A/cm^2$, while the accelerating voltage was varied from 0.8 to 4 keV.

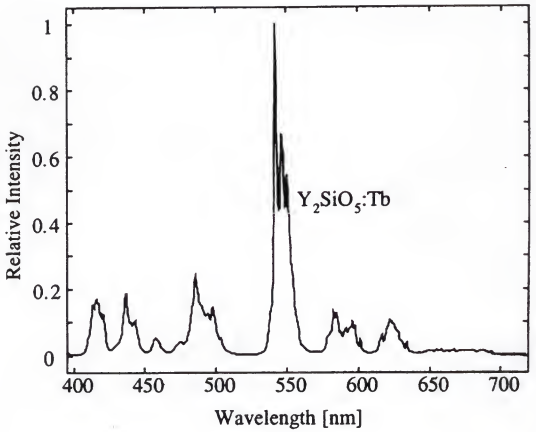


Figure 4-6 Cathodoluminescence spectrum for $Y_2SiO_5$:Tb measured at 1 keV over the visible wavelength range from 400 to 720 nm.[49]

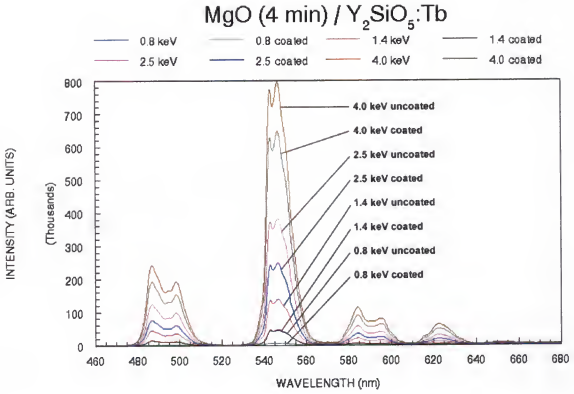


Figure 4-7 Cathodoluminescence intensity as a function of wavelength for a coating of MgO deposited for 4 minutes on $Y_2SiO_5$:Tb powder. Both coated and uncoated results are shown. The beam current was kept constant at 0.16 $\mu A/cm^2$, while the accelerating voltage was varied from 0.8 to 4 keV.

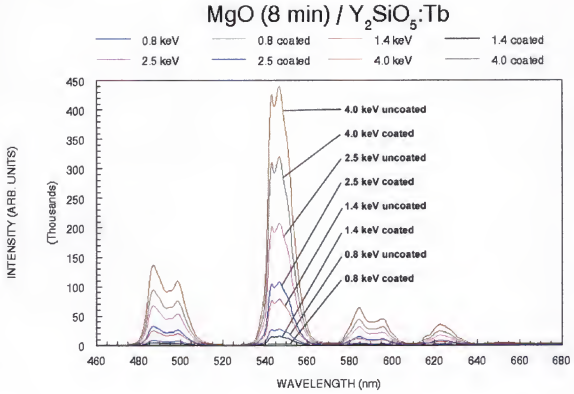


Figure 4-8 Cathodoluminescence intensity as a function of wavelength for a coating of MgO deposited for 8 minutes on $Y_2SiO_5$:Tb powder. Both coated and uncoated results are shown. The beam current was kept constant at 0.16 $\mu A/cm^2$, while the accelerating voltage was varied from 0.8 to 4 keV.

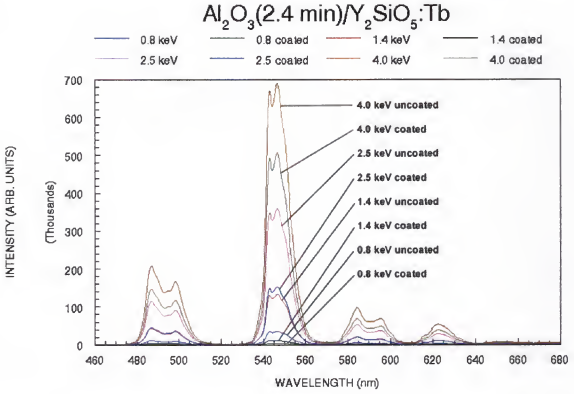


Figure 4-9 Cathodoluminescence intensity as a function of wavelength for a coating of $Al_2O_3$ deposited for 2.4 minutes on $Y_2SiO_5$:Tb powder. Both coated and uncoated results are shown. The beam current was kept constant at 0.16 $\mu A/cm^2$, while the accelerating voltage was varied from 0.8 to 4 keV.

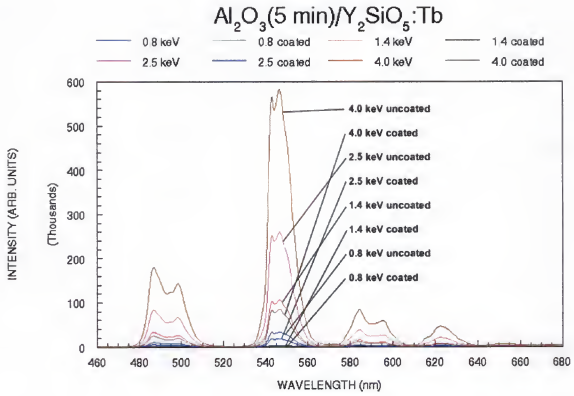


Figure 4-10 Cathodoluminescence intensity as a function of wavelength for a coating of $Al_2O_3$ deposited for 5 minutes on $Y_2SiO_5$:Tb powder. Both coated and uncoated results are shown. The beam current was kept constant at 0.16 $\mu A/cm^2$, while the accelerating voltage was varied from 0.8 to 4 keV.

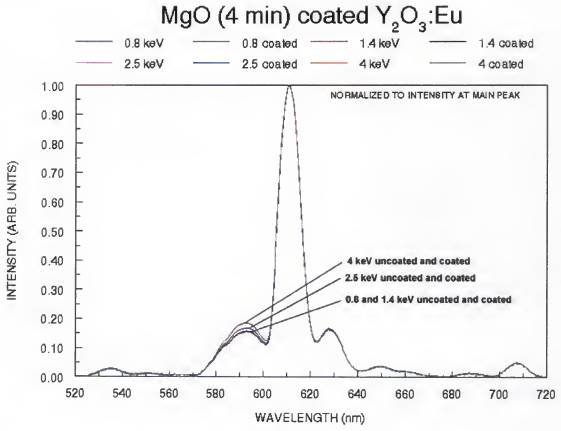


Figure 4-11 Cathodoluminescence intensity normalized to the intensity of the main 611 nm peak as a function of wavelength for a coating of MgO deposited for 4 minutes on $Y_2O_3$:Eu powder. Both coated and uncoated results are shown. The beam current was kept constant at 0.16 $\mu A/cm^2$, while the accelerating voltage was varied from 0.8 to 4 keV.

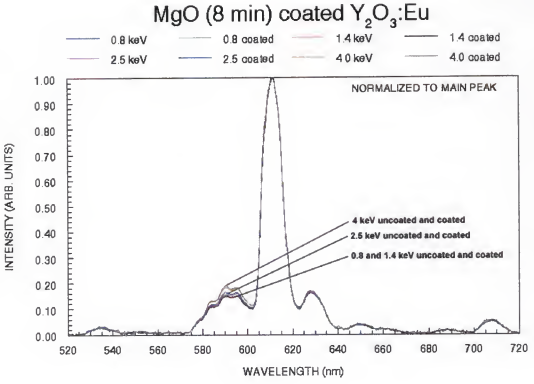


Figure 4-12 Cathodoluminescence intensity normalized to the intensity of the main 611 nm peak as a function of wavelength for a coating of MgO deposited for 8 minutes on $Y_2O_3$:Eu powder. Both coated and uncoated results are shown. The beam current was kept constant at 0.16 $\mu A/cm^2$, while the accelerating voltage was varied from 0.8 to 4 keV.

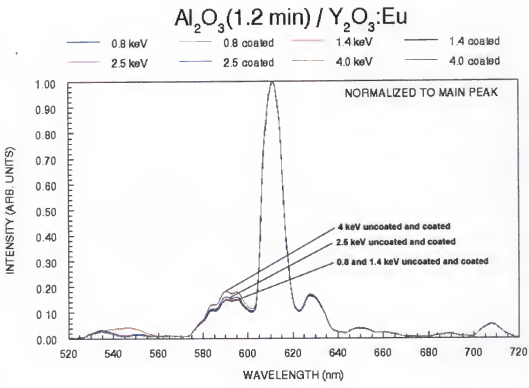


Figure 4-13 Cathodoluminescence intensity normalized to the intensity of the main 611 nm peak as a function of wavelength for a coating of $Al_2O_3$ deposited for 1.2 minutes on $Y_2O_3$:Eu powder. Both coated and uncoated results are shown. The beam current was kept constant at 0.16 $\mu A/cm^2$, while the accelerating voltage was varied from 0.8 to 4 keV.

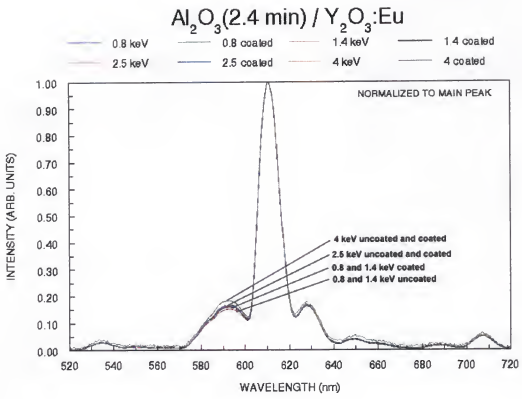


Figure 4-14 Cathodoluminescence intensity normalized to the intensity of the main 611 nm peak as a function of wavelength for a coating of $Al_2O_3$ deposited for 2.4 minutes on $Y_2O_3$:Eu powder. Both coated and uncoated results are shown. The beam current was kept constant at 0.16 $\mu A/cm^2$, while the accelerating voltage was varied from 0.8 to 4 keV.

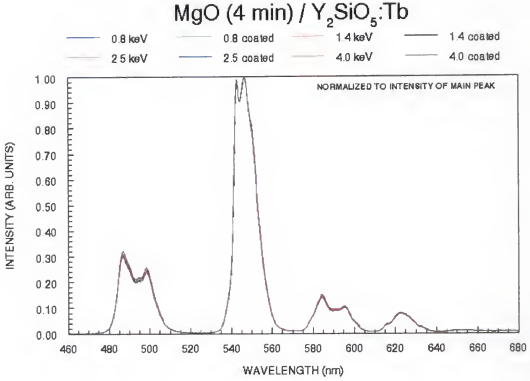


Figure 4-15 Cathodoluminescence intensity normalized to the intensity of the main 547 nm peak as a function of wavelength for a coating of MgO deposited for 4 minutes on $Y_2SiO_5$:Tb powder. Both coated and uncoated results are shown. The beam current was kept constant at 0.16 $\mu A/cm^2$, while the accelerating voltage was varied from 0.8 to 4 keV.

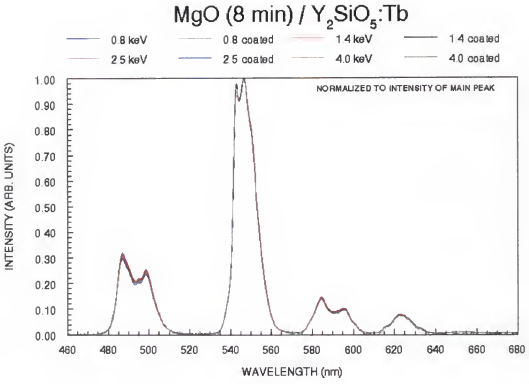


Figure 4-16 Cathodoluminescence intensity normalized to the intensity of the main 547 nm peak as a function of wavelength for a coating of MgO deposited for 8 minutes on $Y_2SiO_5$:Tb powder. Both coated and uncoated results are shown. The beam current was kept constant at 0.16 $\mu A/cm^2$, while the accelerating voltage was varied from 0.8 to 4 keV.

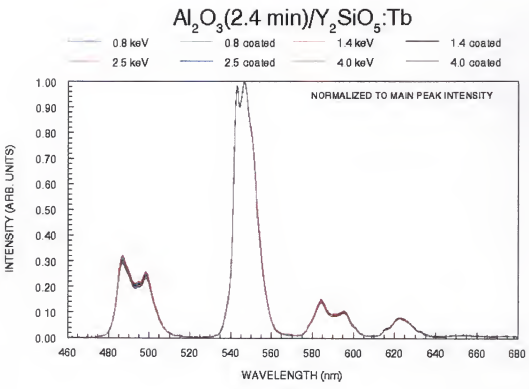


Figure 4-17 Cathodoluminescence intensity normalized to the intensity of the main 547 nm peak as a function of wavelength for a coating of $Al_2O_3$ deposited for 2.4 minutes on $Y_2SiO_5$:Tb powder. Both coated and uncoated results are shown. The beam current was kept constant at 0.16 $\mu A/cm^2$, while the accelerating voltage was varied from 0.8 to 4 keV.

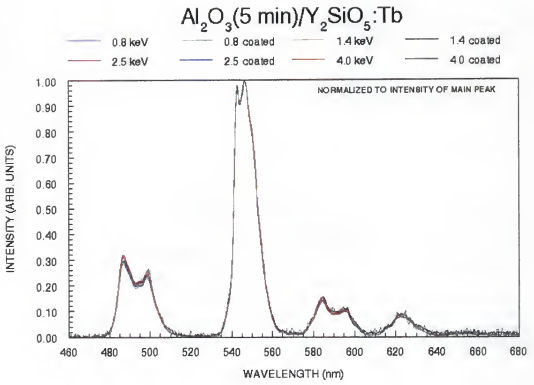


Figure 4-18 Cathodoluminescence intensity normalized to the intensity of the main 547 nm peak as a function of wavelength for a coating of $Al_2O_3$ deposited for 5 minutes on $Y_2SiO_5$:Tb powder. Both coated and uncoated results are shown. The beam current was kept constant at 0.16 $\mu A/cm^2$, while the accelerating voltage was varied from 0.8 to 4 keV.

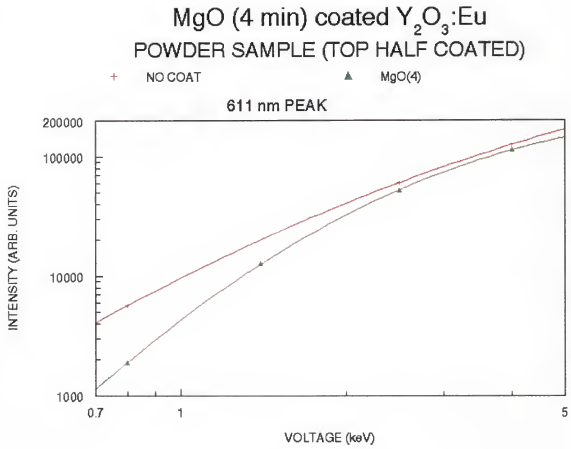


Figure 4-19 Cathodoluminescence intensity of the 611 nm peak as a function of beam energy for a coating of MgO deposited for 4 minutes on $Y_2O_3$:Eu powder. Both coated and uncoated results are shown. The beam current was kept constant at 0.16 $\mu A/cm^2$, while the accelerating voltage was varied from 0.8 to 4 keV. The slight divergence of the curves at high energy is a result of the curve fitting and is not indicative of the phosphor or coating.

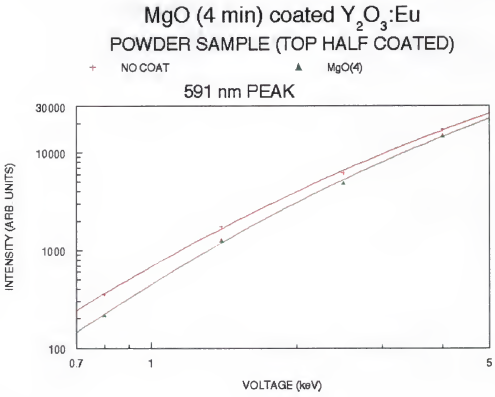


Figure 4-20 Cathodoluminescence intensity of the 591 nm peak as a function of beam energy for a coating of MgO deposited for 4 minutes on $Y_2O_3$:Eu powder. Both coated and uncoated results are shown. The beam current was kept constant at 0.16 $\mu A/cm^2$, while the accelerating voltage was varied from 0.8 to 4 keV.

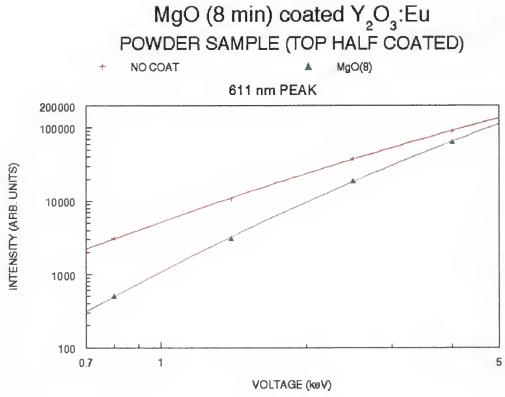


Figure 4-21 Cathodoluminescence intensity of the 611 nm peak as a function of beam energy for a coating of MgO deposited for 8 minutes on $Y_2O_3$:Eu powder. Both coated and uncoated results are shown. The beam current was kept constant at 0.16 $\mu A/cm^2$, while the accelerating voltage was varied from 0.8 to 4 keV.

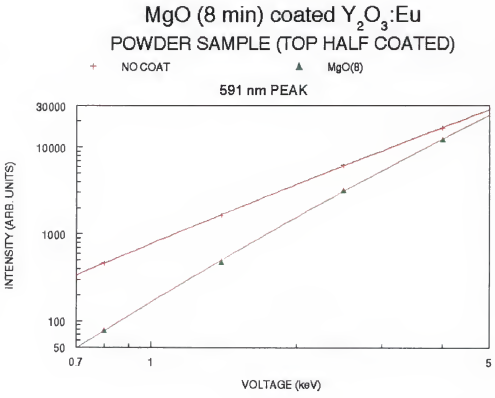


Figure 4-22 Cathodoluminescence intensity of the 591 nm peak as a function of beam energy for a coating of MgO deposited for 8 minutes on $Y_2O_3$:Eu powder. Both coated and uncoated results are shown. The beam current was kept constant at 0.16 $\mu A/cm^2$, while the accelerating voltage was varied from 0.8 to 4 keV.

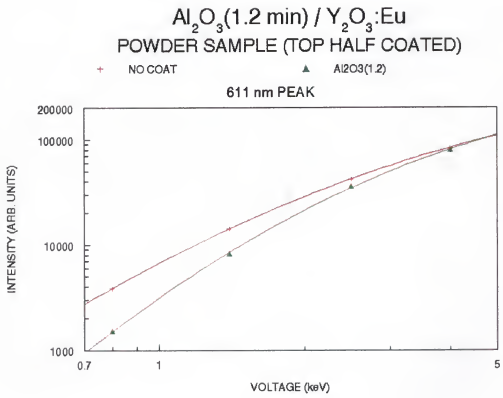


Figure 4-23 Cathodoluminescence intensity of the 611 nm peak as a function of beam energy for a coating of $Al_2O_3$ deposited for 1.2 minutes on $Y_2O_3$:Eu powder. Both coated and uncoated results are shown. The beam current was kept constant at 0.16 $\mu A/cm^2$, while the accelerating voltage was varied from 0.8 to 4 keV.

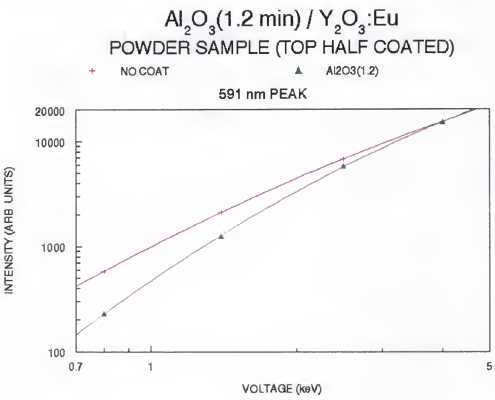


Figure 4-24 Cathodoluminescence intensity of the 591 nm peak as a function of beam energy for a coating of $Al_2O_3$ deposited for 1.2 minutes on $Y_2O_3$:Eu powder. Both coated and uncoated results are shown. The beam current was kept constant at 0.16 $\mu A/cm^2$, while the accelerating voltage was varied from 0.8 to 4 keV.

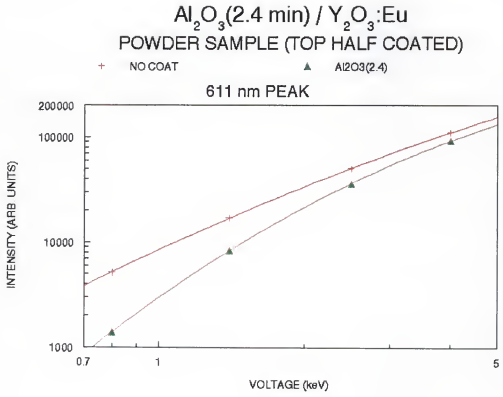


Figure 4-25 Cathodoluminescence intensity of the 611 nm peak as a function of beam energy for a coating of $Al_2O_3$ deposited for 2.4 minutes on $Y_2O_3$:Eu powder. Both coated and uncoated results are shown. The beam current was kept constant at 0.16 $\mu A/cm^2$, while the accelerating voltage was varied from 0.8 to 4 keV.

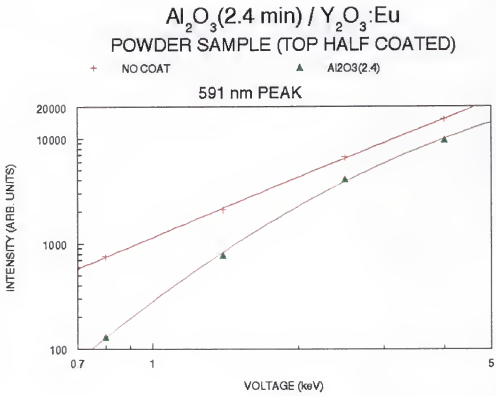


Figure 4-26 Cathodoluminescence intensity of the 591 nm peak as a function of beam energy for a coating of $Al_2O_3$ deposited for 2.4 minutes on $Y_2O_3$:Eu powder. Both coated and uncoated results are shown. The beam current was kept constant at 0.16 $\mu A/cm^2$, while the accelerating voltage was varied from 0.8 to 4 keV. The slight divergence of the curves at high energy is a result of the curve fitting and is not indicative of the phosphor or coating.

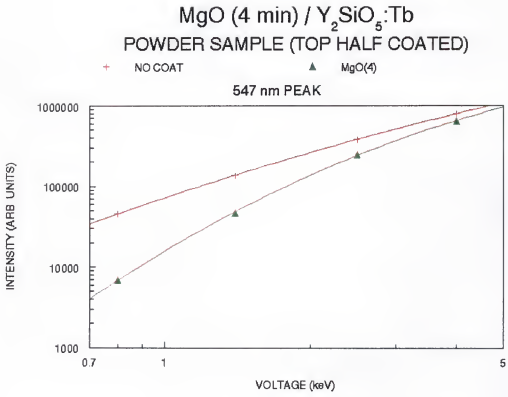


Figure 4-27 Cathodoluminescence intensity of the 547 nm peak as a function of beam energy for a coating of MgO deposited for 4 minutes on $Y_2SiO_5$:Tb powder. Both coated and uncoated results are shown. The beam current was kept constant at 0.16 $\mu A/cm^2$, while the accelerating voltage was varied from 0.8 to 4 keV.

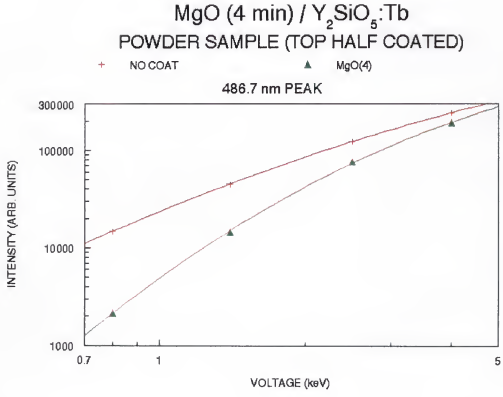


Figure 4-28 Cathodoluminescence intensity of the 486.7 nm peak as a function of beam energy for a coating of MgO deposited for 4 minutes on $Y_2SiO_5$:Tb powder. Both coated and uncoated results are shown. The beam current was kept constant at 0.16 $\mu A/cm^2$, while the accelerating voltage was varied from 0.8 to 4 keV.

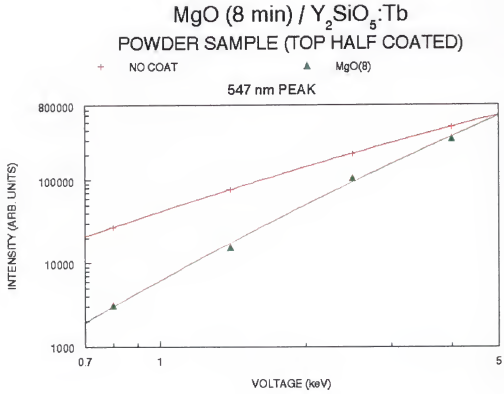


Figure 4-29 Cathodoluminescence intensity of the 547 nm peak as a function of beam energy for a coating of MgO deposited for 8 minutes on $Y_2SiO_5$:Tb powder. Both coated and uncoated results are shown. The beam current was kept constant at 0.16 $\mu A/cm^2$, while the accelerating voltage was varied from 0.8 to 4 keV.

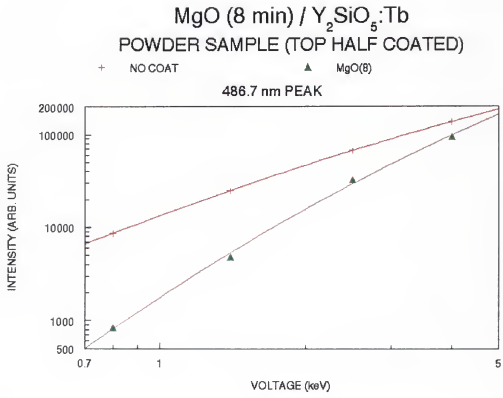


Figure 4-30 Cathodoluminescence intensity of the 486.7 nm peak as a function of beam energy for a coating of MgO deposited for 8 minutes on $Y_2SiO_5$:Tb powder. Both coated and uncoated results are shown. The beam current was kept constant at 0.16 $\mu A/cm^2$, while the accelerating voltage was varied from 0.8 to 4 keV.

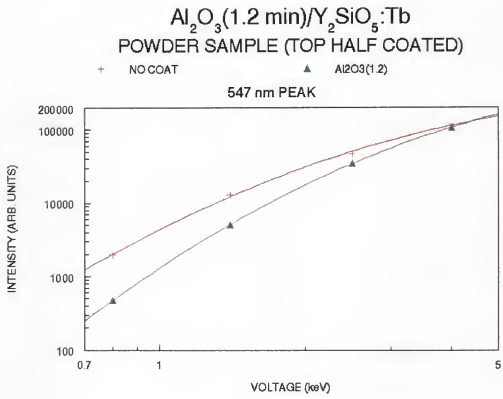


Figure 4-31 Cathodoluminescence intensity of the 547 nm peak as a function of beam energy for a coating of $Al_2O_3$ deposited for 1.2 minutes on $Y_2SiO_5$:Tb powder. Both coated and uncoated results are shown. The beam current was kept constant at 0.16 $\mu A/cm^2$, while the accelerating voltage was varied from 0.8 to 4 keV.

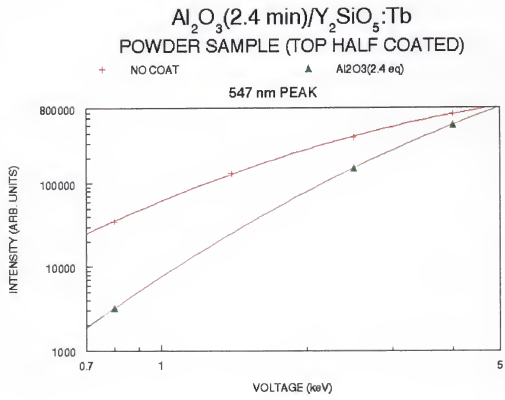


Figure 4-32 Cathodoluminescence intensity of the 547 nm peak as a function of beam energy for a coating of $Al_2O_3$ deposited for 2.4 minutes on $Y_2SiO_5$:Tb powder. Both coated and uncoated results are shown. The beam current was kept constant at 0.16 $\mu A/cm^2$, while the accelerating voltage was varied from 0.8 to 4 keV.

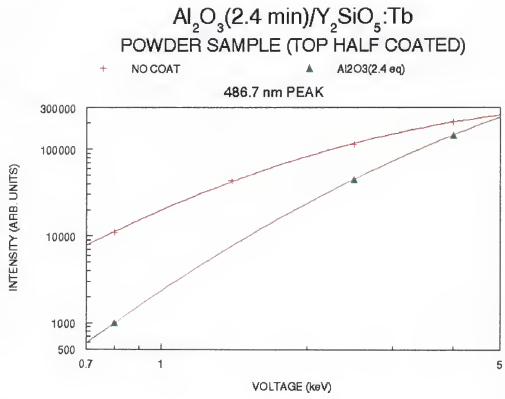


Figure 4-33 Cathodoluminescence intensity of the 486.7 nm peak as a function of beam energy for a coating of $Al_2O_3$ deposited for 2.4 minutes on $Y_2SiO_5$:Tb powder. Both coated and uncoated results are shown. The beam current was kept constant at 0.16 $\mu A/cm^2$, while the accelerating voltage was varied from 0.8 to 4 keV.

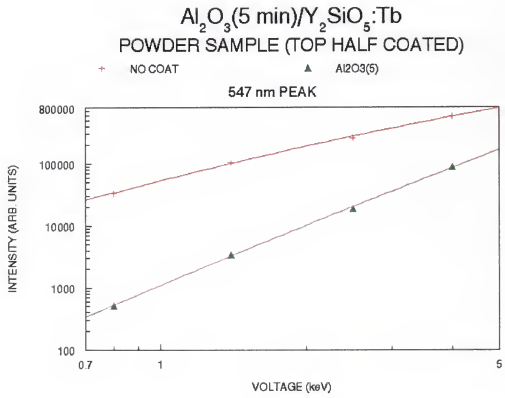


Figure 4-34 Cathodoluminescence intensity of the 547 nm peak as a function of beam energy for a coating of $Al_2O_3$ deposited for 5 minutes on $Y_2SiO_5$:Tb powder. Both coated and uncoated results are shown. The beam current was kept constant at 0.16 $\mu A/cm^2$, while the accelerating voltage was varied from 0.8 to 4 keV.

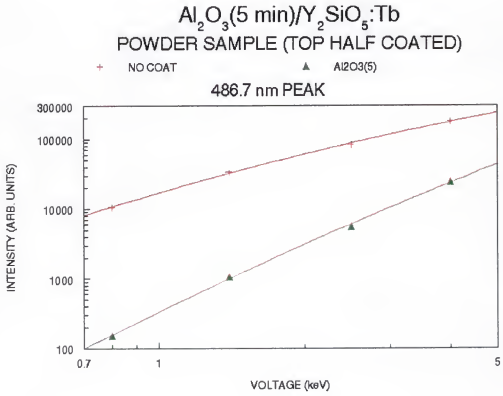


Figure 4-35 Cathodoluminescence intensity of the 486.7 nm peak as a function of beam energy for a coating of $Al_2O_3$ deposited for 5 minutes on $Y_2SiO_5$:Tb powder. Both coated and uncoated results are shown. The beam current was kept constant at 0.16 $\mu A/cm^2$, while the accelerating voltage was varied from 0.8 to 4 keV.

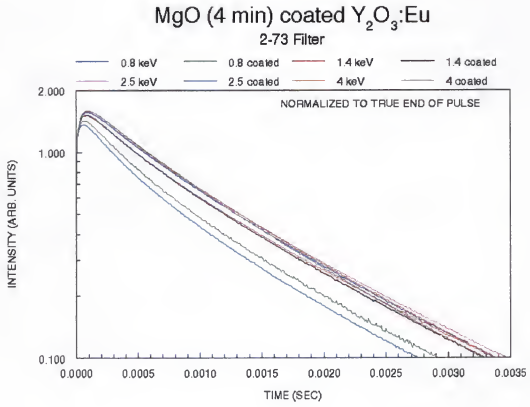


Figure 4-36 Pulsed cathodoluminescence intensity as a function of time for a coating of MgO deposited for 4 minutes on $Y_2O_3$:Eu powder. Data were collected through a Corning glass 2-73 filter. Both coated and uncoated results are shown for beam energies ranging from 0.8 to 4.0 keV. Data have been normalized to the intensity at the end of the pulse.

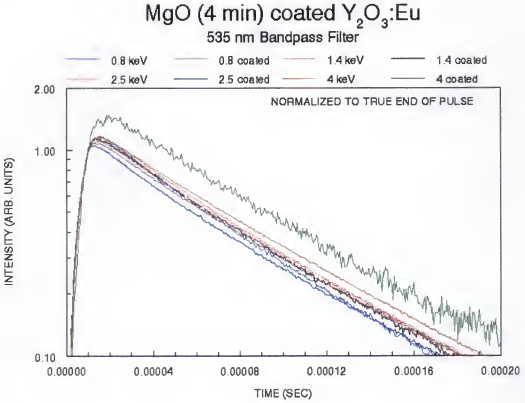


Figure 4-37 Pulsed cathodoluminescence intensity as a function of time for a coating of MgO deposited for 4 minutes on $Y_2O_3$:Eu powder. Data were collected through a 535 nm bandpass filter. Both coated and uncoated results are shown for beam energies ranging from 0.8 to 4.0 keV. Data have been normalized to the intensity at the end of the pulse. The curve for the coated sample at 0.8 keV is offset due to difficulty in accurately determining the end of pulse intensity because of a small signal-to-noise ratio.

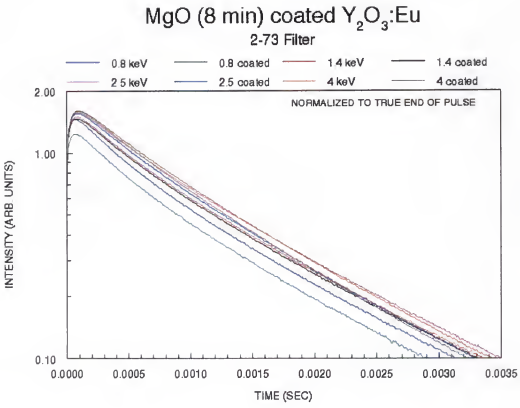


Figure 4-38 Pulsed cathodoluminescence intensity as a function of time for a coating of MgO deposited for 8 minutes on $Y_2O_3$:Eu powder. Data were collected through a Corning glass 2-73 filter. Both coated and uncoated results are shown for beam energies ranging from 0.8 to 4.0 keV. Data have been normalized to the intensity at the end of the pulse.

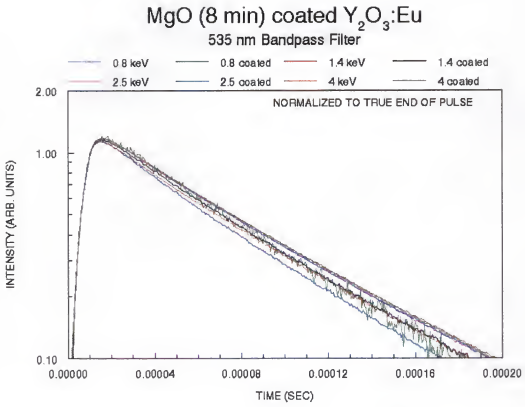


Figure 4-39 Pulsed cathodoluminescence intensity as a function of time for a coating of MgO deposited for 8 minutes on $Y_2O_3$:Eu powder. Data were collected through a 535 nm bandpass filter. Both coated and uncoated results are shown for beam energies ranging from 0.8 to 4.0 keV. Data have been normalized to the intensity at the end of the pulse.

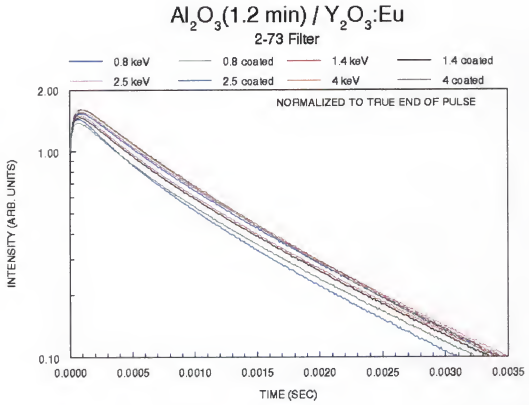


Figure 4-40 Pulsed cathodoluminescence intensity as a function of time for a coating of $Al_2O_3$ deposited for 1.2 minutes on $Y_2O_3$:Eu powder. Data were collected through a Corning glass 2-73 filter. Both coated and uncoated results are shown for beam energies ranging from 0.8 to 4.0 keV. Data have been normalized to the intensity at the end of the pulse.

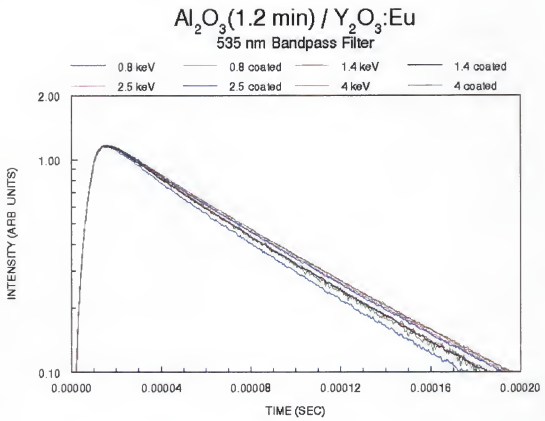


Figure 4-41 Pulsed cathodoluminescence intensity as a function of time for a coating of $Al_2O_3$ deposited for 1.2 minutes on $Y_2O_3$:Eu powder. Data were collected through a 535 nm bandpass filter. Both coated and uncoated results are shown for beam energies ranging from 0.8 to 4.0 keV. Data have been normalized to the intensity at the end of the pulse.

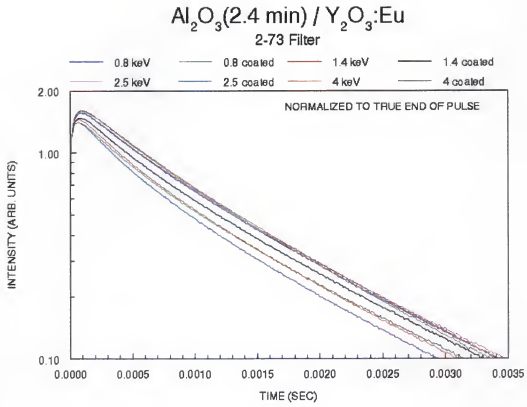


Figure 4-42 Pulsed cathodoluminescence intensity as a function of time for a coating of $Al_2O_3$ deposited for 2.4 minutes on $Y_2O_3$:Eu powder. Data were collected through a Corning glass 2-73 filter. Both coated and uncoated results are shown for beam energies ranging from 0.8 to 4.0 keV. Data have been normalized to the intensity at the end of the pulse.

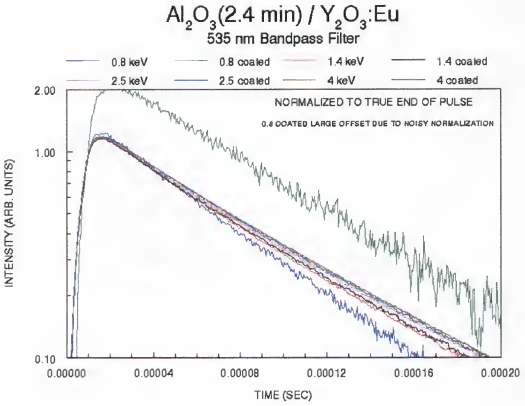


Figure 4-43 Pulsed cathodoluminescence intensity as a function of time for a coating of $Al_2O_3$ deposited for 2.4 minutes on $Y_2O_3$:Eu powder. Data were collected through a 535 nm bandpass filter. Both coated and uncoated results are shown for beam energies ranging from 0.8 to 4.0 keV. Data have been normalized to the intensity at the end of the pulse. The curve for the coated sample at 0.8 keV is offset due to difficulty in accurately determining the end of pulse intensity because of a small signal-to-noise ratio.

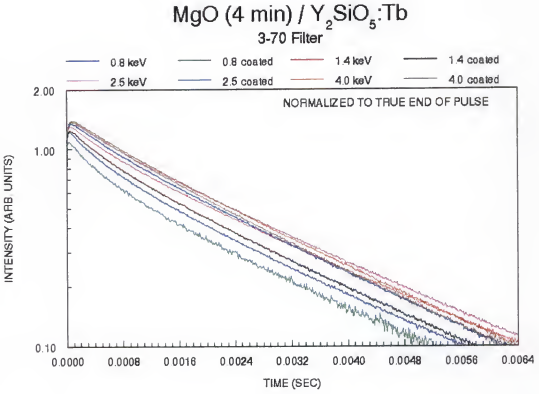


Figure 4-44 Pulsed cathodoluminescence intensity as a function of time for a coating of MgO deposited for 4 minutes on $Y_2SiO_5$:Tb powder. Data were collected through a Corning glass 3-70 filter. Both coated and uncoated results are shown for beam energies ranging from 0.8 to 4.0 keV. Data have been normalized to the intensity at the end of the pulse.

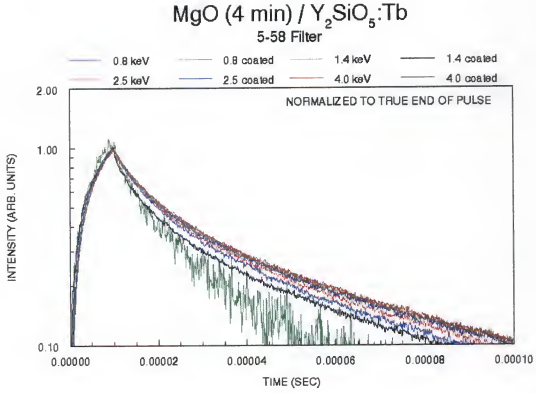


Figure 4-45 Pulsed cathodoluminescence intensity as a function of time for a coating of MgO deposited for 4 minutes on $Y_2SiO_5$:Tb powder. Data were collected through a Corning glass 5-58 filter. Both coated and uncoated results are shown for beam energies ranging from 0.8 to 4.0 keV. Data have been normalized to the intensity at the end of the pulse.

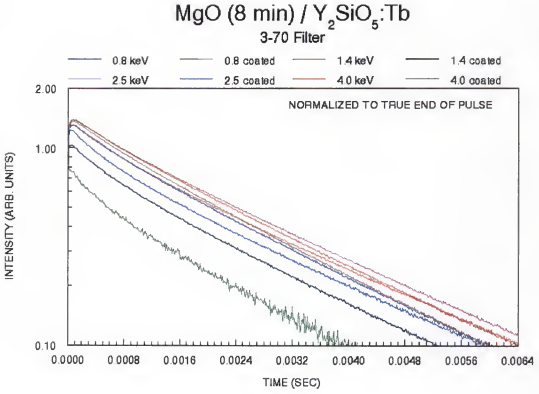


Figure 4-46 Pulsed cathodoluminescence intensity as a function of time for a coating of MgO deposited for 8 minutes on $Y_2SiO_5$:Tb powder. Data were collected through a Corning glass 3-70 filter. Both coated and uncoated results are shown for beam energies ranging from 0.8 to 4.0 keV. Data have been normalized to the intensity at the end of the pulse.

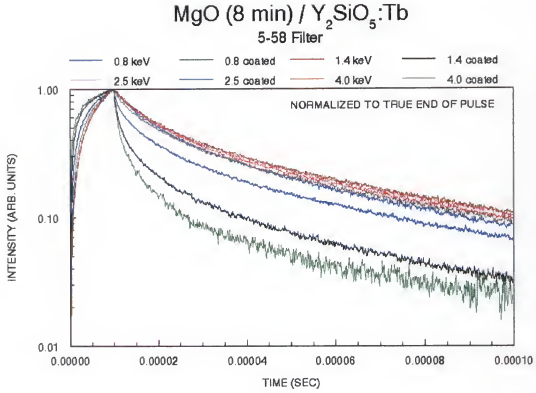


Figure 4-47 Pulsed cathodoluminescence intensity as a function of time for a coating of MgO deposited for 8 minutes on $Y_2SiO_5$:Tb powder. Data were collected through a Corning glass 5-58 filter. Both coated and uncoated results are shown for beam energies ranging from 0.8 to 4.0 keV. Data have been normalized to the intensity at the end of the pulse.

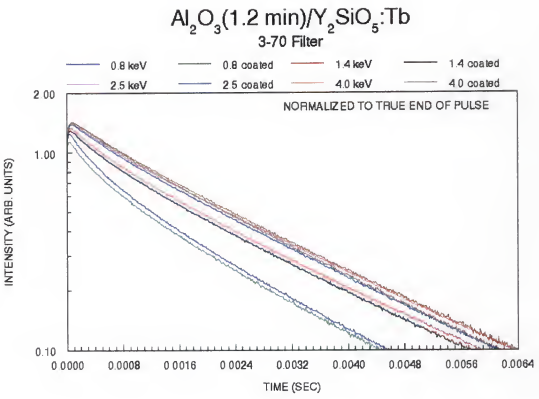


Figure 4-48 Pulsed cathodoluminescence intensity as a function of time for a coating of $Al_2O_3$ deposited for 1.2 minutes on $Y_2SiO_5$:Tb powder. Data were collected through a Corning glass 3-70 filter. Both coated and uncoated results are shown for beam energies ranging from 0.8 to 4.0 keV. Data have been normalized to the intensity at the end of the pulse.

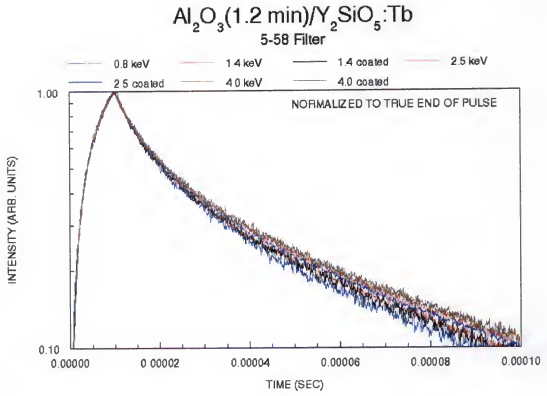


Figure 4-49 Pulsed cathodoluminescence intensity as a function of time for a coating of $Al_2O_3$ deposited for 1.2 minutes on $Y_2SiO_5$:Tb powder. Data were collected through a Corning glass 5-58 filter. Both coated and uncoated results are shown for beam energies ranging from 0.8 to 4.0 keV. Data have been normalized to the intensity at the end of the pulse.

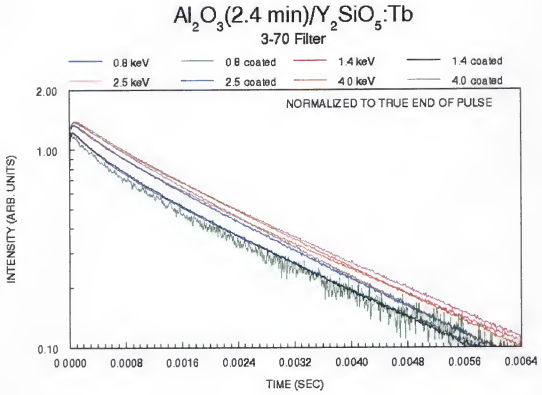


Figure 4-50 Pulsed cathodoluminescence intensity as a function of time for a coating of $Al_2O_3$ deposited for 2.4 minutes on $Y_2SiO_5$:Tb powder. Data were collected through a Corning glass 3-70 filter. Both coated and uncoated results are shown for beam energies ranging from 0.8 to 4.0 keV. Data have been normalized to the intensity at the end of the pulse.

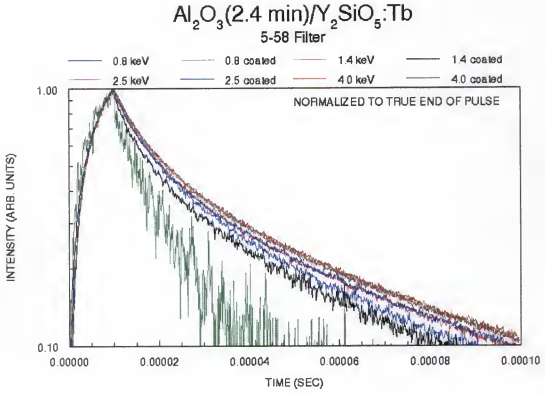


Figure 4-51 Pulsed cathodoluminescence intensity as a function of time for a coating of $Al_2O_3$ deposited for 2.4 minutes on $Y_2SiO_5$:Tb powder. Data were collected through a Corning glass 5-58 filter. Both coated and uncoated results are shown for beam energies ranging from 0.8 to 4.0 keV. Data have been normalized to the intensity at the end of the pulse.

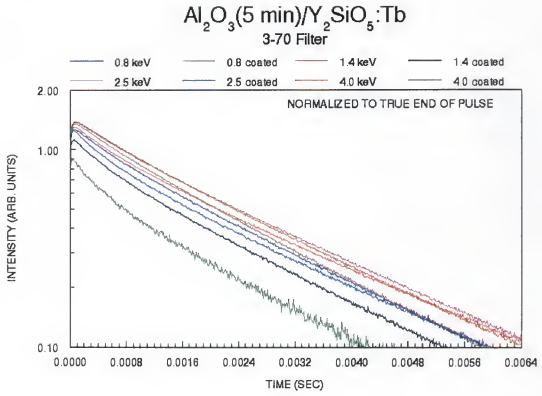


Figure 4-52 Pulsed cathodoluminescence intensity as a function of time for a coating of $Al_2O_3$ deposited for 5 minutes on $Y_2SiO_5$:Tb powder. Data were collected through a Corning glass 3-70 filter. Both coated and uncoated results are shown for beam energies ranging from 0.8 to 4.0 keV. Data have been normalized to the intensity at the end of the pulse.

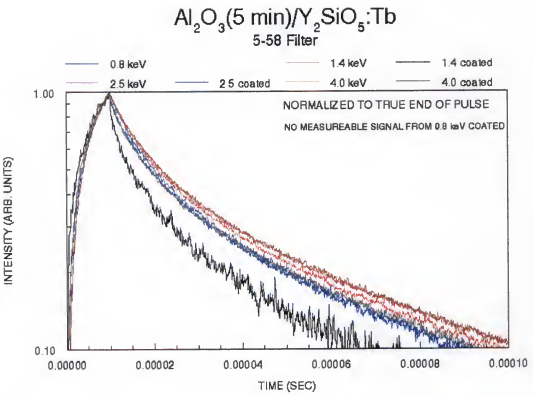


Figure 4-53 Pulsed cathodoluminescence intensity as a function of time for a coating of $Al_2O_3$ deposited for 5 minutes on $Y_2SiO_5$:Tb powder. Data were collected through a Corning glass 5-58 filter. Both coated and uncoated results are shown for beam energies ranging from 0.8 to 4.0 keV. Data have been normalized to the intensity at the end of the pulse. No measurable signal could be obtained from the coated sample at 0.8 keV.

Table 5

Thickness of coatings on samples based on measurements taken from Si shadow masks.

| | Thickness (Å) |
|---|---|
| MgO (4 min) / $Y_2O_3$:Eu | 73 (a) |
| MgO (8 min) / $Y_2O_3$:Eu | 146 (a) |
| $Al_2O_3$ (1.2 min) / $Y_2O_3$:Eu | 78 (a) |
| $Al_2O_3$ (2.4 min) / $Y_2O_3$:Eu | 156 (a) |
| $Al_2O_3$ (1.2 min) / $Y_2SiO_5$:Tb | 78 (a) |
| $Al_2O_3$ (5 min) / $Y_2SiO_5$:Tb (grown in new chamber) | 545 (b) and 489 (c) |
| $Al_2O_3$ (5 min) / $Y_2SiO_5$:Tb | ~ 1100 (d) |
| MgO (4 min) / $Y_2SiO_5$:Tb | 290 (b) and 268 (c) |
| MgO (8 min) / $Y_2SiO_5$:Tb | 549 (b) and 494 (c) |

(a) Based on a linear growth rate extrapolation of measurements taken from films of the same materials grown on Si substrates for 5 minutes under identical conditions. $Al_2O_3$ film (5 minutes) = 325 Å from ellipsometry and about 340 Å from TEM MgO film (5 minutes) = 91 Å from ellipsometry

(b) Data taken on multiple wavelength ellipsometer and fit assuming an 18 Å $SiO_2$ film between the substrate and film due to oxidation of the Si.

(c) Data taken on single wavelength ellipsometer.

(d) Approximation made from step height on stylus profilometer.

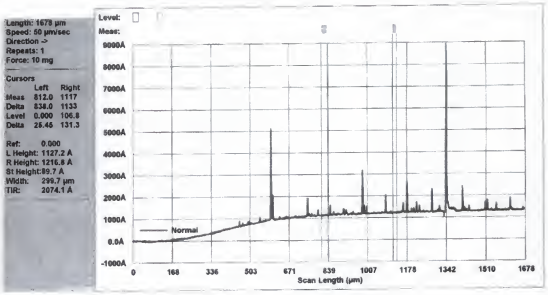


Figure 4-54 Stylus profilometer output showing the step between bare Si and $Al_2O_3$ film on a shadow mask used during 5 minute deposition of $Al_2O_3$ onto $Y_2SiO_5$:Tb powder. The measured height is approximately 1150 Å.

Figure 4-55 Transmission electron microscopy (TEM) image of an $Al_2O_3$ film on a Si substrate deposited by PLD at 50 mTorr oxygen. This thickness was used to confirm the ellipsometry results, and these measurements were used to extrapolate the thicknesses for the earlier samples. The darkest region is the Si substrate. The light gray region on the right side of the image is the epoxy used during cross-section sample preparation. The film is located in the middle and is a medium gray in color.

Figure 4-56 Transmission electron microscopy (TEM) image of a MgO film on a Si substrate deposited by PLD at 50 mTorr oxygen. The dark islands are the MgO. The medium gray region at the bottom is the Si substrate. The light gray region at the top is the epoxy used during cross-section sample preparation.

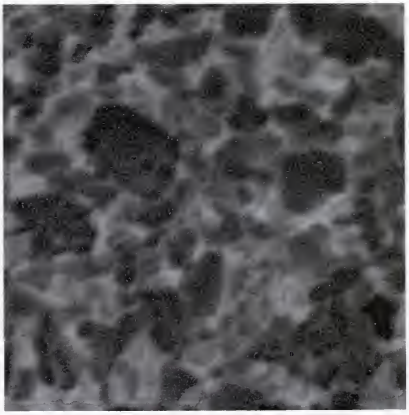

Figure 4-57 A 4000X cathodoluminescence scan of an uncoated $Y_2O_3$:Eu powder taken in a scanning electron microscope. Beam energy was 1.4 keV. For a size marker, see Figure 4-58.

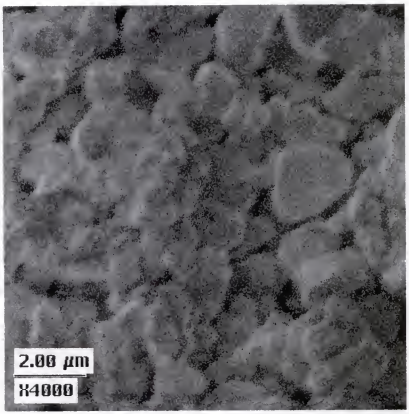


Figure 4-58 A 4000X secondary electron image of an uncoated $Y_2O_3$:Eu powder taken in a scanning electron microscope. Beam energy was 1.4 keV.

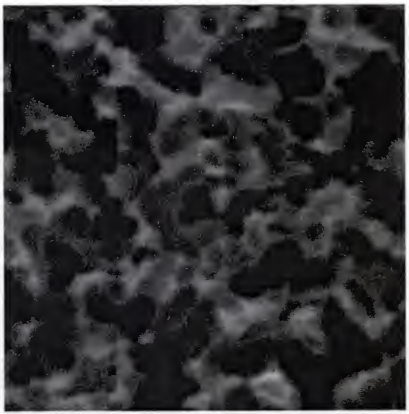

Figure 4-59 A 4000X cathodoluminescence scan of an $Al_2O_3$ coating deposited for 1.2 minutes onto $Y_2O_3$:Eu powder. The image was taken in a scanning electron microscope. Beam energy was 1.4 keV. For a size marker, see Figure 4-60.

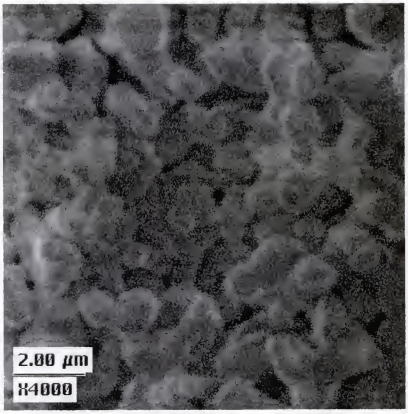


Figure 4-60 A 4000X secondary electron image of an $Al_2O_3$ coating deposited for 1.2 minutes onto $Y_2O_3$:Eu powder. The image was taken in a scanning electron microscope. Beam energy was 1.4 keV.

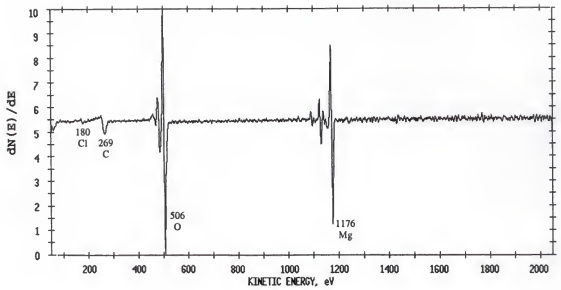


Figure 4-61 Auger electron spectroscopy (AES) surface scan of a MgO film, deposited for 8 minutes using PLD, on a Si shadow mask.

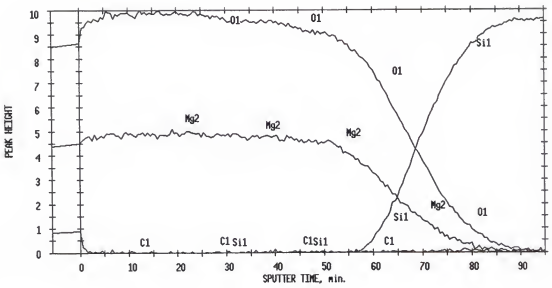


Figure 4-62 Sputter AES depth profile of a MgO film on a Si shadow mask. The area analyzed is the same as in Figure 4-61. A 3x3 raster was used on the ion sputter gun.

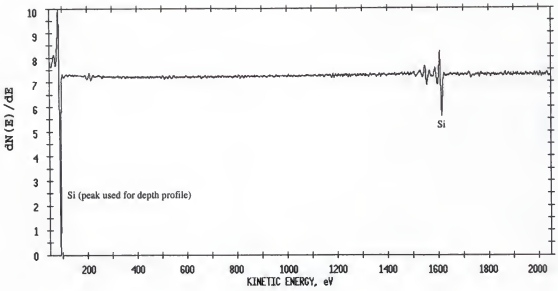


Figure 4-63 AES surface scan after depth profiling on a MgO-coated Si shadow mask. This is the same area as in Figure 4-62. The trace shows complete removal of the MgO film.

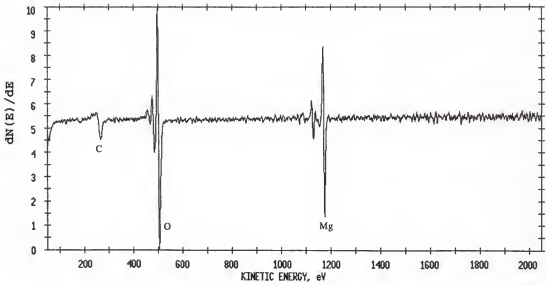


Figure 4-64 AES surface scan of a MgO film deposited for 8 minutes on $Y_2iO_5$:Tb powder. The scan shows that the coating is continuous and uniform within the escape depth of Auger electrons.

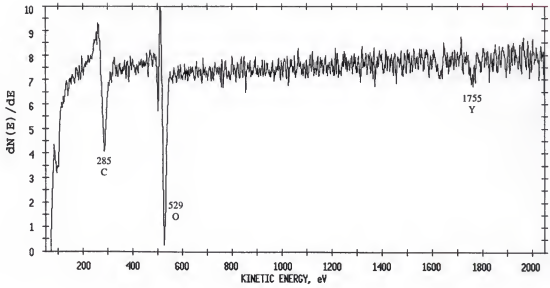


Figure 4-65 AES surface scan of uncoated $Y_2SiO_5$:Tb powder. The large decrease in the signal at low energies is due to charging of the sample under the electron beam.

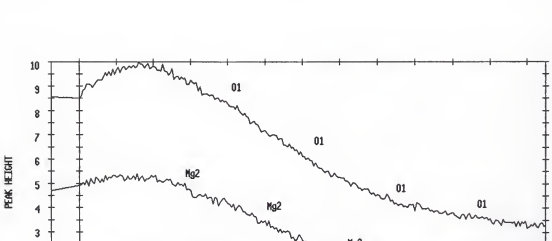


Figure 4-66 AES depth profile of MgO deposited for 8 min on $Y_2SiO_5$:Tb powder. A 3x3 raster was used on the ion sputter gun. A 5 second delay was used after sputtering and before collection of the Auger signal to improve the noise.

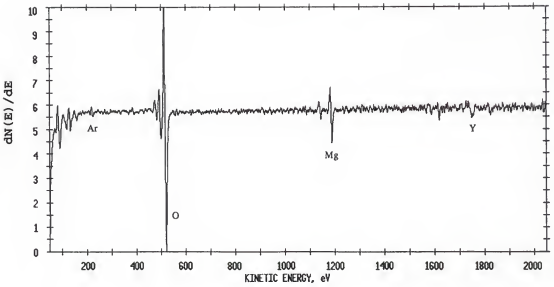


Figure 4-67 AES surface scan after the sputter depth profile of Figure 4-66 was taken. The Mg signal that is still present is due to shadowing of the sputter ion beam. The shadowing effect is a result of the uneven height of the particles.

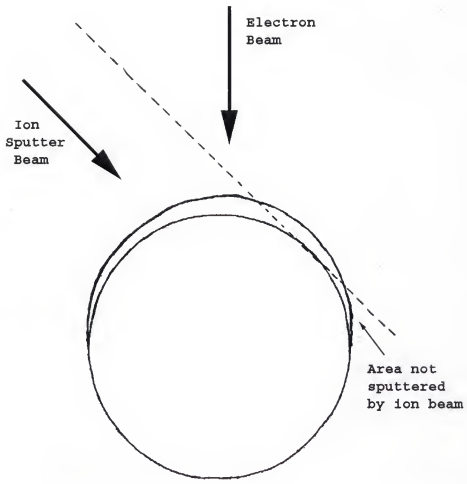


Figure 4-68 Schematic depicting shadowing of the ion sputter beam due to the spherical shape of the phosphor powder surface. The area depicted in the image will not be sputtered by the ion beam, however, it will be detected in the AES surface profile. As a result, there will be a small signal from the coating constituents in all of the AES measurements regardless of sputter time.

CHAPTER 5
MODELING OF RESULTS

## Introduction

In Chapter 4 and the literature review, it was demonstrated that coatings applied to phosphor powders attenuate their luminescence under electron beam excitation. In this chapter, a model will be presented to explain and predict this decrease in luminescence. First, a simple "dead layer" model will be assumed. Then corrections will be added to enhance the accuracy of the initial model. Corrections will take into account (1) the contribution to the luminescence of the incident angle of incoming electrons, (2) the uniformity of the coating, and (3) the electron energy loss at low energies. Consideration will be given to the backscattering coefficient due to the coating and the index of refraction, although it was found that neither was necessary for accurate prediction of the luminescence from the coated phosphors.

## Energy Loss in Dead Layer

When an electron enters a solid, it loses energy through inelastic collisions with electrons of host lattice atoms. This energy is used to excite electrons into upper energy levels. These excited electrons can then recombine with an available hole to produce radiation, heat, X-rays, Auger electrons, etc. In a luminescent material, some of the excited electrons will recombine at an activator site to produce visible light. In a

non-luminescent material, the energy released during recombination will be used in one of the other processes mentioned above. A non-luminescent material on top of a luminescent one is therefore called a "dead layer" because it absorbs energy that could be used in the luminescent material to generate light.

Initially, a calculation is made to determine the energy of an electron at any point along its trajectory into the solid. Empirically, it is found that the cathodoluminescent (CL) intensity, L, follows the relationship:

$$L = B * E_0^{\ y} \qquad [5.1]$$

where $E_0$ is the incident beam energy, y is a material constant usually in the range of 1.2 to 2.0 (its exact value will not be important for this model), and B is a constant dependent upon the specific luminescent material. This equation allows for calculation of the intensity of the light emitted from the sample.

According to the Rao-Sahib and Wittry correction to the Bethe stopping power equation (cited in Chapter 2), the energy loss per incremental electron travel distance (i.e., the stopping power) can be expressed as:[30]

$$\frac{\partial E}{\partial z} = -\frac{2}{3a} E^{-½} \qquad [5.2]$$

where z is the distance along the trajectory, E is the energy at point z along the primary trajectory, and a is a constant dependent upon the material. By taking the integral of Equation 5.2, the energy E at any point z along the trajectory can be related to the incident energy $E_0$ through:

$$E = \left( E_0^{\,½} - \frac{z}{a} \right)^{⅔}. \qquad [5.3]$$

Given the above three equations, the change in luminescence along the trajectory can be found to be:

$$\frac{\partial L}{\partial z} = \frac{2yB}{3a}\left(E_0^{1/2} - \frac{z}{a}\right)^{\frac{2\gamma}{3}-1}. \qquad [5.4]$$

This can be checked for validity by integrating over the entire trajectory range. This range, which will be referred to as $z_r$, can be found by determining when the electron energy has reached zero. Equation 5.3 then becomes:

$$0 = \left(E_0^{1/2} - \frac{z_r}{a}\right)^{3/2}$$

or

$$z_r = aE_0^{1/2}. \qquad [5.5]$$

The total luminescence is then found by integrating the change in luminescence from the surface (z = 0) to the end of range $z_r$:

$$L = \int_0^{z_r} \frac{\partial L}{\partial z} dz .$$

Solving the integral after plugging in Equations 5.4 and 5.5 yields:

$$L = \frac{2yB}{3a}\left(E_0^{1/2} - \frac{z}{a}\right)^{2\gamma/3}\left(\frac{-3a}{2y}\right)\Bigg|_0^{z_r} = B * E_0^{\ y}. \qquad [5.6]$$

Comparison of Equations 5.1 and 5.6 reveals that they are identical. Thus Equation 5.4 is self-consistent.

In order to calculate the effect of the coating on the luminescence of the underlying phosphor, it was assumed that the coating only acts to reduce the energy of

the incoming electron before it can reach the phosphor/coating interface. It then becomes necessary to determine the energy of an electron upon exiting a material of a known thickness. Equation 5.3 provides just such an answer. The parameters that will be needed are the path length in the dead layer ($z_{rd}$), the incident energy ($E_0$), and the constant (a) for the coating material. By Equation 5.5, the constant (a) is related to the incident energy and the total range of an electron in a bulk sample of the coating material ($z_{rb}$). Using Equations 5.3 and 5.5, the electron energy upon exiting the dead layer ($E_1$) can be found to be:

$$E_1 = E_0\left(1 - \frac{z_{rd}}{z_{rb}}\right)^{2/3}. \qquad [5.7]$$

This equation was found to give an accurate prediction of the energy loss in the coatings for energies above about 3 keV, depending on coating material and thickness. An improved energy loss equation will be presented below to provide a better fit for lower beam energies.

**Incident Angle Contributions and Coating Uniformity**

In order to accurately calculate the energy loss in the coating material, the path length of the electron is required. In this section, the fractional contribution to the luminescence from a given incidence angle will be calculated. This quantity will be referred to as the incident angle probability for the purposes of this study. Some of the equations derived in this calculation will be used to derive a more realistic representation of the coating thickness and account for its non-uniformity. The fractional contribution will then be recalculated based on the non-uniform coating.

As a first approximation, a uniform coating thickness will be assumed. It is also assumed that the particles are spherical, all incoming electrons are traveling from the top parallel to the mean surface normal of the particle, and the electron distribution is uniform in the mean plane of the surface. The assumption of spherical particles is an approximation to the shape of commercially processed phosphor powders. A phosphor grown from a sol-gel process also generally exhibits a spherical shape. This assumption of spherical particles also greatly reduces the complexity of the calculation. A uniform electron beam traveling along a trajectory parallel to the mean surface normal of the particles is valid for an electron gun located directly above the sample with low angular divergence. (If the electron gun were located in some other orientation with a low angular divergence, the treatment would be the same. However, knowledge of the location of the neighboring particles would be necessary to account for any small changes due to shadowing of the electrons by these particles.)

For this calculation, the center axis will be defined as the line that passes through the center of the sphere and is parallel to the mean surface normal vector. The first step in the calculation is to find the relationship between the angle θ from the center axis (which will also be the incident angle for a uniform coating) and the radius r from the center axis of the particle. Figure 5-1 shows a cross-sectional view of the spherical particle. From the figure, it can be seen that:

$$\sin(\theta) = \frac{r}{r_0 + t} \qquad [5.8]$$

or

$$\theta = \sin^{-1}\left(\frac{r}{r_0 + t}\right)$$

where t is the thickness of the coating. The derivative of Equation 5.8 will be needed later in the calculation, so it is presented here:

$$r = (r_0 + t)\sin(\theta)$$

$$dr = (r_0 + t)d[\sin(\theta)] = (r_0 + t)\cos(\theta)d\theta . \qquad [5.9]$$

Next, an incremental area of the incoming electron beam is calculated. The electrons are assumed to be uniform in the plane above the sphere. The particle's projection onto this plane will be a disk with a radius r, where r is the same as used above. Figure 5-2 shows a representation of this disk with an arbitrary incremental area depicted. This incremental area can be found by multiplying its two sides to give:

$$dA_{disk} = r(dr)(d\phi) . \qquad [5.10]$$

Taking the integral over dϕ gives:

$$dA_{disk} = 2\pi r(dr) .$$

Plugging in Equations 5.8 and 5.9 allow this incremental area to be related back to the incident angle on the spherical particle:

$$dA_{disk} = 2\pi(r_0 + t)^2 \sin(\theta)\cos(\theta)d\theta . \qquad [5.11]$$

Dividing Equation 5.11 by dθ will give the incremental area for any given θ. To find the probability of an electron striking the particle at this angle, the equation must also be divided by the area of the sphere. However, since the electrons can only strike the top half of the particle, only the top half need be considered when finding the surface area:

$$A_{hemisphere} = 2\pi(r_0 + t)^2 . \qquad [5.12]$$

Dividing Equation 5.11 by dθ and Equation 5.12 gives the probability P(θ) for any given incident angle θ as:

$$P(\theta) = \frac{dA_{disk}}{A_{hemisphere} d\theta} = \sin(\theta)\cos(\theta). \qquad [5.13]$$

The above equation can also be derived by relating an incremental area on the sphere to the incident electron flux. For this method, the first step is to find the incremental area on the sphere. Figure 5-3 depicts this area. The equation is obtained by multiplying the two sides that bound the box:

$$dA_{sphere} = (r d\phi)[(r_0 + t) d\theta] = (r_0 + t)^2 \sin(\theta) d\theta d\phi. \qquad [5.14]$$

Again, taking the integral over dϕ gives 2π. Combining this with Equation 5.12 and dividing by dθ results in the following equation:

$$\frac{dA_{sphere}}{A_{hemisphere} d\theta} = \sin(\theta). \qquad [5.15]$$

This may seem contradictory to the probability found earlier, but the direction of the incident electrons still needs to be considered. Thus far, spherical symmetry has been assumed. If this were the case, the electrons would have to be incident along the surface normal for any point on the sphere, meaning that the electrons would have to be uniformly distributed over the surface of the sphere and all traveling toward the center. For the model, it is assumed that all electrons are traveling in one direction, parallel to the mean surface normal of the particle. To account for this, a relation must be found between an incremental area of the incoming electrons and the corresponding area on the sphere. As in the previous calculation, the incremental area of the electrons is equivalent to that on a disk and is given by Equation 5.10. Similarly, the incremental area on the sphere is represented by Equation 5.14. Combining these equations yields:

$$\frac{dA_{disk}}{dA_{sphere}} = \frac{r(dr)(d\phi)}{r(r_0 + t)(d\theta)(d\phi)} = \frac{dr}{(r_0 + t)d\theta}.$$

Plugging in Equation 5.9 gives:

$$\frac{dA_{disk}}{dA_{sphere}} = \cos(\theta). \qquad [5.16]$$

This is the incremental area on the particle that corresponds to the same incremental area of incident electrons. Multiplying Equations 5.15 and 5.16 gives the correct equation for the probability:

$$P(\theta) = \frac{dA_{sphere}}{A_{hemisphere}d\theta}\left(\frac{dA_{disk}}{dA_{sphere}}\right) = \frac{dA_{disk}}{A_{hemisphere}d\theta} = \sin(\theta)\cos(\theta).$$

Therefore, both methods yield similar results for the probability, as can be see by comparing the above equation with Equation 5.13. (The second method was included because some of the equations derived from it will be used to calculate a more accurate representation of the coating thickness.) A plot of $P(\theta)$ versus $\theta$ is shown in Figure 5-4. The curve exhibits a maximum at 45° of 0.5. This shows that the majority of the luminescence from the particles with a uniform coating comes from electrons that are incident at 45° from surface normal. The fractional contribution goes towards zero as $\theta$ goes towards zero or 90. The large angle dependence is due to the curvature of the particle. The small angle dependence is a result of the diminishing area of interest as $\theta$ goes towards zero.

Until now, it was assumed that the coating layer was uniform in thickness over the surface of the powder particle. For an incident coating flux, uniform in the plane perpendicular to the mean surface normal and deposited onto a spherical particle surface,

the resultant coating will not be uniform. The spherical shape of the powder will lead to a thicker coating at the top of the particle and a thinner coating near the edges. This is similar to considerations given during calculation of the incident angle probability for the incoming electrons given above. From Equation 5.16, the ratio of an incremental area of the deposition flux to the same area on the spherical surface shows a cosine dependence. If the maximum thickness (at the top of the particle where $\theta = 0$) is defined as t, then the thickness of the coating, as measured radially from the center of the particle at any given angle $\theta$, will be given by t*cos($\theta$). See Figure 5-5 for a schematic.

A new incident angle probability will be calculated with the cosine dependent thickness. All other assumptions are the same as before. The relationship between $\theta$ (the angle from the center axis) and r (the distance from the central axis to the coating surface) is given by:

$$r = (r_0 + t\cos\theta)\sin\theta \qquad [5.21]$$

$$dr = \left[r_0 \cos\theta + t\left(\cos^2\theta - \sin^2\theta\right)\right]d\theta .$$

An incremental area of the coating flux can be found to be:

$$dA_{disk} = 2\pi(r)(dr) . \qquad [5.22]$$

The area of the top half of the sphere with the coating can be found by taking the integral of the incremental area on the sphere from zero to $\pi/2$. The result is:

$$A_{hemisphere} = 2\pi\left(r_0^2 + r_0 t + \tfrac{1}{3}t^2\right). \qquad [5.23]$$

Plugging in Equations 5.21, 5.22, and 5.23, the incident angle probability can be found to be:

$$P(\theta) = \frac{dA_{disk}}{A_{hemisphere} d\theta} \qquad [5.24]$$

or

$$P(\theta) = \frac{r_0^2 \sin\theta\cos\theta + 2r_0 t \sin\theta\cos^2\theta - r_0 t \sin^3\theta + t^2 \sin\theta\cos^3\theta - t^2 \sin^3\theta\cos\theta}{r_0^2 + r_0 t + \frac{1}{3}t^2}.$$

Figure 5-6 (derived in Appendix B) shows a plot of P(θ) versus θ for a variety of thicknesses. As can be seen from the graph, the maximum of this function moves to lower angles as the thickness is increased. This is a result of the θ dependence of the coating.

In the uniform coating model, θ was not only the angle from the center axis, but also the incidence angle from surface normal. This is no longer the case for the cosine dependent coating because surface normal does not point radially out from the coating. The curvature of the coating would have to be spherical for this to be the case. To find the angle to surface normal (ψ), the slope of the surface normal vector is needed. This is the negative reciprocal of the slope of the surface tangent. From Figure 5-5, it can be seen that the height of the coated particle can be expressed as:

$$h = (r_0 + t\cos\theta)\cos\theta. \qquad [5.25]$$

The slope of the tangent line can be expressed as:

$$\frac{dh}{dr} = \frac{dh}{d\theta} * \frac{d\theta}{dr}.$$

This can be found using Equation 5.21 and the derivative of Equation 5.25. The slope of the surface normal is the negative reciprocal of the tangent line because the lines are perpendicular. The slope of the surface normal therefore can be expressed as:

$$-\frac{dr}{dh} = \frac{r_0 \cos\theta + t\cos^2\theta - t\sin^2\theta}{r_0 \sin\theta + 2t\cos\theta\sin\theta}. \qquad [5.26]$$

The angle of the incident electron to the surface normal is the cotangent of the slope of the surface normal. By Equation 5.26, the angle is:

$$\Psi = \cot^{-1}\left(\frac{r_0 \cos\theta + t\cos^2\theta - t\sin^2\theta}{r_0 \sin\theta + 2t\cos\theta\sin\theta}\right). \qquad [5.27]$$

Figure 5-7 (derived in Appendix B) shows a plot of the relationship between $\psi$ and $\theta$. The incident angle probability versus the angle to surface normal is shown in Figure 5-8. It can be seen that all of the curves have a maximum around 45°, similar to the results from the uniform coating.

**Path Length of Electrons in the Coating**

To determine the energy loss in the coating, a measure of the path length of the electron in the coating is needed. A new angle ($\gamma$) must be defined to facilitate this computation. Figure 5-5 shows this schematically. The angle $\gamma$ will be defined as the angle from the center axis (defined as before) to the point on the spherical surface directly below the intersection of the radial line with the coating surface at angle $\theta$. The relationship between $\gamma$ and r can be expressed as:

$$r = r_0 \sin\gamma. \qquad [5.28]$$

Combining this with Equation 5.21 gives:

$$\gamma = \sin^{-1}\left(\frac{(r_0 + t\cos\theta)\sin\theta}{r_0}\right). \qquad [5.29]$$

The coating thickness parallel to the center axis is found by subtracting the height of the particle from the height of the particle and coating:

$$d = (r_0 + t\cos\theta)\cos\theta - r_0\cos\gamma .$$

Figure 5-9 (derived in Appendix C) shows the coating at various thicknesses. The undercutting at the edge of the particle is due to shadowing by the coating during deposition. Figure 5-10 (derived in Appendix C) shows the vertical coating thickness d as a function of angle for multiple thicknesses. Assuming no diffuse scattering of the electron as it passes through the coating, the distance d is the path length of the electron in the coating. One interesting aspect of the thickness d is that it is almost constant for all angles, except near the edge of the particle where the coating becomes nearly vertical. The nearly constant value of d implies that the electron travels the same distance in the coating irrespective of where it impinges on the surface. Thus, only one angle needs to be considered for calculation of the energy loss in the coating layer. It should also be pointed out that the thicker coatings in Figures 5-6 through 5-10 and Appendices B and C are very large compared to the coatings applied for this work. These large values were chosen to exaggerate and illustrate the effects, but they should not be considered an accurate portrayal of the coatings studied here.

**Calculation of the Cathodoluminescence from Coated Phosphors**

To calculate the cathodoluminescence from a coated phosphor, the energy loss in the coating needs to be determined. From the discussion above, the path length in the coating will be equal to the thickness at $\theta = 0$, regardless of where the electron strikes the particle. Given this path length, the next step is to determine the energy loss along this

trajectory. To start, the modified Bethe stopping power equation is used. Bethe's original equation is given in Equation 2.1 as:

$$\frac{dE}{ds} = \frac{-785\rho Z}{A * E} \ln\left(\frac{1.166E}{J}\right)$$

where A is the atomic weight in g/mol, Z is the atomic number, E is the electron energy, $\rho$ is the density in g/cm$^3$, and J is the mean ionization potential in eV.[14, 24, 27-30] Rao-Sahib and Wittry suggested a correction to the original equation to account for the inflection at low energies. Their new equation was a parabolic extrapolation of the stopping power from the inflection point at E = 6.338 J down to E = 0. The modified equation is given in Equation 2.3 as[30]:

$$\frac{dE}{ds} = \frac{-785 * \rho * Z}{1.2588 * A * \sqrt{E * J}}.$$

The low energy correction by Joy and Luo of the mean ionization potential is also used; it is given in Equation 2.4 as[14, 29, 31]:

$$J' = \frac{J}{1 + k\left(\frac{J}{E}\right)}$$

where J' is the new mean ionization potential, J is the average energy loss per interaction, and k is a fitting parameter around 0.85. Appendix D shows a plot of the various stopping power equations. The stopping power suggested by Love et al. is also shown for comparison.[131] The stopping power equation of Rao-Sahib and Wittry was chosen for calculating the energy loss in the coating because it had the correct form and is widely accepted as being more accurate. Equation 5.7 is the integrated stopping power equation. This is the same equation used in the energy loss calculations.

The integrated stopping power equation requires knowledge of the incident energy of the electrons, range in the coating, and the total path length of an electron in a bulk sample of the coating material. As a first attempt, Monte Carlo simulations were used to find the total path length in bulk, $z_{rb}$.[132, 133] These simulations provided a convenient method of finding the ranges at a few selected energies, but they were not realistic for determining the ranges over the entire energy interval of interest. To calculate the path length at any given incident energy, the stopping power equation was integrated and the total range defined as the point where the energy of the electron went to zero. Thus the total range can be expressed as:

$$z_{rb} = \frac{252 * A * J^{\frac{1}{2}} * E_0^{\frac{3}{2}}}{2355 * \rho * Z} \qquad [5.30]$$

where the energy values are expressed in keV and the range is in microns. The mean ionization potential J given by Equation 2.2 is valid for $Z \geq 13$; since both of the coatings used in this work had an average Z = 10, the following equation was chosen instead:

$$J = 11.5 * Z \qquad [5.31]$$

where J is measured in eV. This equation is valid for $Z \leq 12$.[29]

The luminescence versus beam energy curves for the uncoated and coated phosphors shown in Figures 4-19, 4-21, 4-23, 4-25, 4-27, 4-29, 4-31, 4-33, and 4-35 were converted to a linear intensity versus energy scale to be more consistent with results displayed in the literature. These are shown in Figures 5-11 through 5-19. These luminescence curves were chosen because the main emission peak of the phosphor will dominate emission from the sample. The curves have been fit using a power law equation of the form:

$$L = a0 + a1 * E^{a2}$$

where a0, a1, and a2 are the fit parameters; they are displayed on the graphs.

Using all of the above parameters, the energy loss, based on the Rao-Sahib and Wittry stopping power equation, is calculated as the electron passes through the coating. The energy of the electron as it passes from the coating into the phosphor is then used to find the luminescence by plugging this new lower energy into the fit equation for the uncoated phosphor's luminescence. The Mathcad programs used to calculate the luminescence are presented in Appendices E through M. The calculated luminescence versus beam energy curves are shown in Figures 5-20 through 5-28, along with the measured luminescence from Figures 5-11 through 5-19.

**New Energy Loss Equation**

Examination of the calculated luminescence in Figures 5-20 through 5-28 shows that the Rao-Sahib and Wittry equation does not give an accurate fit to the measured curves at low energy. A second energy equation was used to improve the accuracy of the fit. Many authors have shown that the Bethe stopping power equation overestimates the energy loss at low electron energies. To correct for this, they used a cutoff energy in the interval and added a residual range to the calculated result.[28, 29] Joy, based on results by Nieminen, further suggested that the stopping power for all materials varies as $E^{5/2}$ below about 50 eV.[29] Other authors have used the power loss function derived by Makhov that says that the electron beam power per unit area at a depth x is given by the following:

$$P(x, j_0, V_0) = j_0 V_0 \exp\left(-X^2 - X^{0.9}\right) \qquad [5.32]$$

where $j_0$ is the beam current density at the surface, $V_0$ is the accelerating potential, and X is the normalized depth given by:

$$X(x,V_0) = \frac{x}{\rho^{-1} * C * V_0^n} = \frac{x}{R(V_0)}$$

where ρ is the density of the material and C and n are fitting parameters that are material dependent. $R(V_0)$ is referred to as the electron range and is equal to the point when $P = j_0 V_0 \exp(-2)$.[96, 134] Kingsley and Prener also suggested a simple exponential excitation function:

$$P(x, j_0, V_0) = j_0 V_0 \exp\left(\frac{-2x}{R}\right) \qquad [5.33]$$

that fit their data just as well as the Makhov function. This equation has a form similar to Equation 5.32, with equal exponents. It is also similar to an equation given by Dowling and Sewell.[96]

To provide a better fit to the measured luminescence from the coated phosphors, Equation 5.33 was used. Dividing by the current gives the energy of an electron after traveling a distance x through the coating. The resulting equation is:

$$E = E_0 \exp\left(\frac{-2x}{a' * E_0^{k'}}\right) \qquad [5.34]$$

where a′ and k′ are fitting parameters for the material of interest. One of the biggest potential sources of error in implementing the new model involved finding an accurate measurement of the coating thickness. To obtain an accurate value, the thickness used for the model was adjusted slightly so that the attenuation predicted by the Bethe stopping power equation matched the measured luminescence from the coated sample in the higher energy region (around 4 keV). This method was chosen because the Bethe

stopping power equation has been shown by many authors to be an accurate prediction of energy loss at energies of ~ 4 keV. The fitting parameters in Equation 5.34 were then found so that the energy loss would match the Bethe equation at higher energies while still accurately predicting the luminescence from the coated sample at low energies. Once the constants a′ and k′ were found for one coating thickness, the energy loss equation (5.34) could then be used to accurately predict the luminescent attenuation for all of the other coating thicknesses for the same coating material. Plots of the energy of the electron as it exits the coating that were made using the Bethe equation and Equation 5.34 are shown in Figures 5-29 through 5-37 for each of the coatings used for this study. The Mathcad programs used to derive these figures are presented in Appendices E through M. The calculated and measured luminescence from the coated sample is shown in Figures 5-20 through 5-28. Their derivation is also shown in Appendices E through M. Comparison of the calculated attenuation in the luminescence to the measured luminescence shows that this method allows for accurate prediction of the luminescence from a coated particle.

**Backscattering Coefficients**

When a coating is placed on top of a phosphor, it will change the number of electrons backscattered from the material. The coating material and its thickness could play an important role in determining the backscattering coefficient for a given beam energy. To study the effects on the backscattering coefficient, Windows-based Monte Carlo simulation codes were used.[132, 133] Required parameters for the simulations included average atomic number, average atomic weight, and density for each of the

materials. Table 6 gives a list of these. The simulations provided an output of the backscattering coefficient for the current run directly on the plot. To find this number, the program keeps track of the number of electrons lost from the top surface of the material. It then compares this against the total number of incident electrons to calculate the percentage backscattered. Multiple runs of 100,000 trajectories were done to ensure sufficient averaging. Proceeding in such a manner, simulations were done for uncoated $Y_2O_3$:Eu and coatings of MgO and $Al_2O_3$ on $Y_2O_3$:Eu . For each of these, simulations had to be completed for multiple beam energies at various coating thicknesses. Table 7 is a compilation of all of the calculated backscattering coefficients. No simulations were performed for the $Y_2SiO_5$:Tb samples because the thickness was so large that the simulations predicted that only a small fraction, if any, of the incident electrons would reach the phosphor material. This is due to the overprediction of the stopping power based on the Bethe equation, as discussed above.

Incorporation of a correction into the luminescence model would require an assumption that the difference in backscattering coefficient is due to electrons that remained in the phosphor material as a result of the coating. Although the coating could have contributed to a small change in the number of electrons lost from the phosphor, it is not feasible to assume that the numbers calculated with the Monte Carlo simulations are an accurate measure of these. Due to the agreement of the calculated cathodoluminescence with the experimental data, no correction was used to account for a change in the backscattering due to the presence of a coating layer.

**Index of Refraction**

If there were a large difference in the index of refraction between the film and phosphor, then critical angle issues would have to be considered for a smooth surface. When electromagnetic radiation passes from one medium to another, its direction is changed. Snell's Law describes this change[135]:

$$n_1 \sin(\theta_1) = n_2 \sin(\theta_2)$$

where n is the index of refraction and θ is the angle from surface normal. If the light travels from a medium with a higher index to one with a lower index, then there is an angle, $\theta_c$, at which all of the light will be internally reflected. This is called the critical angle and is given by the following[70]:

$$\theta_c = \sin^{-1}\left(n_2 / n_1\right)$$

where $n_1$ and $n_2$ are the higher and lower index of refraction, respectively. Since the phosphor's index is larger than the air around it, the light generated in the phosphor will exhibit a critical angle dependence. Applying a coating to the surface of the phosphor can affect the light rays and change this angular dependence. Table 8 shows the index of refraction for the coatings and phosphors at the wavelength of interest for the light produced by the phosphors. It can be seen from the table that the indices of the coatings and phosphors are similar. Thus, there will be little effect on the light traveling from the particle into the coating. Also, the critical angle of the light leaving the coating will be nearly the same as for the uncoated powder. For these reasons, no corrections were made in the model to account for a difference in the index of refraction.

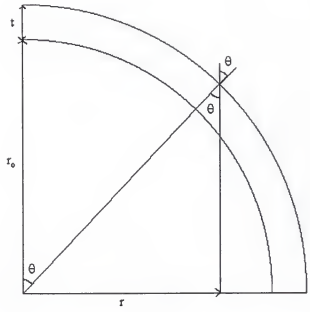


Figure 5-1 Cross-sectional schematic of spherical phosphor with a uniform coating layer of thickness t. The angle from the center axis, θ, will be equal to the incident electron angle from surface normal because of the uniform coating.

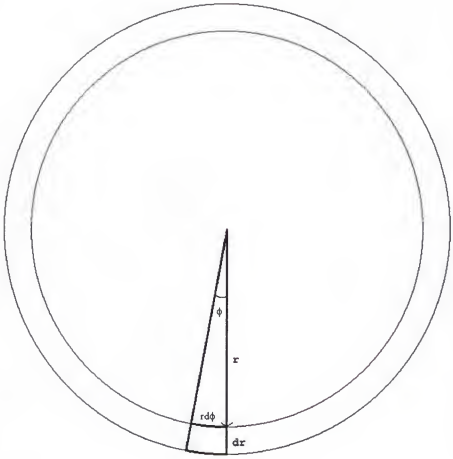


Figure 5-2 Schematic of incremental area of the incident electrons. This also represents the planar projection of the spherical particle as seen by the incoming electrons.

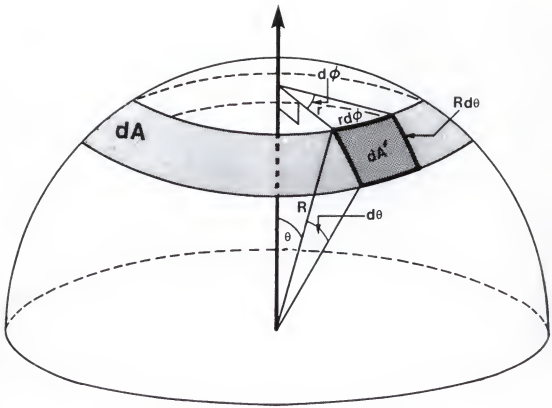


Figure 5-3 Schematic of the phosphor surface with an incremental area depicted.[136]

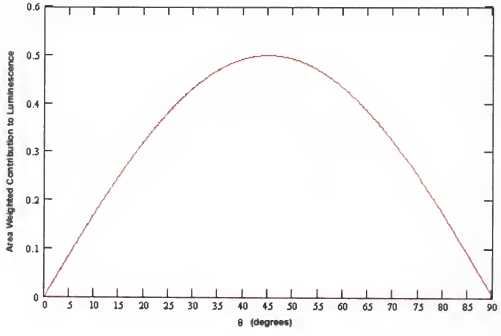


Figure 5-4 Area weighted contribution to the luminescence versus the angle from the center axis of the particle for a uniform coating. The center axis has been defined as the line passing through the center of the particle parallel to the mean surface normal.

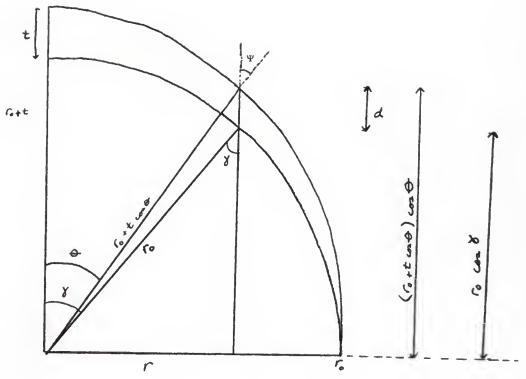


Figure 5-5 Schematic of phosphor particle with a non-uniform coating that varies in thickness as t*cos(θ), where θ is the angle from the center axis. All other variables are defined in the text.

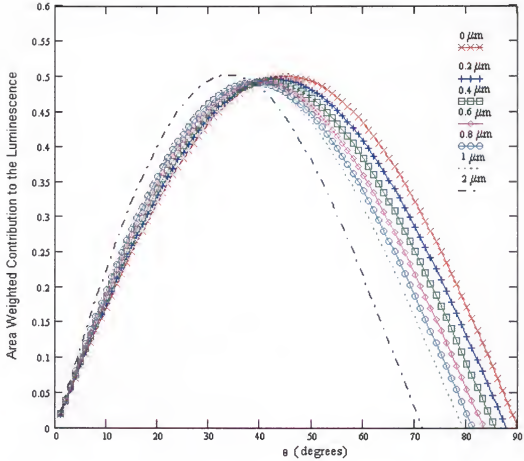


Figure 5-6 Area weighted contribution to the luminescence as a function of the angle from the mean surface normal for a cosine-dependent coating thickness. The thickness values shown are for $\theta = 0$.

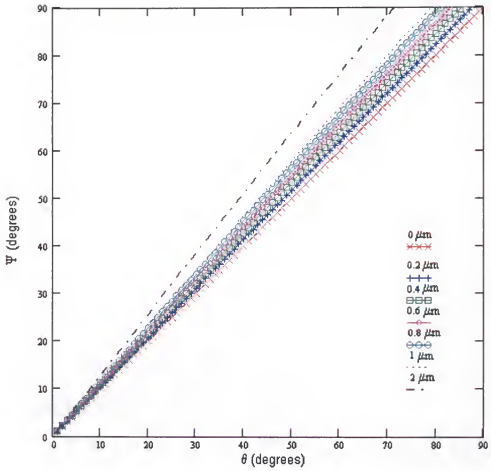


Figure 5-7 The angle from surface normal versus the angle from the mean surface normal for a cosine-dependent coating thickness. The thickness values shown are for $\theta = 0$.

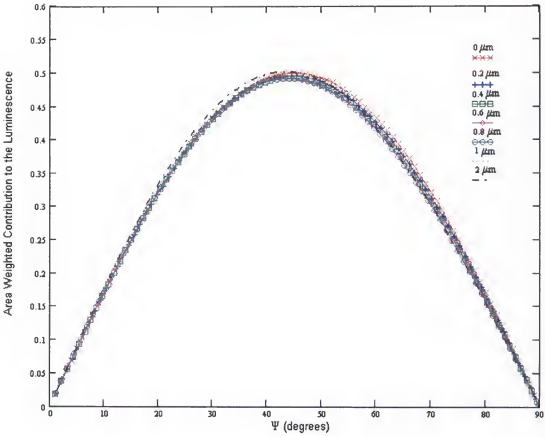


Figure 5-8 Area weighted contribution to the luminescence as a function of the angle of incidence from surface normal for a cosine-dependent coating thickness. The thickness values shown are for $\theta = 0$.

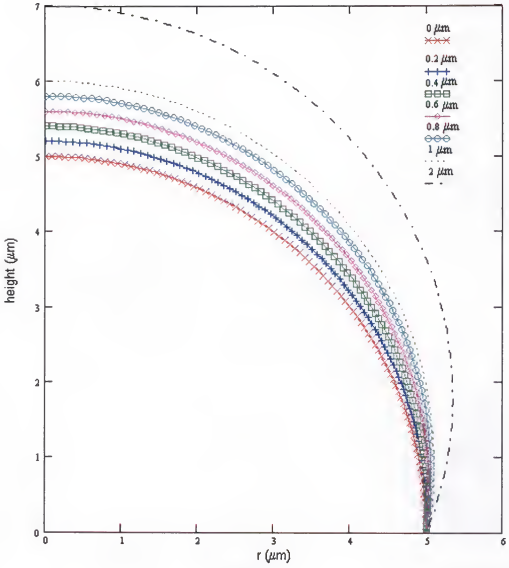


Figure 5-9 The height of the coating as a function of the distance from the center axis for a uniform coating flux deposited onto a spherical particle. The center axis has been defined as the line passing through the center of the particle parallel to the mean surface normal. The undercutting of the coating is due to shadowing during the deposition process. The thickness values shown are the maximum thickness of the coating, which will be located at the top of the particle.

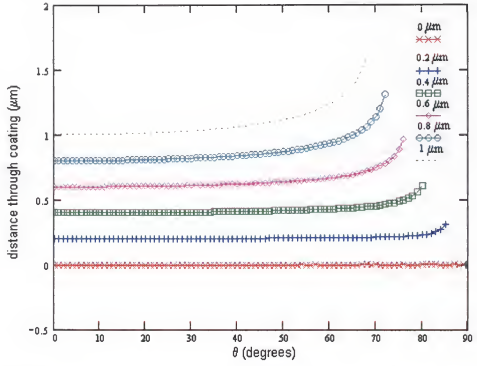


Figure 5-10 The vertical distance through the coating as a function of the angle from the mean surface normal for a cosine-dependent coating thickness. The thickness values shown are for $\theta = 0$.

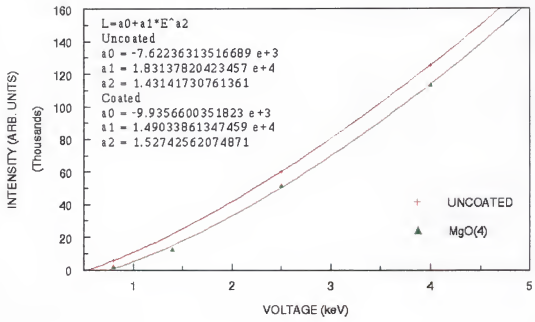


Figure 5-11 The cathodoluminescence intensity of the 611 nm peak as a function of beam energy for a coating of MgO deposited for 4 minutes on $Y_2O_3$:Eu powder. Both coated and uncoated results are shown. The beam current was kept constant at 0.16 $\mu A/cm^2$, while the accelerating voltage was varied from 0.8 to 4 keV. The data were fitted to a power law equation, with the fit parameters shown on the graph.

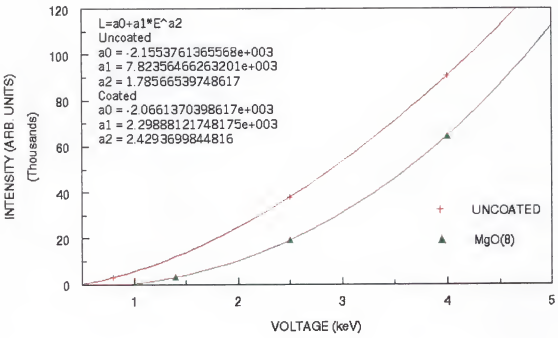


Figure 5-12 The cathodoluminescence intensity of the 611 nm peak as a function of beam energy for a coating of MgO deposited for 8 minutes on $Y_2O_3$:Eu powder. Both coated and uncoated results are shown. The beam current was kept constant at 0.16 $\mu A/cm^2$, while the accelerating voltage was varied from 0.8 to 4 keV. The data were fitted to a power law equation, with the fit parameters shown on the graph.

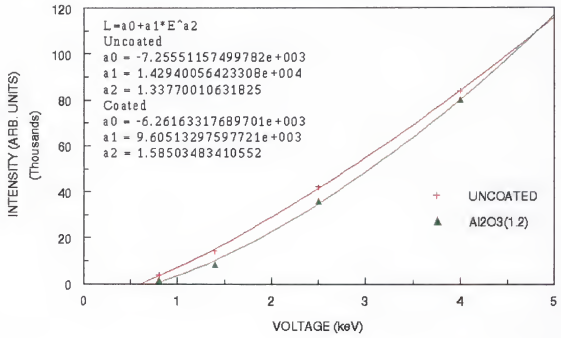


Figure 5-13 The cathodoluminescence intensity of the 611 nm peak as a function of beam energy for a coating of $Al_2O_3$ deposited for 1.2 minutes on $Y_2O_3$:Eu powder. Both coated and uncoated results are shown. The beam current was kept constant at 0.16 $\mu A/cm^2$, while the accelerating voltage was varied from 0.8 to 4 keV. The data were fitted to a power law equation, with the fit parameters shown on the graph.

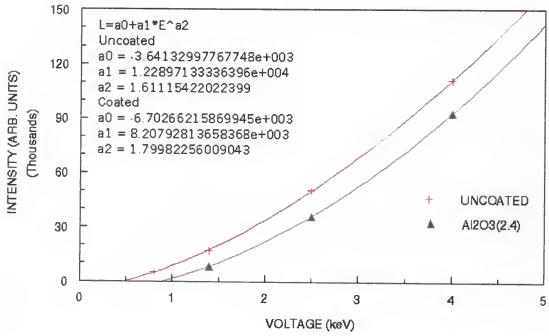


Figure 5-14 The cathodoluminescence intensity of the 611 nm peak as a function of beam energy for a coating of $Al_2O_3$ deposited for 2.4 minutes on $Y_2O_3$:Eu powder. Both coated and uncoated results are shown. The beam current was kept constant at 0.16 $\mu A/cm^2$, while the accelerating voltage was varied from 0.8 to 4 keV. The data were fitted to a power law equation, with the fit parameters shown on the graph.

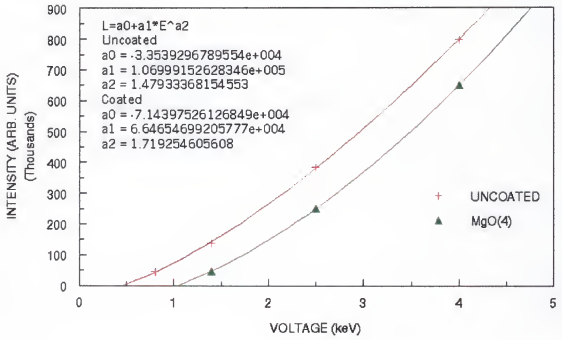


Figure 5-15 The cathodoluminescence intensity of the 547 nm peak as a function of beam energy for a coating of MgO deposited for 4 minutes on $Y_2SiO_5$:Tb powder. Both coated and uncoated results are shown. The beam current was kept constant at 0.16 $\mu A/cm^2$, while the accelerating voltage was varied from 0.8 to 4 keV. The data were fitted to a power law equation, with the fit parameters shown on the graph.

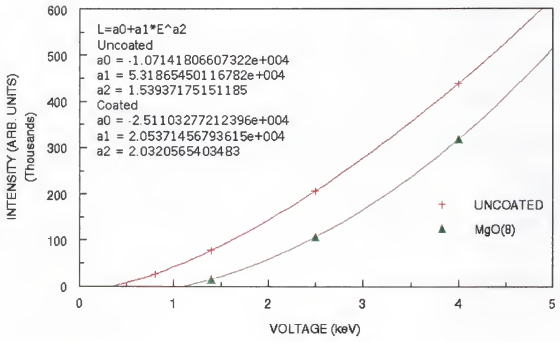


Figure 5-16 The cathodoluminescence intensity of the 547 nm peak as a function of beam energy for a coating of MgO deposited for 8 minutes on $Y_2SiO_5$:Tb powder. Both coated and uncoated results are shown. The beam current was kept constant at 0.16 $\mu A/cm^2$, while the accelerating voltage was varied from 0.8 to 4 keV. The data were fitted to a power law equation, with the fit parameters shown on the graph.

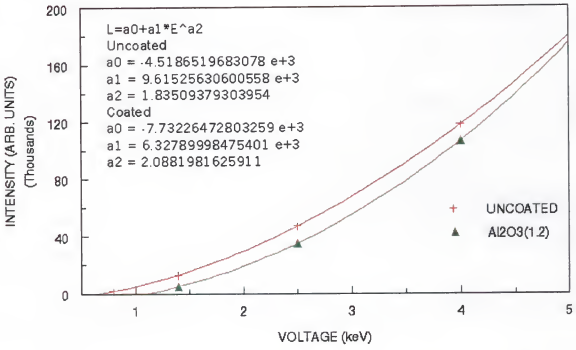


Figure 5-17 The cathodoluminescence intensity of the 547 nm peak as a function of beam energy for a coating of $Al_2O_3$ deposited for 1.2 minutes on $Y_2SiO_5$:Tb powder. Both coated and uncoated results are shown. The beam current was kept constant at 0.16 $\mu A/cm^2$, while the accelerating voltage was varied from 0.8 to 4 keV. The data were fitted to a power law equation, with the fit parameters shown on the graph.

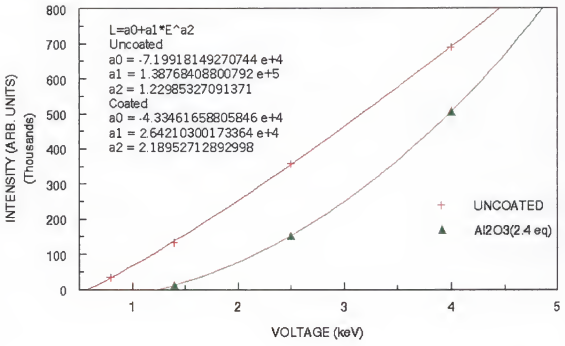


Figure 5-18 The cathodoluminescence intensity of the 547 nm peak as a function of beam energy for a coating of $Al_2O_3$ deposited for 5 minutes on $Y_2SiO_5$:Tb powder in new chamber. Both coated and uncoated results are shown. The beam current was kept constant at 0.16 $\mu A/cm^2$, while the accelerating voltage was varied from 0.8 to 4 keV. The data were fitted to a power law equation, with the fit parameters shown on the graph.

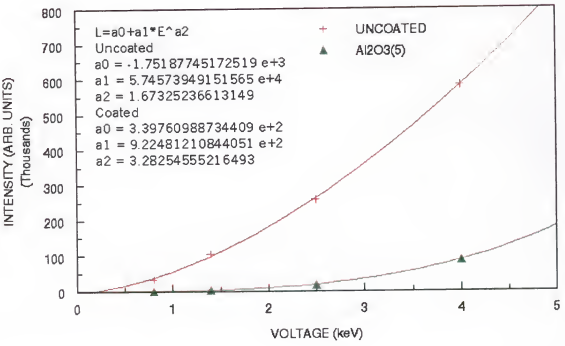


Figure 5-19 The cathodoluminescence intensity of the 547 nm peak as a function of beam energy for a coating of $Al_2O_3$ deposited for 5 minutes on $Y_2SiO_5$:Tb powder. Both coated and uncoated results are shown. The beam current was kept constant at 0.16 $\mu A/cm^2$, while the accelerating voltage was varied from 0.8 to 4 keV. The data were fitted to a power law equation, with the fit parameters shown on the graph.

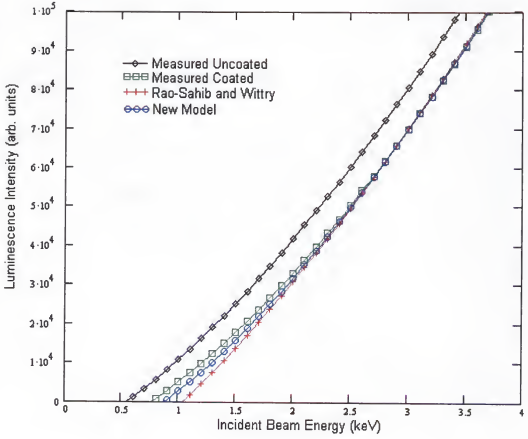


Figure 5-20 Luminescence intensity as a function of beam voltage for a 4 minute coating of MgO on $Y_2O_3$:Eu powder. Curves are shown for the measured cathodoluminescence from both the coated and uncoated phosphor. Calculated cathodoluminescence intensity from the coated sample using both the Rao-Sahib and Wittry stopping power equation and the new energy loss equation are also shown. From the graph, it can be seen that the new energy loss equation allows for an improved calculation of the cathodoluminescence at low energies. Markers on the curves are for curve differentiation only and do not represent actual measured values.

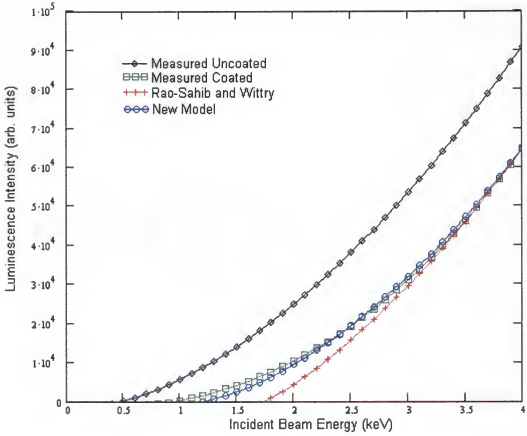


Figure 5-21 Luminescence intensity as a function of beam voltage for a 8 minute coating of MgO on $Y_2O_3$:Eu powder. Curves are shown for the measured cathodoluminescence from both the coated and uncoated phosphor. Calculated cathodoluminescence intensity from the coated sample using both the Rao-Sahib and Wittry stopping power equation and the new energy loss equation are also shown. From the graph, it can be seen that the new energy loss equation allows for an improved calculation of the cathodoluminescence at low energies. Markers on the curves are for curve differentiation only and do not represent actual measured values.

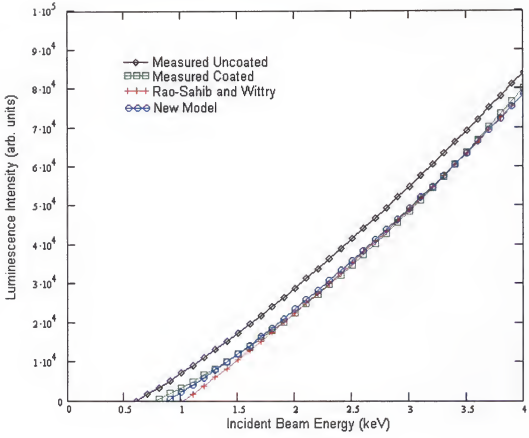


Figure 5-22 Luminescence intensity as a function of beam voltage for a 1.2 minute coating of $Al_2O_3$ on $Y_2O_3$:Eu powder. Curves are shown for the measured cathodoluminescence from both the coated and uncoated phosphor. Calculated cathodoluminescence intensity from the coated sample using both the Rao-Sahib and Wittry stopping power equation and the new energy loss equation are also shown. From the graph, it can be seen that the new energy loss equation allows for an improved calculation of the cathodoluminescence at low energies. Markers on the curves are for curve differentiation only and do not represent actual measured values.

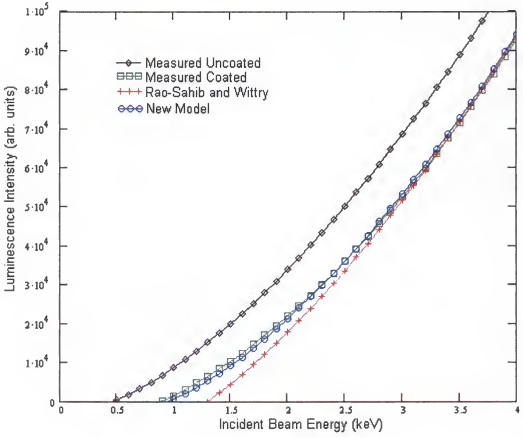


Figure 5-23 Luminescence intensity as a function of beam voltage for a 2.4 minute coating of $Al_2O_3$ on $Y_2O_3$:Eu powder. Curves are shown for the measured cathodoluminescence from both the coated and uncoated phosphor. Calculated cathodoluminescence intensity from the coated sample using both the Rao-Sahib and Wittry stopping power equation and the new energy loss equation are also shown. From the graph, it can be seen that the new energy loss equation allows for an improved calculation of the cathodoluminescence at low energies. Markers on the curves are for curve differentiation only and do not represent actual measured values.

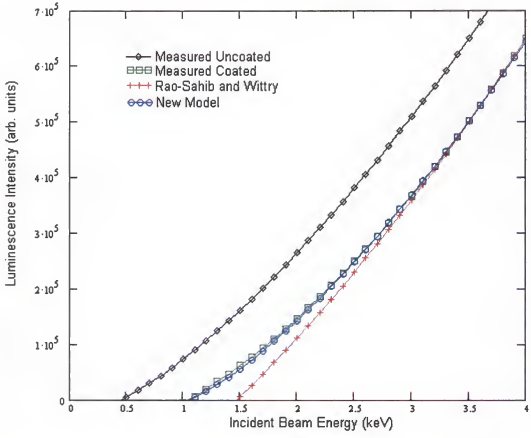


Figure 5-24 Luminescence intensity as a function of beam voltage for a 4 minute coating of MgO on $Y_2SiO_5$:Tb powder. Curves are shown for the measured cathodoluminescence from both the coated and uncoated phosphor. Calculated cathodoluminescence intensity from the coated sample using both the Rao-Sahib and Wittry stopping power equation and the new energy loss equation are also shown. From the graph, it can be seen that the new energy loss equation allows for an improved calculation of the cathodoluminescence at low energies. Markers on the curves are for curve differentiation only and do not represent actual measured values.

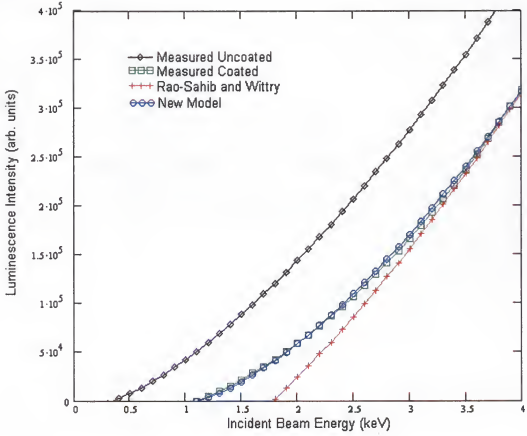


Figure 5-25 Luminescence intensity as a function of beam voltage for a 8 minute coating of MgO on $Y_2SiO_5$:Tb powder. Curves are shown for the measured cathodoluminescence from both the coated and uncoated phosphor. Calculated cathodoluminescence intensity from the coated sample using both the Rao-Sahib and Wittry stopping power equation and the new energy loss equation are also shown. From the graph, it can be seen that the new energy loss equation allows for an improved calculation of the cathodoluminescence at low energies. Markers on the curves are for curve differentiation only and do not represent actual measured values.

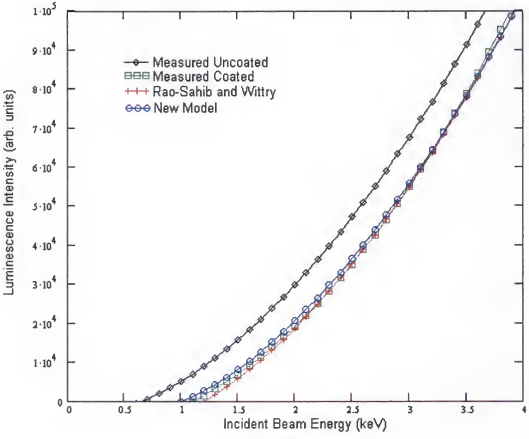


Figure 5-26 Luminescence intensity as a function of beam voltage for a 1.2 minute coating of $Al_2O_3$ on $Y_2SiO_5$:Tb powder. Curves are shown for the measured cathodoluminescence from both the coated and uncoated phosphor. Calculated cathodoluminescence intensity from the coated sample using both the Rao-Sahib and Wittry stopping power equation and the new energy loss equation are also shown. From the graph, it can be seen that the new energy loss equation allows for an improved calculation of the cathodoluminescence at low energies. Markers on the curves are for curve differentiation only and do not represent actual measured values.

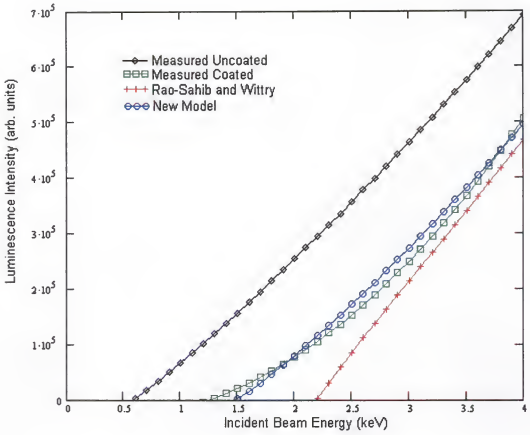


Figure 5-27 Luminescence intensity as a function of beam voltage for a 5 minute coating in the new chamber of $Al_2O_3$ on $Y_2SiO_5$:Tb powder. Curves are shown for the measured cathodoluminescence from both the coated and uncoated phosphor. Calculated cathodoluminescence intensity from the coated sample using both the Rao-Sahib and Wittry stopping power equation and the new energy loss equation are also shown. From the graph, it can be seen that the new energy loss equation allows for an improved calculation of the cathodoluminescence at low energies. The poor agreement between the calculated and measured luminescence is due to the fitting equation found for the measured luminescence. Markers on the curves are for curve differentiation only and do not represent actual measured values.

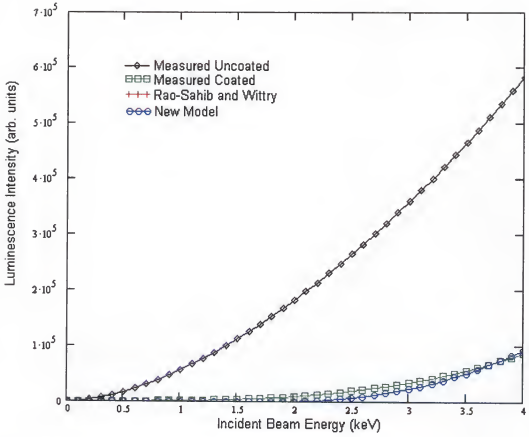


Figure 5-28 Luminescence intensity as a function of beam voltage for a 5 minute coating of $Al_2O_3$ on $Y_2SiO_5$:Tb powder. Curves are shown for the measured cathodoluminescence from both the coated and uncoated phosphor. Calculated cathodoluminescence intensity from the coated sample using the new energy loss equation is also shown. No luminescence is predicted over this energy range using the Rao-Sahib and Wittry energy loss calculation. Markers on the curves are for curve differentiation only and do not represent actual measured values.

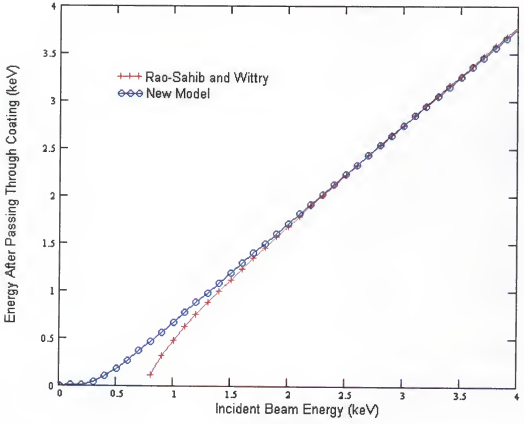


Figure 5-29 Energy of the electron after passing through coating layer as a function of incident beam energy for a 4 minute coating of MgO on $Y_2O_3$:Eu. Shown are the energies based on the Rao-Sahib and Wittry stopping power equation and the new energy loss equation. The fitting parameters in the new energy loss equation were chosen so that the energy loss would match that from the Rao-Sahib and Wittry equation at high energies (above about 3 keV), while allowing for a better fit to the measured luminescence at low energies.

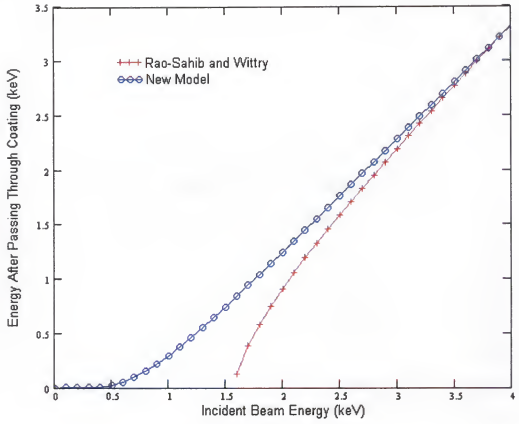


Figure 5-30 Energy of the electron after passing through coating layer as a function of incident beam energy for a 8 minute coating of MgO on $Y_2O_3$:Eu. Shown are the energies based on the Rao-Sahib and Wittry stopping power equation and the new energy loss equation. The fitting parameters in the new energy loss equation were chosen so that the energy loss would match that from the Rao-Sahib and Wittry equation at high energies (above about 3.5 keV), while allowing for a better fit to the measured luminescence at low energies.

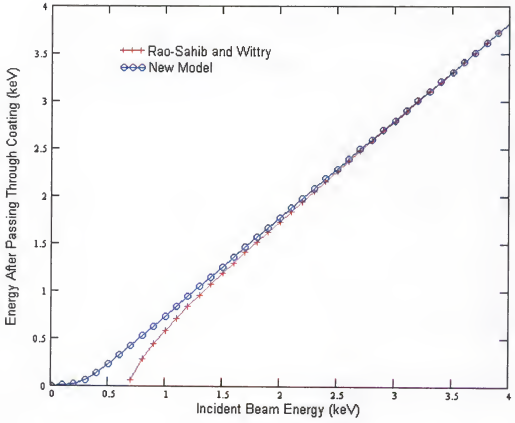


Figure 5-31 Energy of the electron after passing through coating layer as a function of incident beam energy for a 1.2 minute coating of $Al_2O_3$ on $Y_2O_3$:Eu. Shown are the energies based on the Rao-Sahib and Wittry stopping power equation and the new energy loss equation. The fitting parameters in the new energy loss equation were chosen so that the energy loss would match that from the Rao-Sahib and Wittry equation at high energies (above about 3 keV), while allowing for a better fit to the measured luminescence at low energies.

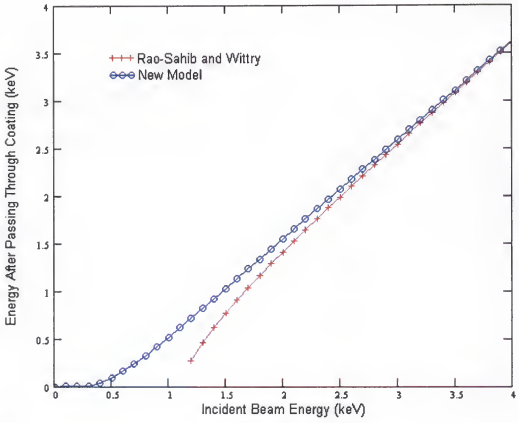


Figure 5-32 Energy of the electron after passing through coating layer as a function of incident beam energy for a 2.4 minute coating of $Al_2O_3$ on $Y_2O_3$:Eu. Shown are the energies based on the Rao-Sahib and Wittry stopping power equation and the new energy loss equation. The fitting parameters in the new energy loss equation were chosen so that the energy loss would match that from the Rao-Sahib and Wittry equation at high energies (above about 3 keV), while allowing for a better fit to the measured luminescence at low energies.

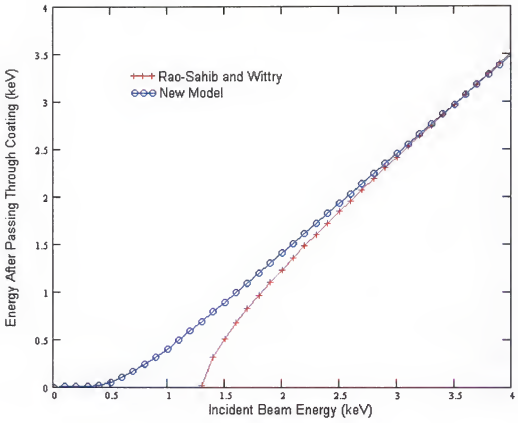


Figure 5-33 Energy of the electron after passing through coating layer as a function of incident beam energy for a 4 minute coating of MgO on $Y_2SiO_5$:Tb. Shown are the energies based on the Rao-Sahib and Wittry stopping power equation and the new energy loss equation. The fitting parameters in the new energy loss equation were chosen so that the energy loss would match that from the Rao-Sahib and Wittry equation at high energies (above about 3 keV), while allowing for a better fit to the measured luminescence at low energies.

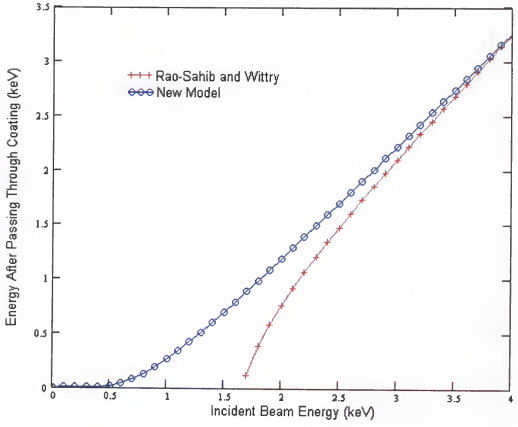


Figure 5-34 Energy of the electron after passing through coating layer as a function of incident beam energy for a 8 minute coating of MgO on $Y_2SiO_5$:Tb. Shown are the energies based on the Rao-Sahib and Wittry stopping power equation and the new energy loss equation. The fitting parameters in the new energy loss equation were chosen so that the energy loss would match that from the Rao-Sahib and Wittry equation at high energies (above about 3.5 keV), while allowing for a better fit to the measured luminescence at low energies.

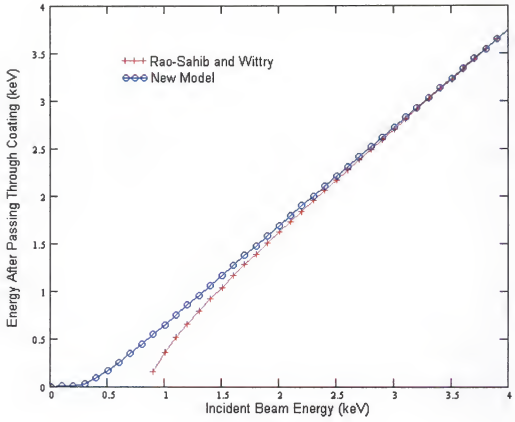


Figure 5-35 Energy of the electron after passing through coating layer as a function of incident beam energy for a 1.2 minute coating of $Al_2O_3$ on $Y_2SiO_5$:Tb. Shown are the energies based on the Rao-Sahib and Wittry stopping power equation and the new energy loss equation. The fitting parameters in the new energy loss equation were chosen so that the energy loss would match that from the Rao-Sahib and Wittry equation at high energies (above about 3 keV), while allowing for a better fit to the measured luminescence at low energies.

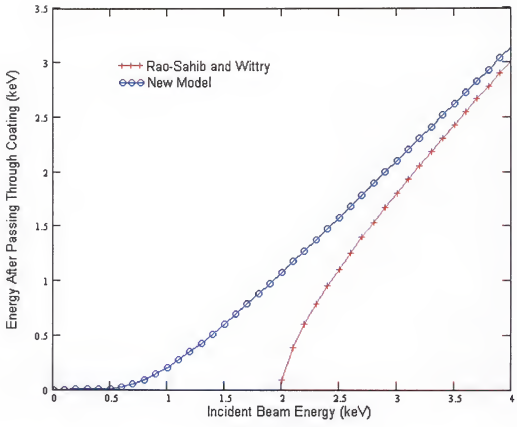


Figure 5-36 Energy of the electron after passing through coating layer as a function of incident beam energy for a 5 minute coating in the new chamber of $Al_2O_3$ on $Y_2SiO_5$:Tb. Shown are the energies based on the Rao-Sahib and Wittry stopping power equation and the new energy loss equation.

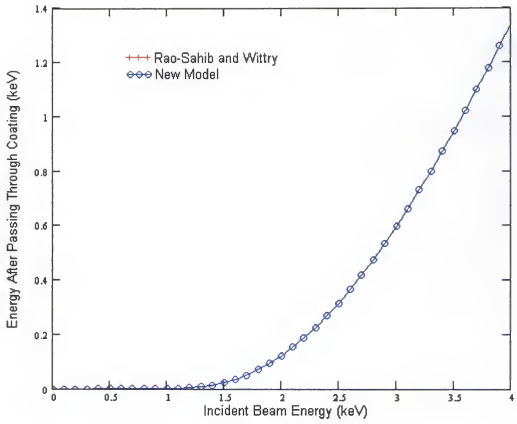


Figure 5-37 Energy of the electron after passing through coating layer as a function of incident beam energy for a 5 minute coating of $Al_2O_3$ on $Y_2SiO_5$:Tb. Shown are the energies based on the Rao-Sahib and Wittry stopping power equation and the new energy loss equation. The Rao-Sahib and Wittry stopping power predicts that no electrons will penetrate this coating over the energy range from 0 to 4 keV.

Table 6

Average atomic number, density, and average atomic weight of the different materials used in this work.

| Material | Average Atomic Number (Z) | Density $g/cm^3$ | Average Atomic Weight |
|---|---|---|---|
| $Al_2O_3$ | 10 | 3.97 | 20.3922 |
| MgO | 10 | 3.6 | 20.152 |
| Si | 14 | 2.3290 | 28.086 |
| $Y_2O_3$ | 20.4 | 5.03 | 45.162 |
| $Y_2SiO_5$ | 16.5 | 4.43 | 35.7368 |
| C (graphite) | 6 | 2.5 | 12.011 |

Atomic number and atomic weight numbers tabulated from periodic table. Density values for all elements except $Y_2SiO_5$ taken from CRC Handbook. Density value for $Y_2SiO_5$ taken from reference 51.

Table 7

Backscattering coefficients calculated using Monte Carlo simulations.

| | Backscattering Coefficient (%) | | |
|---|---|---|---|
| Material | 1.4 keV | 2.5 keV | 4.0 keV |
| $Y_2O_3$ | 36.865 | 37.19 | 37.425 |
| MgO (73 Å) /$Y_2O_3$ | 36.3 | 37.215 | 37.825 |
| MgO (146 Å) /$Y_2O_3$ | 26.03 | 34.835 | 37.195 |
| $Al_2O_3$ (78 Å) /$Y_2O_3$ | 32.7 | 36.77 | 37.54 |
| $Al_2O_3$ (156 Å) /$Y_2O_3$ | 25.94 | 29.67 | 36.6 |

No backscattering simulations were performed for the $Y_2SiO_5$ samples.

Table 8

Optical constants for selected materials.

| Material | N | k |
|---|---|---|
| $SiO_2$(reference) | 1.46 | 0 [c] |
| MgO | 1.736 [a] and 1.752 [b] | 0 [c] |
| $Al_2O_3$ | 1.765 [a] | 0 [c] |
| $Y_2O_3$:Eu | 1.93 | 0 [c] |
| Si | 3.85 | -.02 |

[a] data taken from CRC Handbook

[b] Based on a linear fit to data from OPTICAL WAVES IN LAYERED MEDIA by Pochi Yeh 500 nm – n=1.76; 1000 nm – n=1.72

[c] Actual values are on the order of $10^{-7}$, which is insignificant in the calculations used for this work

# CHAPTER 6
# DISCUSSION

## Introduction

In Chapter 4, cathodoluminescence data were presented for coatings of MgO and $Al_2O_3$ ablated onto powders of $Y_2O_3$:Eu and $Y_2SiO_5$:Tb by pulsed laser deposition. It was seen that the coatings caused a reduction in the cathodoluminescent intensity from the phosphors. Also, thicker coatings caused a larger attenuation of the intensity. In Chapter 5, a model was presented to help explain and predict the loss in luminescence from the coated samples. In this chapter, the validity of the model and its implications for the effects of the coatings will be discussed.

## Initial Uniform Coating Model

Before development of the model discussed in Chapter 5, a model had been developed to predict the cathodoluminescence from a coated sample, based on the assumption of a uniform coating. This earlier model was designed to predict the loss in luminescence at a single beam energy and coating thickness. Corrections for the fractional contribution to the luminescence based on incident angle and backscattering coefficient were incorporated to help improve the accuracy of the calculation. As with the model presented in Chapter 5, it was assumed that the coatings were acting as dead layers, i.e., they were absorbing energy from the incident electrons and therefore

reducing the energy available to produce luminescence in the phosphor. An energy loss calculation was performed based on Rao-Sahib and Wittry's modified Bethe stopping power equation. The ranges used in the calculation were obtained by measuring trajectories in a Monte Carlo simulation program. Data were fit by comparison of the energy determined by the calculation to that determined from the luminescence intensity versus beam energy curves.

Although the model appeared to give reasonable fits to the energy loss in the coating layers, there were a few drawbacks that limited its applicability. First, it only allowed for prediction of the energy loss (and therefore the luminescence) at a single thickness and energy. If an additional energy or thickness was desired, the calculation had to be repeated, which meant running new Monte Carlo simulations with the updated parameters. In order to get accurate statistical averaging, many trajectories had to be measured with the simulations. This caused the energy loss calculation to be very time-consuming, and therefore prediction of the coated phosphor's luminescence at more than a few selected energies was unfeasible.

Another drawback to this initial model was that it only worked for coatings less than about 175 Å. For thicker coatings, the model could not predict the energy loss accurately. This was especially noticeable with the thicker coatings on the $Y_2SiO_5$:Tb powders from the second set of samples (see Coating Thickness and Uniformity section in Chapter 4). The model predicted that electrons should not be able to penetrate a coating that was thicker than their path length. Therefore, no luminescence should be present at beam energies below the point at which the electron penetration range equals the thickness of the coating. This was not the case with the thicker set of coatings, which

continued to display luminescence well below this point. The reason for this discrepancy and the method used to fix it will be discussed in the new model below.

One of the biggest problems with modeling the effects of the coatings on the phosphor luminescence is getting an accurate determination of the thickness of the coating on the phosphor. In this study, two different methods were used for determining coating thickness. The thickness on the first set of samples was determined by measuring the thickness of films grown, under the same conditions as those for the powders, for 5 minutes and using a linear growth rate extrapolation. These included the following samples: MgO (4 min.)/$Y_2O_3$:Eu, MgO (8 min.)/$Y_2O_3$:Eu, $Al_2O_3$ (1.2 min.)/$Y_2O_3$:Eu, $Al_2O_3$ (2.4 min.)/$Y_2O_3$:Eu, and $Al_2O_3$ (1.2 min.) /$Y_2SiO_5$:Tb. Thickness for the second set of samples was found from the Si masks used to cover these samples during deposition. These included the following samples: MgO (4 min.)/$Y_2SiO_5$:Tb, MgO (8 min.)/ $Y_2SiO_5$:Tb, $Al_2O_3$ (5 min.)/$Y_2SiO_5$:Tb, and $Al_2O_3$ (5 min. in new chamber)/$Y_2SiO_5$:Tb. Values obtained from the second set are assumed to be more accurate since they were taken from the masks used to cover the samples during the actual deposition. In the discussion of the model below, it is shown that the thicknesses for the first set of samples may be greater than originally believed, based on the linear growth rate extrapolation.

This initial model assumed a uniform coating on the phosphor surface. Since there was a uniform deposition flux over a spherical particle surface, this is not a realistic depiction of the coating thickness. Therefore, results could not predict the luminescence from the coated sample accurately. The use of the Rao-Sahib and Wittry stopping power equation also reduced the accuracy of the calculation at energies below about 3 keV, as discussed below. A new model was developed to account for the non-uniform coating.

**Validity of the Energy Loss Model**

To overcome the problems of the initial model, a new model was developed; this new model was discussed in Chapter 5. The new model allows for fast and accurate calculation of the cathodoluminescence intensity from a coated phosphor over the entire energy range up to 4 keV. In this model, the coating thickness was assumed to have a cosine dependence, as predicted from the incremental area of the spherical phosphor surface as compared to that same area of the incident coating flux. From the non-uniform coating thickness, it was found that the electron path length through the coating is nearly the same irrespective of where the electron enters the coating, assuming that there is no diffuse scattering. The electron energy loss was then predicted for beam energies from zero to 4 keV using Rao-Sahib and Wittry's modified Bethe stopping power equation. Luminescence for the coated particle was then calculated based on this new lower energy electron. Calculated curves agreed well with the measured luminescence from the coated phosphors at energies above about 3 keV, but they overestimated the attenuation of the luminescence at lower energies. To provide a more accurate fit, a new energy loss equation was introduced based on a modification of the Makhov power loss equation for thin films.

The modification of the Bethe stopping power equation proposed by Rao-Sahib and Wittry has been widely referenced as an accurate prediction of the energy loss at beam energies of about 4 keV and up, although some suggest that the low energy limit is closer to 1 keV. When used to predict the luminescence from the second set of coated samples, this equation gave accurate results for the high-energy (about 3 keV and up,

depending on the sample) region of the curves. However, at low energies, the luminescence predicted was lower than that measured from the samples. The calculated luminescence for the first set of samples found using the linear extrapolation thicknesses was much lower than the measured luminescence. The most probable explanation for this is that the samples used to measure the thicknesses were deposited under slightly different conditions than those used for the coatings ablated onto the phosphors. This is possible since the films grown on the Si to determine the thicknesses were deposited after the coatings were ablated onto the phosphors, and there is no way to ensure that the two were exactly the same thickness.

For the modeling of the data, it was assumed that the modified Bethe stopping power equation was an accurate prediction of the energy loss for beam energies from about 3 keV and higher. The thickness of the coatings was then adjusted so that the calculated and measured luminescence from the coated samples matched over this energy range. The thickness values determined in this manner closely agreed with those found from ellipsometry for the second set of samples. However, the values for the first set of samples was almost double that found from ellipsometry, for reasons mentioned in the previous paragraph. For a comparison of the thickness values, see Table 9 at the end of this chapter.

As stated earlier, the luminescence at low energies calculated through application of a modified Bethe stopping power equation predicted a larger attenuation than was measured from the samples. The Bethe stopping power equation is based on an average stopping power for the electrons. It does not include the cross-section for scattering of the electrons as they travel through the material. In applications of beam energies above

about 4 keV, this is not a problem because the low energy region of the electron trajectory does not contribute greatly to the overall process. However, for beam energies below this value, the low energy electrons need to be taken into account to get an accurate representation of the electron stopping power. The Rao-Sahib correction to the original Bethe equation is a parabolic extrapolation that allows for energies below the inflection point of the original equation at E = 6.338 J, where E is the electron energy and J is the mean ionization potential for all energy loss processes. Therefore, it does not specifically address the low energy electron stopping power, but rather retains the form of the original equation. Therefore, the Rao-Sahib stopping power equation overestimates the stopping power for low energy electrons.

To provide a more accurate fit to the low energy electrons, the scattering of the electrons as they traverse the coating layer should be considered. The screened Rutherford scattering cross section is widely used for computation of the scattering of electrons in solids. However, at energies below 20 keV or for materials with high atomic numbers, the Mott cross section is needed to give an accurate representation of the scattering of the energetic electrons with the lattice.[24] The Mott cross section equation is more accurate in these situations because it is derived from a more exact treatment of the elastic scattering using quantum mechanics. However, there is no straightforward method of calculating the Mott scattering cross section based on materials parameters alone. Some Monte Carlo simulations utilizing these expressions rely on databases of measured scattering at incremental energies and use various extrapolation procedures to determine the intermediate energies. Others use expressions that give an approximation of the Mott scattering based on the Rutherford scattering expression, although these still

require knowledge of the scattering from the material of interest to find the fitting parameters.[31, 131, 137]

Since calculation of the Mott scattering cross sections required knowledge of the scattering in the two coating materials, it was beyond the scope of this research project. Instead, an improved energy loss calculation was sought that would account for the extended range of the low energy electrons. Researchers such as Kanaya et al. and Love et al. have suggested stopping power equations that extend the useful range of the Bethe equation to lower energies. The problem with most of these equations is that they require the use of multiple fitting parameters and, in cases where more than one beam energy dependent term is used, do not allow for convenient determination of the electron energy loss upon integration. To keep the number of fitting parameters to a minimum and still provide an accurate fit to the energy loss at low beam energies, an energy loss equation similar to one suggested by Kingsley and Prener was chosen.[96] The new energy loss equation is:

$$E = E_0 \exp\left(\frac{-2x}{a' * E_0^{k'}}\right)$$

where E is the energy at a point x along the path length, $E_0$ is the incident beam energy, and a′ and k′ are fitting parameters for the material of interest. For a coating applied to a phosphor, the fitting parameters should only be dependent upon the properties of the coating material since the reduction in luminescence comes from energy loss processes in the coating layer.

Results of the calculated cathodoluminescence intensity as a function of beam energy using the above energy loss equation are shown in Figures 5-20 through 5-28.

Comparison with the measured luminescence from coated samples shows that the new equation allows for very accurate prediction over the entire energy range up to 4 keV. The fitting parameters were found to be 0.064 for a′ and 1.36 for k′ when the coating thickness is measured in micrometers and the energy terms are in keV. These constants were found to be appropriate for all coating thicknesses studied and for both coating materials, although the constants are not expected to be the same for all coating materials. The similarity in density, average atomic number, and average atomic weight of MgO and $Al_2O_3$ could account for the fact that the same fitting parameters worked for both materials.

Due to the need to find the two fitting parameters (a′ and k′) for a given coating material, one coating will have to be deposited onto a phosphor. The Mathcad program can then be used to find the values of a′ and k′ for this coating material. Once these are determined, the coating's effect on the cathodoluminescence can be predicted for any other thickness simply by changing the thickness value in the Mathcad program. This allows for very fast and accurate prediction of the attenuation of the luminescence intensity at any desired thickness and any beam energy up to 4 keV. Given the trade-off between loss in intensity and reduced degradation with thicker coatings, this program can be used, along with knowledge of the degradation resistance at various coating thicknesses, to determine the optimal coating thickness for a particular application.

It is claimed that this model is accurate for beam energies less than 4 keV. This upper limit was chosen because no data were available at higher energies due to limits imposed by the electron gun used to excite the luminescence. However, if the energy loss function is examined for higher energies, it is found to closely follow the Bethe

energy loss function. As mentioned earlier in this section, the Bethe energy loss function is believed to be accurate for beam energies above about 4 keV. Therefore, since the two functions are almost identical in this high-energy range, the model presented in this section should also be accurate for energies above 4 keV.

No further corrections were added to the model because it provided an accurate fit of the cathodoluminescence data from the coated samples over the energy range of interest. Possible corrections could have included: backscattering coefficient, scattering, surface recombination velocity, varying activator concentration in the phosphor, and surface roughness. These are discussed below.

### Backscattering Coefficient

In Chapter 5, it was shown that the coated phosphors displayed a different backscattering coefficient than the uncoated phosphors. The difference in backscattering was dependent on the coating material, thickness, and incident beam energy. Monte Carlo simulations were used to determine the value of the backscattering coefficient at selected beam energies and coating thicknesses. At higher energies, the backscattering coefficients of the coated and uncoated phosphor were similar. This is due to the increased interaction volume at higher energies, which means that the coating contributes less to the overall electron solid interaction. Therefore, any correction to the model is only a concern at low energies (below about 2 keV, dependent on the material). It is possible that the new energy loss expression accounts for the change in the backscattering coefficient due to the fitting procedure. However, this does not seem reasonable, given that the same fitting parameters were used for both of the coating materials, although

their backscattering coefficients will be different. Also, as discussed in Chapter 5, the backscattering coefficients are measured as the electrons leave the surface of the coating. To accurately account for a change in backscattering, the number of electrons that leave the phosphor, and not the coating layer, is needed. This value could not be found using the simulations in their present form. Since the model showed good agreement between the calculated and measured luminescence without a backscattering correction, and since the backscattering coefficient from the Monte Carlo simulations is not an accurate measure of a change in the number of electrons in the phosphor itself, this correction was not included into the model.

### Scattering

Scattering of the incident electrons will change their path length in the coating layer. At higher beam energies, the mean free path of the electron in a solid is larger, and therefore scattering is not as much of a concern as it is at low energies. Although a correction was not explicitly included in the model to account for scattering, the new energy loss equation could inherently be taking the low energy scattering into account. It was assumed that the Bethe stopping power equation did not provide an accurate fit of the energy loss at low beam energies because it overestimated the stopping power of these electrons. The explanation of this is that the Bethe stopping power equation assumes an average path length based on scattering of the electrons. At low energies, the expression is no longer an accurate depiction because the process is dominated by electrons with a longer than average path length. To account for this low energy region,

the new energy expression was incorporated into the model. Therefore, the scattering of the low energy electrons is included in the model through the energy loss calculation.

**Surface Recombination and Charging**

Surface recombination refers to the loss of excited electrons from the bulk of the phosphor to nonradiative de-excitation at surface states. As discussed in Chapter 2, certain coatings have been shown to increase the efficiency of phosphors at low voltages. It has been suggested that this is a result of band misalignment that repels generated secondary electrons from the surface and therefore reduces charging of the phosphor. If this is the case, then large bandgap materials, such as those used for this work, should exhibit this behavior under ideal conditions. However, no enhancement was observed over the entire voltage range studied. Comparison of the measured luminescence curves found in Figures 5-20 through 5-28 with those of Kingsley and Prener, shown in Figures 2-14 and 2-15, show a similar low-voltage behavior. Since the curves in Figures 2-14 and 2-15 are for undoped ZnS coated onto ZnS:Cu, no enhancement from surface recombination velocity reduction is expected because the bandgaps are the same. Since the curves measured on the MgO- and $Al_2O_3$-coated $Y_2O_3$:Eu and $Y_2SiO_5$:Tb displayed a nearly identical functional dependence at low voltages, it is assumed that no reduction in surface recombination velocity is occurring in these samples.

The time-resolved cathodoluminescence results shown in Figures 4-36 through 4–53 also reveal that no surface recombination velocity change resulted from the coating. All changes in the curves in these figures can be attributed to a reduction in the beam energy on the incident electrons. If the coating had reduced the surface recombination,

then the non-radiative decay rate would be reduced. Since the overall decay rate is the sum of the radiative and non-radiative decay rates, a reduction in the non-radiative rate would have led to a reduction in the overall rate. This would have shown up as a smaller slope on the pulsed CL curves. No such change could be detected. Therefore, no reduction in the charging of the phosphors was observed with the pulsed laser deposited coatings used in this work.

### Surface Segregation

In Chapter 4, it was found that the Eu concentration in the $Y_2O_3$:Eu samples was higher in the near surface region of the phosphor. This was based on a change in the peak height ratios of the normalized luminescence versus wavelength plots of Figures 4–11 through 4-14. No such problem was found in the $Y_2SiO_5$:Tb samples, shown in Figures 4-15 to 4-18. Since the model was able to accurately predict the luminescence from coated samples of both types of phosphor, the surface segregation correction was assumed to be small. However, it could improve the accuracy of the model slightly for the low-voltage region of the $Y_2O_3$:Eu samples if included. To implement such a change would require knowledge of the Eu concentration as a function of depth and the luminescent efficiency as a function of Eu concentration in $Y_2O_3$. Similar curves would be necessary if the model were to be applied to a different phosphor. Since the goal of this model was to allow prediction of the coating's effect on the luminescent intensity from a wide range of materials systems, and since inclusion of the activator concentration quenching would only slightly improve the accuracy of the calculation, it was not included.

**Surface Roughness**

Rough surfaces have been shown to increase the light radiated from a phosphor surface. This is presumably due to enhanced coupling of the light transmitted from the phosphor because of scattering at the surface. For the present work, commercially available phosphors were chosen. These undergo a series of processing steps, such as ball milling, which result in a slightly rough surface. Therefore, the coating is unlikely to cause a large increase or decrease in the surface roughness for these materials. However, if this model were applied to phosphors grown under controlled conditions to produce very smooth surfaces, then increases in surface roughness due to a coating process might need to be considered.

Table 9

Coating thickness based on ellipsometry measurements and fitting in the Mathcad programs.

| | Thickness from Ellipsometry (Å) | Thickness from Mathcad program (Å) |
|---|---|---|
| MgO (4 min) / $Y_2O_3$:Eu | 73 (a) | 130 |
| MgO (8 min) / $Y_2O_3$:Eu | 146 (a) | 390 |
| $Al_2O_3$ (1.2 min) / $Y_2O_3$:Eu | 78 (a) | 100 |
| $Al_2O_3$ (2.4 min) / $Y_2O_3$:Eu | 156 (a) | 210 |
| $Al_2O_3$ (1.2 min) / $Y_2SiO_5$:Tb | 78 (a) | 140 |
| $Al_2O_3$ (5 min) / $Y_2SiO_5$:Tb (grown in new chamber) | 545 (b) and 489 (c) | 510 |
| $Al_2O_3$ (5 min) / $Y_2SiO_5$:Tb | ~ 1100 (d) | 2300 |
| MgO (4 min) / $Y_2SiO_5$:Tb | 290 (b) and 268 (c) | 290 |
| MgO (8 min) / $Y_2SiO_5$:Tb | 549 (b) and 494 (c) | 430 |

(a) Based on a linear growth rate extrapolation of measurements taken from films of the same materials grown on Si substrates for 5 minutes under identical conditions. $Al_2O_3$ film (5 minutes) = 325 Å from ellipsometry and about 340 Å from TEM
MgO film (5 minutes) = 91 Å from ellipsometry

(b) Data taken on multiple wavelength ellipsometer and fit assuming an 18 Å $SiO_2$ film between the substrate and film due to oxidation of the Si.

(c) Data taken on single wavelength ellipsometer.

(d) Approximation made from step height on stylus profilometer.

# CHAPTER 7
# SUMMARY AND CONCLUSIONS

Coatings of MgO and $Al_2O_3$ were deposited onto sedimented screens of $Y_2O_3$:Eu and $Y_2SiO_5$:Tb by pulsed laser deposition. A Si shadow mask was used during deposition to cover half of the sample. This allowed side-by-side comparison during characterization of coated and uncoated phosphors that had experienced the same processing. Cathodoluminescence data were collected at a constant current density of 0.16 $\mu A/cm^2$ for beam energies of 0.8, 1.4, 2.5, and 4.0 keV. The spectra revealed that the coatings caused a decrease in the cathodoluminescence for all wavelengths in the visible range. Coatings deposited for longer times, which were therefore thicker, attenuated the luminescence more strongly. Based on ellipsometry measurements from the Si shadow masks, the thickness of the measured coating varied from 73 to 550 Å. This is close to the thickness estimated for powders based on modeling of the luminescence data; the estimated thicknesses range from about 100 to 510 Å.

Spectra from the phosphors showed that the coatings had no effect on the wavelength dependence of the emission peaks. Luminescence is generated from an activator site when an excited secondary electron recombines with an available hole to return to the ground state. The wavelength of the emitted light will depend on the difference in the energy levels of the activator site. Therefore, if the energy levels of the activator are disturbed, the wavelength of the emitted light will be shifted. Since no such

shift was observed in the coated samples, it was concluded that the coatings did not alter the electronic states of the activator sites in the phosphors.

The cathodoluminescence spectra were also normalized to the intensity of the main emission peak. This allows for examination of the intensity ratio of all other peaks to the main peak. A change in this ratio can give information about the phosphor and coating. The $Y_2O_3$:Eu samples showed an increase in the ratio of the $^5D_1$ / $^5D_0$ peak heights (591 nm / 611 nm) with increasing beam energy in both coated and uncoated powders. Based on work by Tseng et al.[130] and the increased interaction volume of electrons at higher beam energy, the spectra suggest an increase in the Eu concentration near the surface of the phosphor. The effect is not attributed to the coating, but instead to segregation during synthesis. The normalized $Y_2SiO_5$:Tb spectra showed no change in the peak height ratios over the entire range of interest (460 to 680 nm). This suggests a uniform Tb concentration in the phosphor.

A concern when depositing coatings onto phosphor materials is the deactivation of luminescent centers. This can be caused by one of the following two processes: the Eu can diffuse out of the phosphor into the coating, or one of the coating constituents can diffuse into the phosphor. Either of these processes would lead to a change in the concentration of active luminescent sites, which would show up as a change in the peak height ratios on the normalized CL graph. Neither of these processes occurred in the present study.

A model was developed to predict the luminescence from the coated samples. It relied on the assumption that the coating was acting as a dead layer on top of the phosphor. As electrons passed through the coating, they lost energy that was then

unavailable for excitation of luminescence in the phosphor. The model was designed to allow for prediction of the luminescence over the entire energy range up to 4 keV and at any given thickness. A cosine-dependent coating thickness was used because it is a realistic approximation of a coating deposited from a uniform flux onto a spherical surface. From this approximation of the coating thickness, it was found that the path length through the coating is the same irrespective of the incident point of the electron, assuming no diffuse scattering. Therefore, only one angle needed to be considered for calculating the coating's effect on the luminescence.

The Rao-Sahib and Wittry modification to the Bethe stopping power equation was used in the first attempt to calculate the energy loss in the coating. It was found to only provide an accurate fit for the higher energy region of the curves. Below about 3 keV, depending on the sample, the calculation overestimated the attenuation of the luminescence intensity. This was attributed to the averaging of the electron scattering in the stopping power equation. To provide a more precise energy loss equation for the low energy electrons, a new formula was incorporated. It had the following form:

$$E = E_0 \exp\left(\frac{-2x}{a' * E_0^{k'}}\right)$$

where E is the electron's energy at a distance x into the material, $E_0$ is the incident beam energy, and a′ and k′ are fitting parameters for the material of interest. By fitting the constants a′ and k′ for a given material, the attenuation in the cathodoluminescence intensity could be predicted for any given thickness. The a′ and k′ values found for MgO and $Al_2O_3$ were the same and were equal to 0.064 and 1.36, respectively. The fact that both materials displayed the same constants is likely due to the similarity in density,

average atomic number, and average atomic weight of these materials; it cannot be stated as a general conclusion.

The model presented in this work allows for accurate prediction of the cathodoluminescence from coated phosphors. Application to a different materials system would require the fitting of the luminescence intensity versus beam energy for one coating of known thickness to determine the constants in the energy loss equation (a′ and k′). Afterwards, the luminescence could be predicted for any other thickness.

Since the model was developed to explain the effect of wide-bandgap oxide coatings, no absorbance of the emitted light was included. If the model were to be applied to a material with a bandgap comparable to or smaller than the emitted light, then absorbance would need to be included. This requires knowledge of the absorption coefficient of the coating material and the thickness of the film.

It has been shown recently that certain coatings, when applied to phosphors, can lead to an increase in the low voltage efficiency of the phosphors. This is presumably due to a band offset between the coating and phosphor. Generated secondary electrons in the phosphor are then repelled from the coating-phosphor interface to minimize or avoid surface recombination. A reduction in the surface recombination velocity gives a higher brightness.[15, 93, 104] Although the use of wide-bandgap oxides potentially could have produced such results in the present study, no enhancement of the low voltage efficiency was observed.

In order to realize a commercially available FED, device lifetime needs to be improved. Phosphor degradation is one of the major hurdles to be overcome to reach this goal. As suggested by numerous studies, applying a coating to the phosphors may be the

best way of extending their lifetime. Although deposition of a coating onto a phosphor may reduce degradation and therefore increase lifetime, results of this study and other research indicate that coating phosphors reduces their cathodoluminescence intensity. The selection of coating material type and thickness for a given application should therefore be based on the trade-off between a loss in intensity and slower degradation. Information gained from the model developed in this work should be used in making such a decision.

APPENDIX A
MATHCAD DATA AVERAGING PROGRAM

This is a Mathcad program to convert data files from the Hewlett-Packard Infinium oscilloscope using a sliding interval averaging calculation. The data are reduced to a/g points with the moving average. A two-point log time derivative and slope calculations for sections of the decay curve are also included.

$a := 25000$ number of data points in ASCII files

$g := 25$ number of data points in interval for moving average

$e := \frac{a}{g} - 2$

$y := 1, 2 .. e$ final data point index

$z := 0, 1 .. (g - 1)$ floating avgerage index

$M := data$ data file

The Infinium oscilloscope records a number of data points before the pulse trigger. The average of these is used to find a background value. This background value is then subtracted from the rest of the signal.

$f := 20$ number of points for zero calculation

$M_{f,0} = -5.3 \cdot 10^{-7}$ used to ensure zero calculation is in prepulse region

$$d := \sum_{y=0}^{f} \frac{M_{y,1}}{f+1}$$

$d = -1.9 \cdot 10^{-4}$ dark CL value

$$N_{y,0} := \frac{\sum_{z} M_{g \cdot y + z, 0}}{g} \qquad N_{y,1} := \frac{\sum_{z} M_{g \cdot y + z, 1}}{g}$$

moving time average

$A_y := -N_{y,1} + d$ Take negative of the intensity to give positive values and then subtract background

WRITEPRN("test.prn") := A Writes time averaged data to a .prn file in the winmcad directory for use in slidewrite (data is properly zeroed).

The beam energy is 1.4 keV

The sample is $Y_2SiO_5$:Tb coated with $Al_2O_3$ (1.2 min)

3-70 filter in PMT box

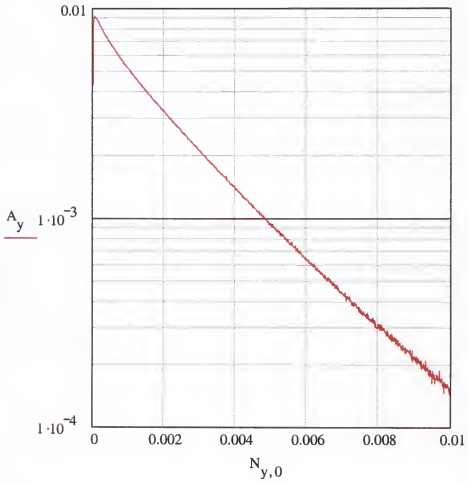

$A_e = 1.4744 \cdot 10^{-4}$

$k := 1, 2 .. e - 1$ index for two point log time derivative

$$B_k := \frac{\left(A_k - A_{k+1}\right) \cdot 2}{\left(N_{k+1,0} - N_{k,0}\right) \cdot \left(A_{k+1} + A_k\right)}$$ negative of two point log time derivative

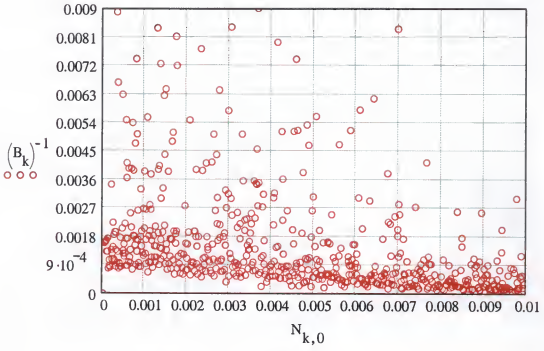


Below is the code to calculate the decay constant over a given data interval.

$s := 900$ start data point

$q := 998$ end data point

$N_{s,0} = 8.99627 \cdot 10^{-3}$ start time

$N_{q,0} = 9.97627 \cdot 10^{-3}$ end time

$j := 0, 1 .. (q - s)$

$p_j := \ln\left(A_{s+j}\right)$ $r_j := N_{s+j,0}$

$h := -(\text{slope}(r, p))^{-1}$

$h = 2.881148 \cdot 10^{-3}$ average decay time constant at long times

The following is a repeat of the earlier code over an interval at the beginning of the pulse.

$u := 80$ start

$t := 120$ end

$N_{u,0} = 7.9627 \cdot 10^{-4}$ start time

$N_{t,0} = 1.19627 \cdot 10^{-3}$ end time

$m := 0, 1 .. (t - u)$

$l_m := \ln(A_{u+m})$ $s_m := N_{u+m,0}$

$h := -(\text{slope}(s, l))^{-1}$

$h = 1.956926 \cdot 10^{-3}$ average decay time constant at short times

APPENDIX B
LUMINESCENCE DUE TO THE INCIDENT ANGLE OF THE ELECTRONS

This is a Mathcad program to compute the modified probability function taking into account the thickness variation across a spherical particle coated with a uniform incident flux from the top. Curves are plotted for coating thicknesses of 0, 0.2, 0.4, 0.6, 0.8, 1, and 2 μm. It should be noted that the coatings used for the research project are thinner than those shown in this program. These larger coatings were chosen to represent the behavior of the equations over a range of coating thicknesses. Refer to Figure 5-11 for a schematic of the particle and coating. The derivation of these equations is explained in Chapter 5.

$\theta := 1, 2 .. 90$ angle from center axis of particle

t is the coating thickness at $\theta = 0$, measured in μm

$R := 5$ radius of particle in μm

$$A(\theta, t) := \frac{\left[R^2 \cdot \sin(\theta \cdot \deg) \cdot \cos(\theta \cdot \deg) + 2 \cdot R \cdot t \cdot \sin(\theta \cdot \deg) \cdot (\cos(\theta \cdot \deg))^2 - R \cdot t \cdot (\sin(\theta \cdot \deg))^3\right]}{R^2 + R \cdot t + \frac{(t)^2}{3}}$$

$$B(\theta, t) := \frac{\left[(t)^2 \cdot \sin(\theta \cdot \deg) \cdot (\cos(\theta \cdot \deg))^3 - (t)^2 \cdot (\sin(\theta \cdot \deg))^3 \cdot \cos(\theta \cdot \deg)\right]}{R^2 + R \cdot t + \frac{(t)^2}{3}}$$

$P(\theta, t) := A(\theta, t) + B(\theta, t)$ area weighted contribution to luminescence at given angle $\theta$ and thickness t

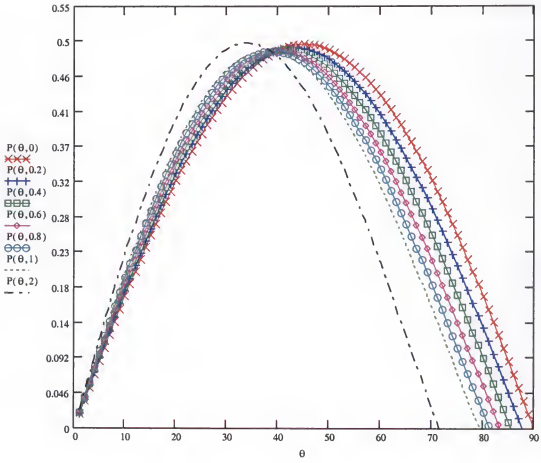


This is a plot of the area weighted contribution to the luminescence at an angle $\theta$ from the center axis of the particle. The second term in the brackets is the coating thickness in $\mu$m. As can be seen from the plot, the angle at which the contribution is maximum decreases with increasing coating thickness. This is due to the shape of the coating.

The angle from the center axis, $\theta$, is no longer equal to the angle between the incident electron and surface normal as in the uniform coating. The angle from surface normal as derived in Chapter 5 is given by the following.

$$\psi(\theta,t) := \operatorname{acot}\left[\frac{R\cdot\cos(\theta\cdot deg)+t\cdot(\cos(\theta\cdot deg))^2-t\cdot(\sin(\theta\cdot deg))^2}{R\cdot\sin(\theta\cdot deg)+2\cdot t\cdot\cos(\theta\cdot deg)\cdot\sin(\theta\cdot deg)}\right]$$

angle from surface normal at given $\theta$

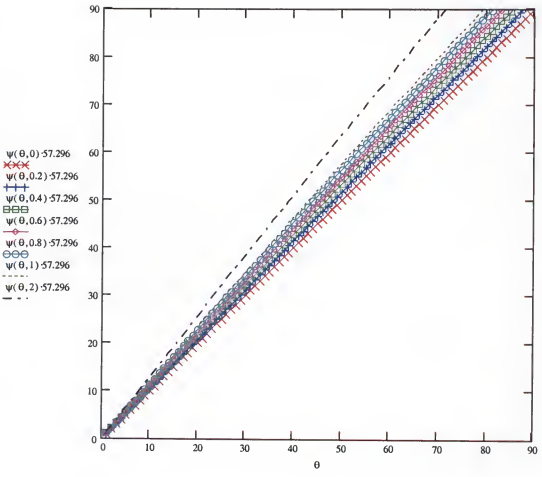


This is a plot of the angle from surface normal of the electron beam as a function of θ for various coating thickness. The second term in the brackets is the coating thickness measured in μm.

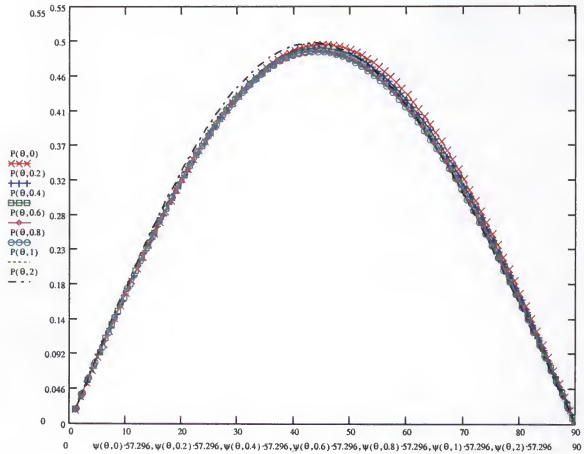


This is a plot of the area weighted contribution at a given angle as a function of the angle $\Psi$. Similar to Figure 5-4 for a uniform coating thickness, the contribution is maximum at about 45 degrees.

APPENDIX C
NONUNIFORM COATING SHAPE

This is a Mathcad program to determine the shape of the coating based on a uniform incident particle flux onto a spherical surface. Refer to Figure 5-11 for a schematic. The derivation of the equations is given in Chapter 5.

$R := 5$ radius of particle in $\mu m$

$\theta := 0, 1 .. 90$ angle from the center axis of the particle

$$\gamma(\theta, t) := \text{asin}\left[\frac{(R + t \cdot \cos(\theta \cdot \text{deg}))\ \sin(\theta \cdot \text{deg})}{R}\right]$$

$r(\theta, t) := (R) \cdot \sin(\gamma(\theta, t))$

$h(\theta, t) := R \cdot \cos(\gamma(\theta, t))$ height of particle

$c(\theta, t) := (R + t \cdot \cos(\theta \cdot \text{deg})) \cdot \cos(\theta \cdot \text{deg})$ height of particle with coating

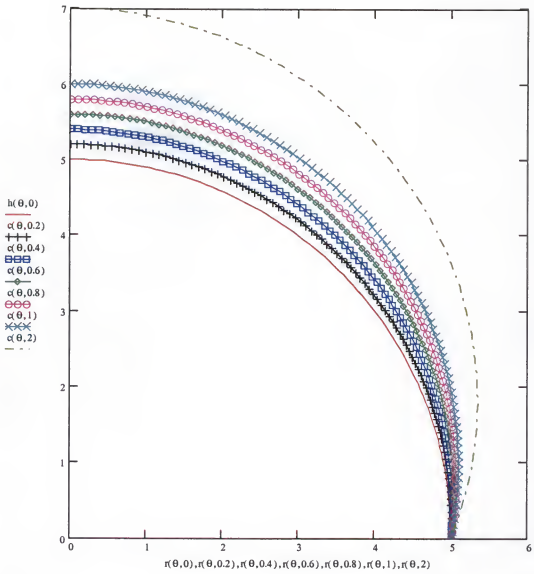


Cross-section of various thicknesses of coating on a spherical particle. The thicknesses are listed as the second term in the parentheses and are measured in μm.

$d(\theta,t) := c(\theta,t) - h(\theta,t)$ distance through the coating measured parallel to center axis

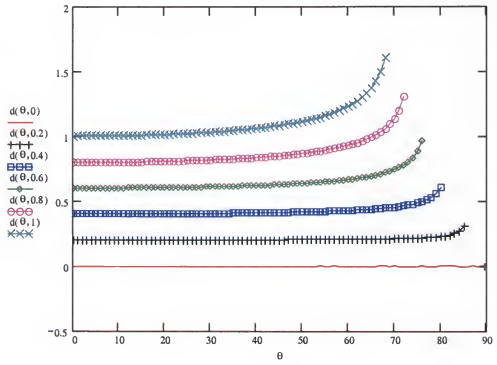


Distance through the coating, as measured parallel to the center axis, as a function of $\theta$ for various coating thicknesses. The thickness is given as the second term in the brackets. The curves increase at the very end due to the curvature of the particle. For the coatings used in this research, the distance through the coating is nearly constant for all angles, as determined from the graph above.

APPENDIX D
STOPPING POWER

This is a Mathcad program to compare the stopping power equations of Bethe, Rao-Sahib and Wittry, and Love et al. The curves have been computed for $Al_2O_3$, but they are similar for other materials.

$\rho := 3.97$ density

$Z := 10$ average atomic number

$A := 20.3922$ average atomic weight

$Ei := 0, 0.01 .. 5$ incident beam energy

$$J := \left(9.76 \cdot Z + \frac{58.5}{Z^{0.19}}\right) \cdot 10^{-3}$$ mean ionization potential in keV

$k := 0.85$ fitting parameter for ionization potential correction

$$J2(Ei) := \frac{J}{1 + k \cdot \left(\frac{J}{Ei + 10^{-50}}\right)}$$ low energy correction of ionization potential by Joy and Lou

$$S1(Ei) := \frac{7.85 \cdot \rho \cdot Z \cdot \ln\left(1.166 \frac{Ei}{J}\right)}{A \cdot Ei}$$ Bethe stopping power equation

$$S2(Ei) := \frac{7.85 \cdot \rho \cdot Z}{1.26 A \cdot (Ei\, J)^{0.5}}$$ Rao-Sahib and Wittry parabloic extrapolation of Bethe stopping power equation

$$S3(Ei) := \frac{\rho \cdot Z \cdot 10^{-4}}{A \cdot \left[1.18 \cdot 10^{-5} \cdot (J \cdot Ei)^{0.5} + 1.47 \cdot 10^{-6} \cdot Ei\right]}$$ Love et al. stopping power equation

All equations are the absolute value of the stopping power. The stopping power is a negative quantity because the atom is losing energy to the lattice as it travels through the material. However, the absolute value allows the behavior of the functions to be seen more easily.

All stopping powers are measured in keV / μm

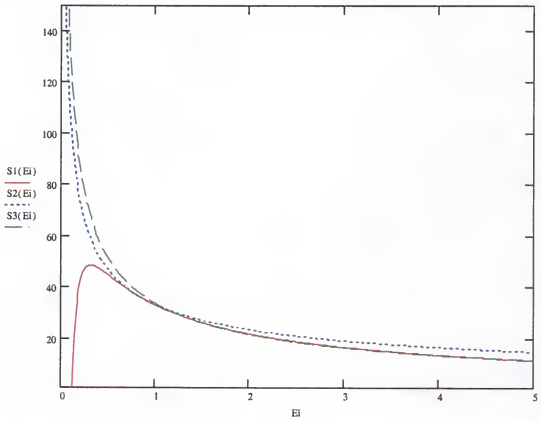


This is a plot of the stopping power equations as a function of incident beam energy. The red curve is the Bethe stopping power equation. The blue curve is the parabolic extrapolation proposed by Rao-Sahib and Wittry. The green curve is the stopping power equation of Love et al.

APPENDIX E
MATHCAD PROGRAM FOR MgO (4 min) / $Y_2O_3$:Eu

This is a Mathcad program to compute the luminescence as a function of beam energy from a 4 minute coating of MgO on $Y_2O_3$:Eu. The coating was applied by pulsed laser deposition.

$t := .013$ thickness in microns of coating at top of particle

$R := 5$ radius of phosphor particle in microns

$\rho := 3.6$ density

$Z := 10$ atomic number

$A := 20.152$ average atomic weight

$\theta := 0, 1 .. 90$ angle from center axis to coating's surface

$$\gamma(\theta) := \operatorname{asin}\left[\frac{(R + t\cdot\cos(\theta\cdot deg))\ \sin(\theta\cdot deg)}{R}\right]$$ angle from center axis to phosphor's surface

$r(\theta) := (R)\cdot\sin(\gamma(\theta))$ distance from center axis

$h(\theta) := R\cdot\cos(\gamma(\theta))$ height of phosphor particle

$c(\theta) := (R + t\cdot\cos(\theta\cdot deg))\cdot\cos(\theta\cdot deg)$ height of phosphor and coating

$d(\theta) := c(\theta) - h(\theta)$ distance traveled through the coating at given $\theta$

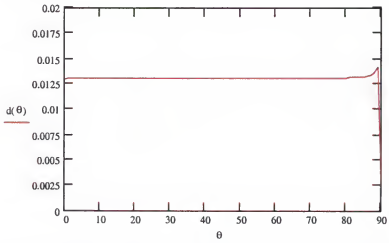


Thickness is nearly constant for all $\theta$, so take $\theta = 0$ for subsequent calculations.

$Ei := 0, .1 .. 4$ incident beam energy

$J := (11.5 \cdot Z) \cdot 10^{-3}$ mean ionization potential in keV

$k := 0.85$ fitting parameter for ionization potential correction

$$J2(Ei) := \frac{J}{1 + k \cdot \left( \frac{J}{Ei + 10^{-50}} \right)}$$ low energy correction of ionization potential

$$D(Ei) := \frac{100 \cdot 1.262 \cdot A \cdot (J2(Ei))^{\frac{1}{2}} \cdot (Ei)^{\frac{3}{2}}}{2355 \rho \cdot Z}$$ range in bulk of coating material at given incident energy Ei based on Rao-Sahib & Wittry

$D(1.4) = 0.033$

$D(2.5) = 0.079$ range in microns at beam energy (keV) inside brackets

$D(4) = 0.161$

$$E(\theta, Ei) := Ei \cdot \left(1 - \frac{d(\theta)}{D(Ei)}\right)^{\frac{2}{3}}$$ energy after traversing coating from Rao-Sahib & Wittry

$$E2(\theta, Ei) := Ei \cdot \exp\left[-2 \cdot \frac{d(\theta)}{0.064 \cdot (Ei)^{1.36}}\right]$$ fitted energy dependence

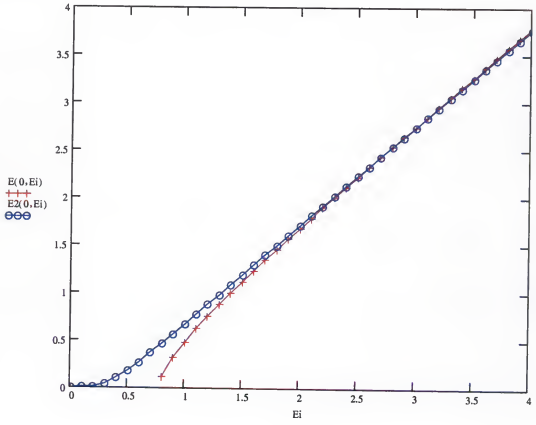


This is a plot of the electron's energy after traveling through the coating as a funciton of incident beam energy. The red curve is based on the calculation using the stopping power equation of Rao-Sahib and Wittry. The blue curve is based on the new fitted energy loss equation.

$a0 := -7.622363135166821 \cdot 10^{3}$

$a1 := 1.831378204234571 \cdot 10^{4}$

fitting coefficients for a power law fit to the uncoated phosphor luminescence, taken from SlideWrite program

$a2 := 1.43141730761361$

$L(\theta, Ei) := a0 + a1 \cdot (E(\theta, Ei))^{a2}$ luminescence of coated material based on Rao-Sahib and Wittry energy loss equation

$L2(\theta, Ei) := a0 + a1 \cdot (E2(\theta, Ei))^{a2}$ luminescence of coated material based on new energy loss equation

$Li(\theta, Ei) := a0 + a1 \cdot (Ei)^{a2}$ luminescence of uncoated material

$am0 := -9.935660035182 \cdot 10^{3}$

$am1 := 1.490338613474591 \cdot 10^{4}$

fitting parameters for measured luminescence from coated material, taken from SlideWrite program

$am2 := 1.52742562074871$

$Lm(\theta, Ei) := am0 + am1 \cdot (Ei)^{am2}$ measured luminescence from the coated phosphor

The following graph shows the cathodoluminescence intensity as a function of beam energy. The black curve is the uncoated phosphor. The green curve is the measured luminescence from the coated phosphor. The red curve is the luminescence as calculated based on the Rao-Sahib modification of the Bethe stopping power equation. The blue curve is the luminescence based on the new energy loss equation. From the graph, it can be seen that the Rao-Sahib and Wittry equation overestimates the attenuation of the luminescence at low energies. The new energy loss equation accurately predicts the luminescence over the entire energy range up to 4 keV. Measurement of the thickness of the coating on the phosphor is the largest source of error for the calculation. To provide a more accurate analysis, it was assumed that the Rao-Sahib and Wittry equation is valid for the high energy region of the curve. The thickness value was then optimized to give agreement between the calculated and measured curves around 4 keV. For further discussion of this correction, see the discussion of the second model in Chapter 6.

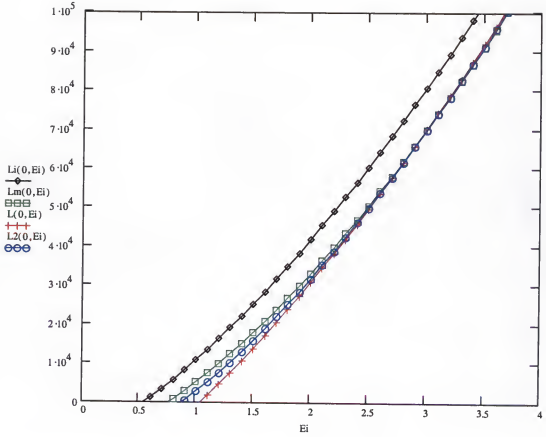


The following is the SlideWrite plot used to determine the curve fiting coefficeints for the measured luminescence from the coated and uncoated phosphor.

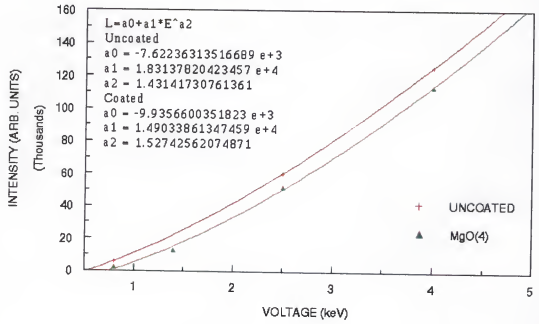

APPENDIX F
MATHCAD PROGRAM FOR MgO (8 min) / $Y_2O_3$:Eu

This is a Mathcad program to compute the luminescence as a function of beam energy from a 8 minute coating of MgO on $Y_2O_3$:Eu. The coating was applied by pulsed laser deposition.

$t := .039$ thickness in microns of coating at top of particle

$R := 5$ radius of phosphor particle in microns

$\rho := 3.6$ density

$Z := 10$ atomic number

$A := 20.152$ average atomic weight

$\theta := 0, 1 .. 90$ angle from center axis to coating's surface

$$\gamma(\theta) := \operatorname{asin}\left[\frac{(R + t\cdot\cos(\theta\cdot deg))\ \sin(\theta\cdot deg)}{R}\right]$$ angle from center axis to phosphor's surface

$r(\theta) := (R)\cdot\sin(\gamma(\theta))$ distance from center axis

$h(\theta) := R\cdot\cos(\gamma(\theta))$ height of phosphor particle

$c(\theta) := (R + t\cdot\cos(\theta\cdot deg))\cdot\cos(\theta\cdot deg)$ height of phosphor and coating

$d(\theta) := c(\theta) - h(\theta)$ distance traveled through the coating at given $\theta$

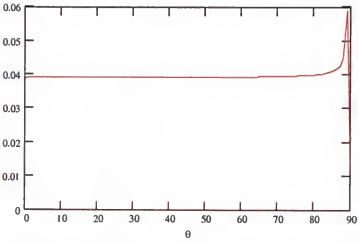


Thickness is nearly constant for all $\theta$, so take $\theta = 0$ for subsequent calculations.

$Ei := 0, .1 .. 4$ incident beam energy

$J := (11.5 \cdot Z) \cdot 10^{-3}$ mean ionization potential in keV

$k := 0.85$ fitting parameter for ionization potential correction

$$J2(Ei) := \frac{J}{1 + k \cdot \left( \frac{J}{Ei + 10^{-50}} \right)}$$ low energy correction of ionization potential

$$D(Ei) := \frac{100 \cdot 1.262 \cdot A \cdot (J2(Ei))^{\frac{1}{2}} \cdot (Ei)^{\frac{3}{2}}}{2355 \rho \cdot Z}$$ range in bulk of coating material at given incident energy Ei based on Rao-Sahib & Wittry

$D(1.4) = 0.033$

$D(2.5) = 0.079$ range in microns at beam energy (keV) inside brackets

$D(4) = 0.161$

$$E(\theta, Ei) := Ei \cdot \left(1 - \frac{d(\theta)}{D(Ei)}\right)^{\frac{2}{3}}$$ energy after traversing coating from Rao-Sahib & Wittry

$$E2(\theta, Ei) := Ei \cdot \exp\left[-2 \cdot \frac{d(\theta)}{0.064 \cdot (Ei)^{1.36}}\right]$$ fitted energy dependence

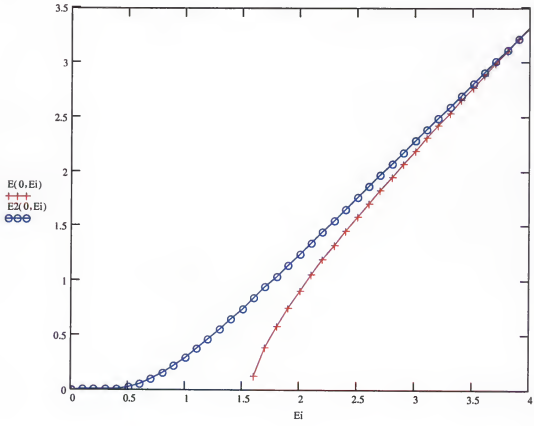


This is a plot of the electron's energy after traveling through the coating as a funciton of incident beam energy. The red curve is based on the calculation using the stopping power equation of Rao-Sahib and Wittry. The blue curve is based on the new fitted energy loss equation.

$a0 := -2.155376136556 \cdot 10^{3}$

$a1 := 7.823564662632 \cdot 10^{3}$

fitting coefficients for a power law fit to the uncoated phosphor luminescence, taken from SlideWrite program

$a2 := 1.78566539748617$

$L(\theta, Ei) := a0 + a1 \cdot (E(\theta, Ei))^{a2}$ luminescence of coated material based on Rao-Sahib and Wittry energy loss equation

$L2(\theta, Ei) := a0 + a1 \cdot (E2(\theta, Ei))^{a2}$ luminescence of coated material based on new energy loss equation

$Li(\theta, Ei) := a0 + a1 \cdot (Ei)^{a2}$ luminescence of uncoated material

$am0 := -2.066137039861 \cdot 10^{3}$

$am1 := 2.298881217481 \cdot 10^{3}$

fitting parameters for measured luminescence from coated material, taken from SlideWrite program

$am2 := 2.4293699844816$

$Lm(\theta, Ei) := am0 + am1 \cdot (Ei)^{am2}$ measured luminescence from the coated phosphor

The following graph shows the cathodoluminescence intensity as a function of beam energy. The black curve is the uncoated phosphor. The green curve is the measured luminescence from the coated phosphor. The red curve is the luminescence as calculated based on the Rao-Sahib modification of the Bethe stopping power equation. The blue curve is the luminescence based on the new energy loss equation. From the graph, it can be seen that the Rao-Sahib and Wittry equation overestimates the attenuation of the luminescence at low energies. The new energy loss equation accurately predicts the luminescence over the entire energy range up to 4 keV. Measurement of the thickness of the coating on the phosphor is the largest source of error for the calculation. To provide a more accurate analysis, it was assumed that the Rao-Sahib and Wittry equation is valid for the high energy region of the curve. The thickness value was then optimized to give agreement between the calculated and measured curves around 4 keV. For further discussion of this correction, see the discussion of the second model in Chapter 6.

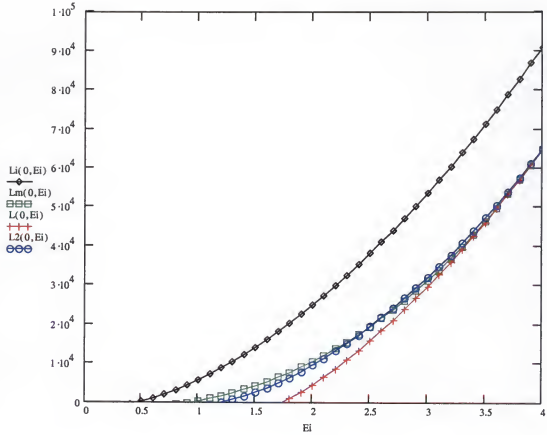


The following is the SlideWrite plot used to determine the curve fiting coefficeints for the measured luminescence from the coated and uncoated phosphor.

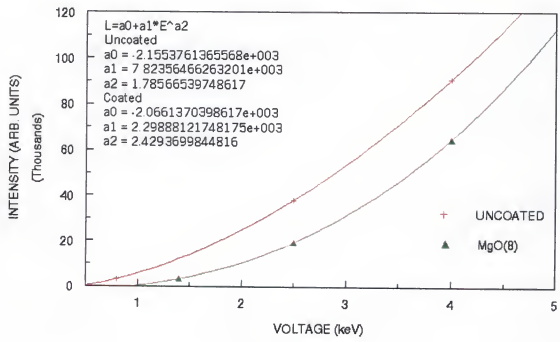

APPENDIX G
MATHCAD PROGRAM FOR $Al_2O_3$ (1.2 min) / $Y_2O_3$:Eu

This is a Mathcad program to compute the luminescence as a function of beam energy from a 1.2 minute coating of $Al_2O_3$ on $Y_2O_3$:Eu. The coating was applied by pulsed laser deposition.

$t := .01$ thickness in microns of coating at top of particle

$R := 5$ radius of phosphor particle in microns

$\rho := 3.97$ density

$Z := 10$ atomic number

$A := 20.3922$ average atomic weight

$\theta := 0, 1 .. 90$ angle from center axis to coating's surface

$$\gamma(\theta) := \operatorname{asin}\left[\frac{(R + t\cdot\cos(\theta\cdot deg))\ \sin(\theta\cdot deg)}{R}\right]$$ angle from center axis to phosphor's surface

$r(\theta) := (R)\cdot\sin(\gamma(\theta))$ distance from center axis

$h(\theta) := R\cdot\cos(\gamma(\theta))$ height of phosphor particle

$c(\theta) := (R + t\cdot\cos(\theta\cdot deg))\cdot\cos(\theta\cdot deg)$ height of phosphor and coating

$d(\theta) := c(\theta) - h(\theta)$ distance traveled through the coating at given $\theta$

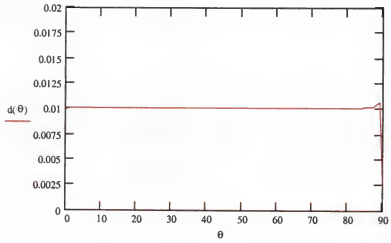


Thickness is nearly constant for all $\theta$, so take $\theta = 0$ for subsequent calculations.

$Ei := 0, .1 .. 4$ incident beam energy

$J := (11.5 \cdot Z) \cdot 10^{-3}$ mean ionization potential in keV

$k := 0.85$ fitting parameter for ionization potential correction

$$J2(Ei) := \frac{J}{1 + k \cdot \left( \frac{J}{Ei + 10^{-50}} \right)}$$ low energy correction of ionization potential

$$D(Ei) := \frac{100 \cdot 1.262 \cdot A \cdot (J2(Ei))^{\frac{1}{2}} \cdot (Ei)^{\frac{3}{2}}}{2355 \cdot \rho \cdot Z}$$ range in bulk of coating material at given incident energy Ei based on Rao-Sahib & Wittry

$D(1.4) = 0.03$

$D(2.5) = 0.072$ range in microns at beam energy (keV) inside brackets

$D(4) = 0.147$

$$E(\theta, Ei) := Ei \cdot \left(1 - \frac{d(\theta)}{D(Ei)}\right)^{\frac{2}{3}}$$ energy after traversing coating from Rao-Sahib & Wittry

$$E2(\theta, Ei) := Ei \cdot \exp\left[-2 \cdot \frac{d(\theta)}{0.064 \cdot (Ei)^{1.36}}\right]$$ fitted energy dependence

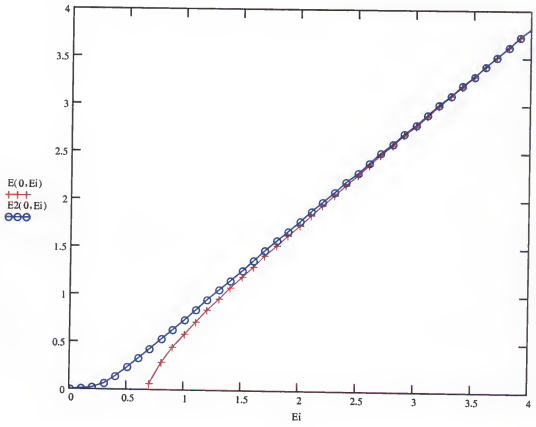


This is a plot of the electron's energy after traveling through the coating as a funciton of incident beam energy. The red curve is based on the calculation using the stopping power equation of Rao-Sahib and Wittry. The blue curve is based on the new fitted energy loss equation.

$a0 := -7.255511574997832 \cdot 10^{3}$

$a1 := 1.429400564233088 \cdot 10^{4}$

$a2 := 1.33770010631825$

fitting coefficients for a power law fit to the uncoated phosphor luminescence, taken from SlideWrite program

$L(\theta, Ei) := a0 + a1 \cdot (E(\theta, Ei))^{a2}$ luminescence of coated material based on Rao-Sahib and Wittry energy loss equation

$L2(\theta, Ei) := a0 + a1 \cdot (E2(\theta, Ei))^{a2}$ luminescence of coated material based on new energy loss equation

$Li(\theta, Ei) := a0 + a1 \cdot (Ei)^{a2}$ luminescence of uncoated material

$am0 := -6.261633176897011 \cdot 10^{3}$

$am1 := 9.605132975977211 \cdot 10^{3}$

$am2 := 1.585034834110552$

fitting parameters for measured luminescence from coated material, taken from SlideWrite program

$Lm(\theta, Ei) := am0 + am1 \cdot (Ei)^{am2}$ measured luminescence from the coated phosphor

The following graph shows the cathodoluminescence intensity as a function of beam energy. The black curve is the uncoated phosphor. The green curve is the measured luminescence from the coated phosphor. The red curve is the luminescence as calculated based on the Rao-Sahib modification of the Bethe stopping power equation. The blue curve is the luminescence based on the new energy loss equation. From the graph, it can be seen that the Rao-Sahib and Wittry equation overestimates the attenuation of the luminescence at low energies. The new energy loss equation accurately predicts the luminescence over the entire energy range up to 4 keV. Measurement of the thickness of the coating on the phosphor is the largest source of error for the calculation. To provide a more accurate analysis, it was assumed that the Rao-Sahib and Wittry equation is valid for the high energy region of the curve. The thickness value was then optimized to give agreement between the calculated and measured curves around 4 keV. For further discussion of this correction, see the discussion of the second model in Chapter 6.

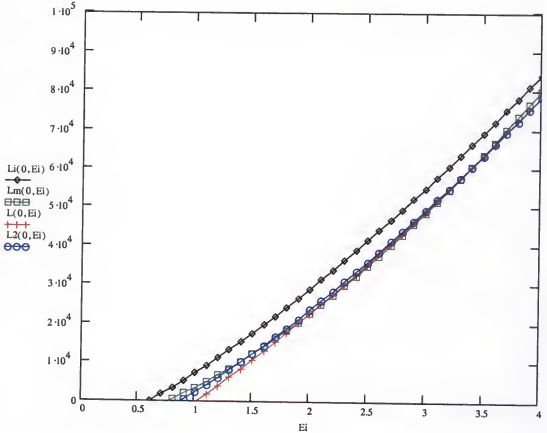


The following is the SlideWrite plot used to determine the curve fiting coefficeints for the measured luminescence from the coated and uncoated phosphor.

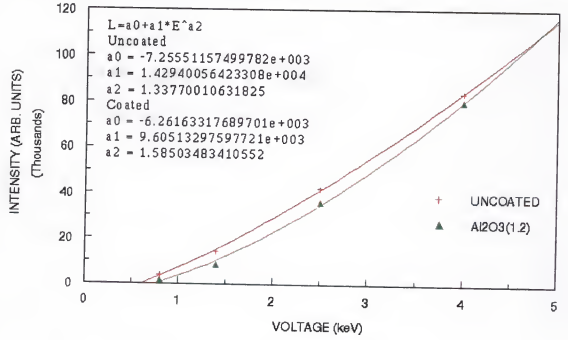

APPENDIX H
MATHCAD PROGRAM FOR $Al_2O_3$ (2.4 min) / $Y_2O_3$:Eu

This is a Mathcad program to compute the luminescence as a function of beam energy from a 2.4 minute coating of $Al_2O_3$ on $Y_2O_3$:Eu. The coating was applied by pulsed laser deposition.

$t := .021$ thickness in microns of coating at top of particle

$R := 5$ radius of phosphor particle in microns

$\rho := 3.97$ density

$Z := 10$ atomic number

$A := 20.3922$ average atomic weight

$\theta := 0, 1 .. 90$ angle from center axis to coating's surface

$$\gamma(\theta) := \operatorname{asin}\left[\frac{(R + t\cdot\cos(\theta\cdot deg))\,\sin(\theta\cdot deg)}{R}\right]$$ angle from center axis to phosphor's surface

$r(\theta) := (R)\cdot\sin(\gamma(\theta))$ distance from center axis

$h(\theta) := R\cdot\cos(\gamma(\theta))$ height of phosphor particle

$c(\theta) := (R + t\cdot\cos(\theta\cdot deg))\cdot\cos(\theta\cdot deg)$ height of phosphor and coating

$d(\theta) := c(\theta) - h(\theta)$ distance traveled through the coating at given $\theta$

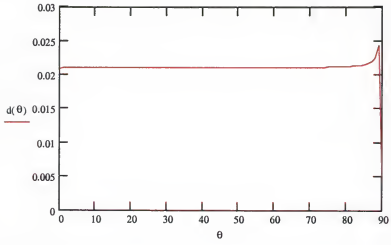


Thickness is nearly constant for all $\theta$, so take $\theta = 0$ for subsequent calculations.

$Ei := 0, .1 .. 4$ incident beam energy

$J := (11.5 \cdot Z) \cdot 10^{-3}$ mean ionization potential in keV

$k := 0.85$ fitting parameter for ionization potential correction

$$J2(Ei) := \frac{J}{1 + k \cdot \left( \frac{J}{Ei + 10^{-50}} \right)}$$ low energy correction of ionization potential

$$D(Ei) := \frac{100 \cdot 1.262 \cdot A \cdot (J2(Ei))^{\frac{1}{2}} \cdot (Ei)^{\frac{3}{2}}}{2355 \rho \cdot Z}$$ range in bulk of coating material at given incident energy Ei based on Rao-Sahib & Wittry

$D(1.4) = 0.03$

$D(2.5) = 0.072$ range in microns at beam energy (keV) inside brackets

$D(4) = 0.147$

$$E(\theta, Ei) := Ei \cdot \left(1 - \frac{d(\theta)}{D(Ei)}\right)^{\frac{2}{3}}$$

energy after traversing coating from Rao-Sahib & Wittry

$$E2(\theta, Ei) := Ei \cdot \exp\left[-2 \cdot \frac{d(\theta)}{0.064 \cdot (Ei)^{1.36}}\right]$$

fitted energy dependence

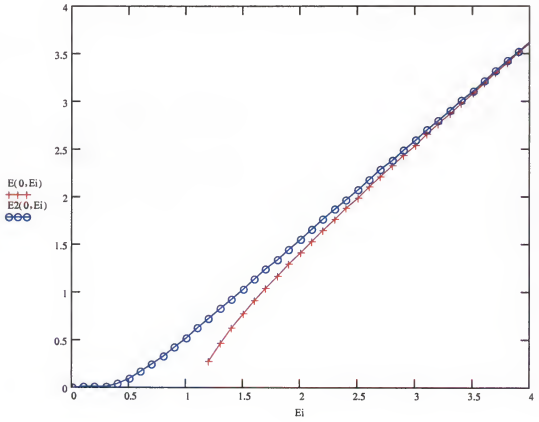


This is a plot of the electron's energy after traveling through the coating as a funciton of incident beam energy. The red curve is based on the calculation using the stopping power equation of Rao-Sahib and Wittry. The blue curve is based on the new fitted energy loss equation.

$a0 := -3.641329977677748 \cdot 10^{3}$

$a1 := 1.228971333363960 \cdot 10^{4}$

$a2 := 1.61115422022399$

fitting coefficients for a power law fit to the uncoated phosphor luminescence, taken from SlideWrite program

$L(\theta, Ei) := a0 + a1 \cdot (E(\theta, Ei))^{a2}$ luminescence of coated material based on Rao-Sahib and Wittry energy loss equation

$L2(\theta, Ei) := a0 + a1 \cdot (E2(\theta, Ei))^{a2}$ luminescence of coated material based on new energy loss equation

$Li(\theta, Ei) := a0 + a1 \cdot (Ei)^{a2}$ luminescence of uncoated material

$am0 := -6.702662158699453 \cdot 10^{3}$

$am1 := 8.207928136583680 \cdot 10^{3}$

$am2 := 1.79982256009043$

fitting parameters for measured luminescence from coated material, taken from SlideWrite program

$Lm(\theta, Ei) := am0 + am1 \cdot (Ei)^{am2}$ measured luminescence from the coated phosphor

The following graph shows the cathodoluminescence intensity as a function of beam energy. The black curve is the uncoated phosphor. The green curve is the measured luminescence from the coated phosphor. The red curve is the luminescence as calculated based on the Rao-Sahib modification of the Bethe stopping power equation. The blue curve is the luminescence based on the new energy loss equation. From the graph, it can be seen that the Rao-Sahib and Wittry equation overestimates the attenuation of the luminescence at low energies. The new energy loss equation accurately predicts the luminescence over the entire energy range up to 4 keV. Measurement of the thickness of the coating on the phosphor is the largest source of error for the calculation. To provide a more accurate analysis, it was assumed that the Rao-Sahib and Wittry equation is valid for the high energy region of the curve. The thickness value was then optimized to give agreement between the calculated and measured curves around 4 keV. For further discussion of this correction, see the discussion of the second model in Chapter 6.

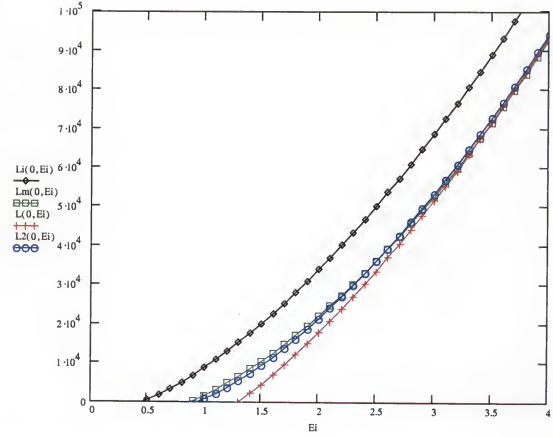


The following is the SlideWrite plot used to determine the curve fiting coefficeints for the measured luminescence from the coated and uncoated phosphor.

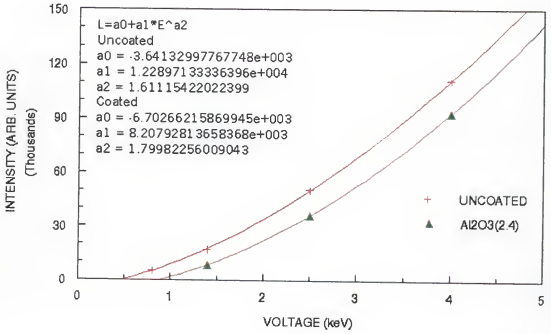

APPENDIX I
MATHCAD PROGRAM FOR MgO (4 min) / $Y_2SiO_5$:Tb

This is a Mathcad program to compute the luminescence as a function of beam energy from a 4 minute coating of MgO on $Y_2SiO_5$:Tb. The coating was applied by pulsed laser deposition.

$t := .029$ thickness in microns of coating at top of particle

$R := 5$ radius of phosphor particle in microns

$\rho := 3.6$ density

$Z := 10$ atomic number

$A := 20.152$ average atomic weight

$\theta := 0, 1 .. 90$ angle from center axis to coating's surface

$$\gamma(\theta) := \operatorname{asin}\left[\frac{(R + t\cdot\cos(\theta\cdot\mathrm{deg}))\ \sin(\theta\cdot\mathrm{deg})}{R}\right]$$ angle from center axis to phosphor's surface

$r(\theta) := (R)\cdot\sin(\gamma(\theta))$ distance from center axis

$h(\theta) := R\cdot\cos(\gamma(\theta))$ height of phosphor particle

$c(\theta) := (R + t\cdot\cos(\theta\cdot\mathrm{deg}))\cdot\cos(\theta\cdot\mathrm{deg})$ height of phosphor and coating

$d(\theta) := c(\theta) - h(\theta)$ distance traveled through the coating at given $\theta$

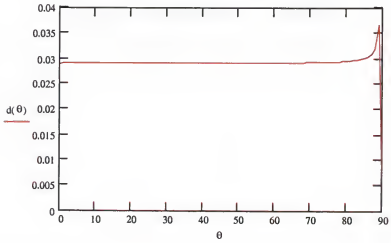


Thickness is nearly constant for all $\theta$, so take $\theta = 0$ for subsequent calculations.

$Ei := 0, .1 .. 4$ incident beam energy

$J := (11.5 \cdot Z) \cdot 10^{-3}$ mean ionization potential in keV

$k := 0.85$ fitting parameter for ionization potential correction

$$J2(Ei) := \frac{J}{1 + k \cdot \left( \frac{J}{Ei + 10^{-50}} \right)}$$ low energy correction of ionization potential

$$D(Ei) := \frac{100 \cdot 1.262 \cdot A \cdot (J2(Ei))^{\frac{1}{2}} \cdot (Ei)^{\frac{3}{2}}}{2355 \cdot \rho \cdot Z}$$ range in bulk of coating material at given incident energy Ei based on Rao-Sahib & Wittry

$D(1.4) = 0.033$

$D(2.5) = 0.079$ range in microns at beam energy (keV) inside brackets

$D(4) = 0.161$

$$E(\theta, Ei) := Ei \cdot \left(1 - \frac{d(\theta)}{D(Ei)}\right)^{\frac{2}{3}}$$ energy after traversing coating from Rao-Sahib & Wittry

$$E2(\theta, Ei) := Ei \cdot \exp\left[-2 \frac{d(\theta)}{0.064 \cdot (Ei)^{1.36}}\right]$$ fitted energy dependence

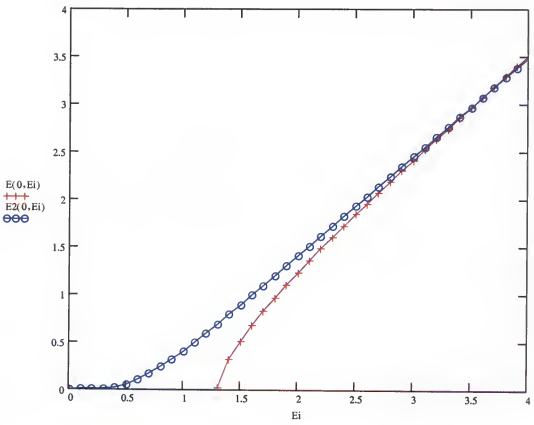


This is a plot of the electron's energy after traveling through the coating as a funciton of incident beam energy. The red curve is based on the calculation using the stopping power equation of Rao-Sahib and Wittry. The blue curve is based on the new fitted energy loss equation.

$a0 := -3.353929678955 \cdot 10^{4}$

$a1 := 1.069991526283 \cdot 10^{5}$

$a2 := 1.47933368154553$

fitting coefficients for a power law fit to the uncoated phosphor luminescence, taken from SlideWrite program

$L(\theta, Ei) := a0 + a1 \cdot (E(\theta, Ei))^{a2}$ luminescence of coated material based on Rao-Sahib and Wittry energy loss equation

$L2(\theta, Ei) := a0 + a1 \cdot (E2(\theta, Ei))^{a2}$ luminescence of coated material based on new energy loss equation

$L(\theta, Ei) := a0 + a1 \cdot (Ei)^{a2}$ luminescence of uncoated material

$am0 := -7.143975261268 \cdot 10^{4}$

$am1 := 6.646546992057 \cdot 10^{4}$

$am2 := 1.719254605608$

fitting parameters for measured luminescence from coated material, taken from SlideWrite program

$Lm(\theta, Ei) := am0 + am1 \cdot (Ei)^{am2}$ measured luminescence from the coated phosphor

The following graph shows the cathodoluminescence intensity as a function of beam energy. The black curve is the uncoated phosphor. The green curve is the measured luminescence from the coated phosphor. The red curve is the luminescence as calculated based on the Rao-Sahib modification of the Bethe stopping power equation. The blue curve is the luminescence based on the new energy loss equation. From the graph, it can be seen that the Rao-Sahib and Wittry equation overestimates the attenuation of the luminescence at low energies. The new energy loss equation accurately predicts the luminescence over the entire energy range up to 4 keV. Measurement of the thickness of the coating on the phosphor is the largest source of error for the calculation. To provide a more accurate analysis, it was assumed that the Rao-Sahib and Wittry equation is valid for the high energy region of the curve. The thickness value was then optimized to give agreement between the calculated and measured curves around 4 keV. For further discussion of this correction, see the discussion of the second model in Chapter 6.

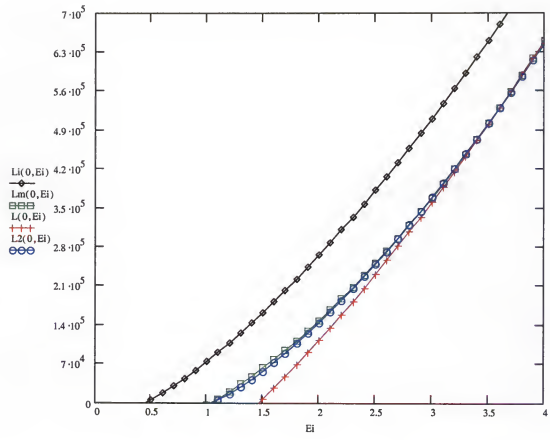


The following is the SlideWrite plot used to determine the curve fiting coefficeints for the measured luminescence from the coated and uncoated phosphor.

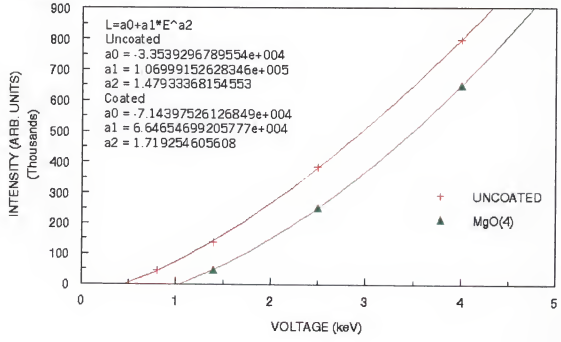

APPENDIX J
MATHCAD PROGRAM FOR MgO (8 min) / $Y_2SiO_5$:Tb

This is a Mathcad program to compute the luminescence as a function of beam energy from a 8 minute coating of MgO on $Y_2SiO_5$:Tb. The coating was applied by pulsed laser deposition.

$t := .043$ thickness in microns of coating at top of particle

$R := 5$ radius of phosphor particle in microns

$\rho := 3.6$ density

$Z := 10$ atomic number

$A := 20.152$ average atomic weight

$\theta := 0, 1 .. 90$ angle from center axis to coating's surface

$$\gamma(\theta) := \operatorname{asin}\left[\frac{(R + t\cdot\cos(\theta\cdot\deg))\ \sin(\theta\cdot\deg)}{R}\right]$$ angle from center axis to phosphor's surface

$r(\theta) := (R)\cdot\sin(\gamma(\theta))$ distance from center axis

$h(\theta) := R\cdot\cos(\gamma(\theta))$ height of phosphor particle

$c(\theta) := (R + t\cdot\cos(\theta\cdot\deg))\cdot\cos(\theta\cdot\deg)$ height of phosphor and coating

$d(\theta) := c(\theta) - h(\theta)$ distance traveled through the coating at given $\theta$

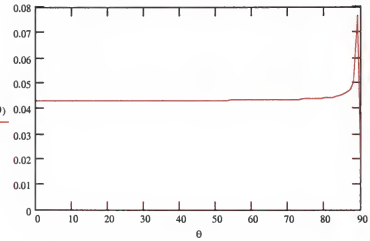


Thickness is nearly constant for all $\theta$, so take $\theta = 0$ for subsequent calculations.

$Ei := 0, .1 .. 4$ incident beam energy

$J := (11.5 \cdot Z) \cdot 10^{-3}$ mean ionization potential in keV

$k := 0.85$ fitting parameter for ionization potential correction

$$J2(Ei) := \frac{J}{1 + k \cdot \left( \frac{J}{Ei + 10^{-50}} \right)}$$ low energy correction of ionization potential

$$D(Ei) := \frac{100 \cdot 1.262 \cdot A \cdot (J2(Ei))^{\frac{1}{2}} \cdot (Ei)^{\frac{3}{2}}}{2355 \cdot \rho \cdot Z}$$ range in bulk of coating material at given incident energy Ei based on Rao-Sahib & Wittry

$D(1.4) = 0.033$

$D(2.5) = 0.079$ range in microns at beam energy (keV) inside brackets

$D(4) = 0.161$

$$E(\theta, Ei) := Ei \cdot \left(1 - \frac{d(\theta)}{D(Ei)}\right)^{\frac{2}{3}}$$ energy after traversing coating from Rao-Sahib & Wittry

$$E2(\theta, Ei) := Ei \cdot \exp\left[-2 \cdot \frac{d(\theta)}{0.064 \cdot (Ei)^{1.36}}\right]$$ fitted energy dependence

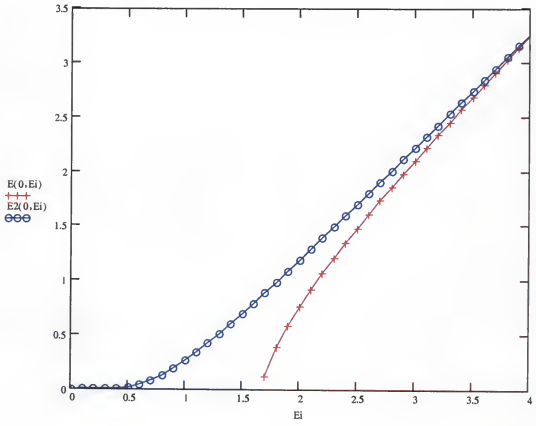


This is a plot of the electron's energy after traveling through the coating as a funciton of incident beam energy. The red curve is based on the calculation using the stopping power equation of Rao-Sahib and Wittry. The blue curve is based on the new fitted energy loss equation.

$a0 := -1.071418066073232 \cdot 10^{4}$

$a1 := 5.318654501167823 \cdot 10^{4}$

$a2 := 1.53937175151185$

fitting coefficients for a power law fit to the uncoated phosphor luminescence, taken from SlideWrite program

$L(\theta, Ei) := a0 + a1 \cdot (E(\theta, Ei))^{a2}$ luminescence of coated material based on Rao-Sahib and Wittry energy loss equation

$L2(\theta, Ei) := a0 + a1 \cdot (E2(\theta, Ei))^{a2}$ luminescence of coated material based on new energy loss equation

$Li(\theta, Ei) := a0 + a1 \cdot (Ei)^{a2}$ luminescence of uncoated material

$am0 := -2.511032772123960 \cdot 10^{4}$

$am1 := 2.053714567936151 \cdot 10^{4}$

$am2 := 2.0320565403483$

fitting parameters for measured luminescence from coated material, taken from SlideWrite program

$Lm(\theta, Ei) := am0 + am1 \cdot (Ei)^{am2}$ measured luminescence from the coated phosphor

The following graph shows the cathodoluminescence intensity as a function of beam energy. The black curve is the uncoated phosphor. The green curve is the measured luminescence from the coated phosphor. The red curve is the luminescence as calculated based on the Rao-Sahib modification of the Bethe stopping power equation. The blue curve is the luminescence based on the new energy loss equation. From the graph, it can be seen that the Rao-Sahib and Wittry equation overestimates the attenuation of the luminescence at low energies. The new energy loss equation accurately predicts the luminescence over the entire energy range up to 4 keV. Measurement of the thickness of the coating on the phosphor is the largest source of error for the calculation. To provide a more accurate analysis, it was assumed that the Rao-Sahib and Wittry equation is valid for the high energy region of the curve. The thickness value was then optimized to give agreement between the calculated and measured curves around 4 keV. For further discussion of this correction, see the discussion of the second model in Chapter 6.

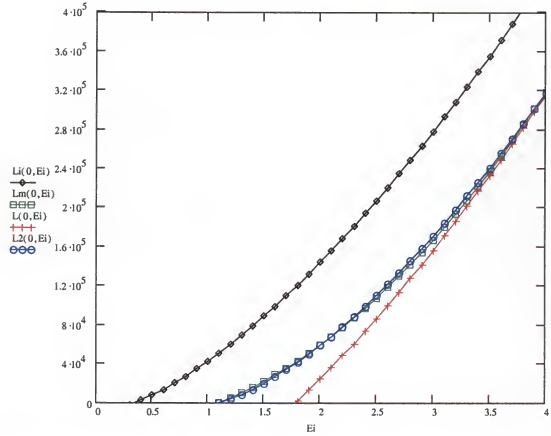


The following is the SlideWrite plot used to determine the curve fiting coefficeints for the measured luminescence from the coated and uncoated phosphor.

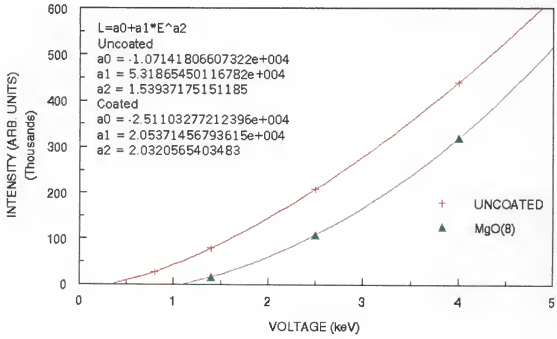

## APPENDIX K
## MATHCAD PROGRAM FOR $Al_2O_3$ (1.2 min) / $Y_2SiO_5$:Tb

This is a Mathcad program to compute the luminescence as a function of beam energy from a 1.2 minute coating of $Al_2O_3$ on $Y_2SiO_5$:Tb. The coating was applied by pulsed laser deposition.

$t := .014$ thickness in microns of coating at top of particle

$R := 5$ radius of phosphor particle in microns

$\rho := 3.97$ density

$Z := 10$ atomic number

$A := 20.3922$ average atomic weight

$\theta := 0, 1 .. 90$ angle from center axis to coating's surface

$$\gamma(\theta) := \operatorname{asin}\left[\frac{(R + t\cdot\cos(\theta\cdot\deg))\,\sin(\theta\cdot\deg)}{R}\right]$$ angle from center axis to phosphor's surface

$r(\theta) := (R)\cdot\sin(\gamma(\theta))$ distance from center axis

$h(\theta) := R\cdot\cos(\gamma(\theta))$ height of phosphor particle

$c(\theta) := (R + t\cdot\cos(\theta\cdot\deg))\cdot\cos(\theta\cdot\deg)$ height of phosphor and coating

$d(\theta) := c(\theta) - h(\theta)$ distance traveled through the coating at given $\theta$

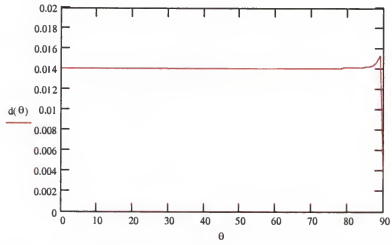


Thickness is nearly constant for all $\theta$, so take $\theta = 0$ for subsequent calculations.

$Ei := 0, .1 .. 4$ incident beam energy

$J := (11.5 \cdot Z) \cdot 10^{-3}$ mean ionization potential in keV

$k := 0.85$ fitting parameter for ionization potential correction

$$J2(Ei) := \frac{J}{1 + k \cdot \left( \frac{J}{Ei + 10^{-50}} \right)}$$ low energy correction of ionization potential

$$D(Ei) := \frac{100 \cdot 1.262 \cdot A \cdot (J2(Ei))^{\frac{1}{2}} \cdot (Ei)^{\frac{3}{2}}}{2355 \cdot \rho \cdot Z}$$ range in bulk of coating material at given incident energy Ei based on Rao-Sahib & Wittry

$D(1.4) = 0.03$

$D(2.5) = 0.072$ range in microns at beam energy (keV) inside brackets

$D(4) = 0.147$

$$E(\theta, Ei) := Ei \cdot \left(1 - \frac{d(\theta)}{D(Ei)}\right)^{\frac{2}{3}}$$ energy after traversing coating from Rao-Sahib & Wittry

$$E2(\theta, Ei) := Ei \cdot \exp\left[-2 \cdot \frac{d(\theta)}{0.064 \cdot (Ei)^{1.36}}\right]$$ fitted energy dependence

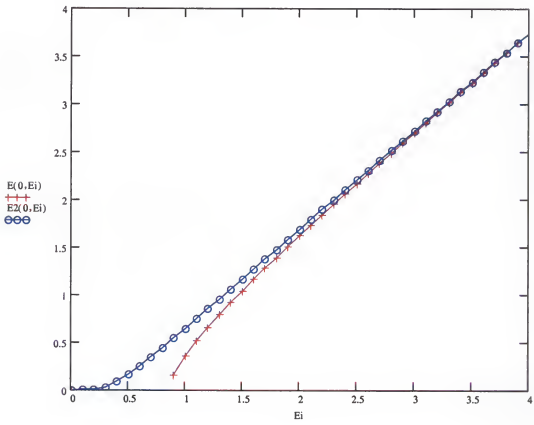


This is a plot of the electron's energy after traveling through the coating as a funciton of incident beam energy. The red curve is based on the calculation using the stopping power equation of Rao-Sahib and Wittry. The blue curve is based on the new fitted energy loss equation.

$a0 := -4.5186519683078 \cdot 10^{3}$

$a1 := 9.615256306005 \cdot 10^{3}$

fitting coefficients for a power law fit to the uncoated phosphor luminescence, taken from SlideWrite program

$a2 := 1.83509379303954$

$L(\theta, Ei) := a0 + a1 \cdot (E(\theta, Ei))^{a2}$ luminescence of coated material based on Rao-Sahib and Wittry energy loss equation

$L2(\theta, Ei) := a0 + a1 \cdot (E2(\theta, Ei))^{a2}$ luminescence of coated material based on new energy loss equation

$Li(\theta, Ei) := a0 + a1 \cdot (Ei)^{a2}$ luminescence of uncoated material

$am0 := -7.73226472803259 \cdot 10^{3}$

$am1 := 6.32789998475401 \cdot 10^{3}$

fitting parameters for measured luminescence from coated material, taken from SlideWrite program

$am2 := 2.0881981625911$

$Lm(\theta, Ei) := am0 + am1 \cdot (Ei)^{am2}$ measured luminescence from the coated phosphor

The following graph shows the cathodoluminescence intensity as a function of beam energy. The black curve is the uncoated phosphor. The green curve is the measured luminescence from the coated phosphor. The red curve is the luminescence as calculated based on the Rao-Sahib modification of the Bethe stopping power equation. The blue curve is the luminescence based on the new energy loss equation. From the graph, it can be seen that the Rao-Sahib and Wittry equation overestimates the attenuation of the luminescence at low energies. The new energy loss equation accurately predicts the luminescence over the entire energy range up to 4 keV. Measurement of the thickness of the coating on the phosphor is the largest source of error for the calculation. To provide a more accurate analysis, it was assumed that the Rao-Sahib and Wittry equation is valid for the high energy region of the curve. The thickness value was then optimized to give agreement between the calculated and measured curves around 4 keV. For further discussion of this correction, see the discussion of the second model in Chapter 6.

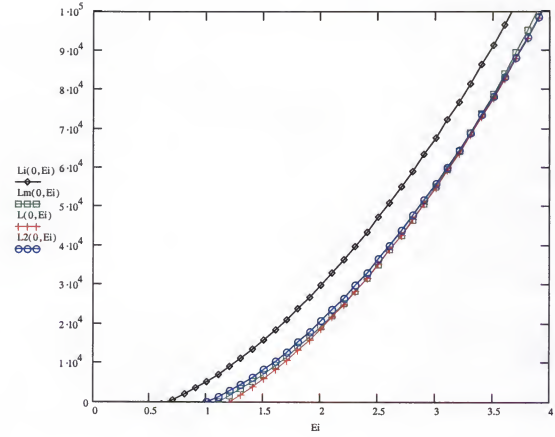


The following is the SlideWrite plot used to determine the curve fiting coefficeints for the measured luminescence from the coated and uncoated phosphor.

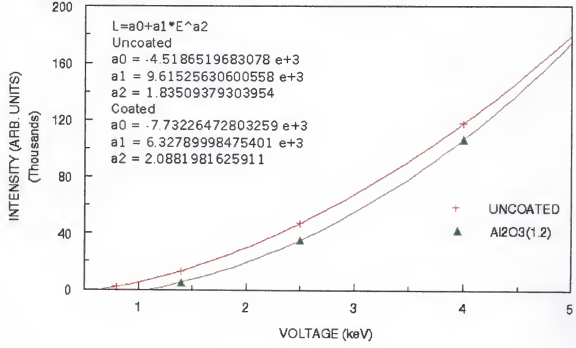

APPENDIX L
MATHCAD PROGRAM FOR $Al_2O_3$ (2.4 min equiv.) / $Y_2SiO_5$:Tb

This is a Mathcad program to compute the luminescence as a function of beam energy from a 2.4 minute equivalent coating of $Al_2O_3$ on $Y_2SiO_5$:Tb. The coating was applied by pulsed laser deposition. The poor accuracy of the calculated luminescence is due to the fitting of the measured luminescence at low voltages.

$t := .051$ thickness in microns of coating at top of particle

$R := 5$ radius of phosphor particle in microns

$\rho := 3.97$ density

$Z := 10$ atomic number

$A := 20.3922$ average atomic weight

$\theta := 0, 1 .. 90$ angle from center axis to coating's surface

$\gamma(\theta) := \text{asin}\left[\frac{(R + t \cdot \cos(\theta \cdot \text{deg}))\ \sin(\theta \cdot \text{deg})}{R}\right]$ angle from center axis to phosphor's surface

$r(\theta) := (R) \cdot \sin(\gamma(\theta))$ distance from center axis

$h(\theta) := R \cdot \cos(\gamma(\theta))$ height of phosphor particle

$c(\theta) := (R + t \cdot \cos(\theta \cdot \text{deg})) \cdot \cos(\theta \cdot \text{deg})$ height of phosphor and coating

$d(\theta) := c(\theta) - h(\theta)$ distance traveled through the coating at given $\theta$

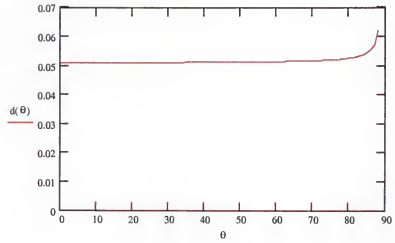


Thickness is nearly constant for all $\theta$, so take $\theta = 0$ for subsequent calculations.

$Ei := 0, .1 .. 4$ incident beam energy

$J := (11.5 \cdot Z) \cdot 10^{-3}$ mean ionization potential in keV

$k := 0.85$ fitting parameter for ionization potential correction

$$J2(Ei) := \frac{J}{1 + k \cdot \left( \frac{J}{Ei + 10^{-50}} \right)}$$ low energy correction of ionization potential

$$D(Ei) := \frac{100 \cdot 1.262 \cdot A \cdot (J2(Ei))^{\frac{1}{2}} \cdot (Ei)^{\frac{3}{2}}}{2355 \cdot \rho \cdot Z}$$ range in bulk of coating material at given incident energy Ei based on Rao-Sahib & Wittry

$D(1.4) = 0.03$

$D(2.5) = 0.072$ range in microns at beam energy (keV) inside brackets

$D(4) = 0.147$

$$E(\theta, Ei) := Ei \cdot \left(1 - \frac{d(\theta)}{D(Ei)}\right)^{\frac{2}{3}}$$ energy after traversing coating from Rao-Sahib & Wittry

$$E2(\theta, Ei) := Ei \cdot \exp\left[-2 \cdot \frac{d(\theta)}{0.064 \cdot (Ei)^{1.36}}\right]$$ fitted energy dependence

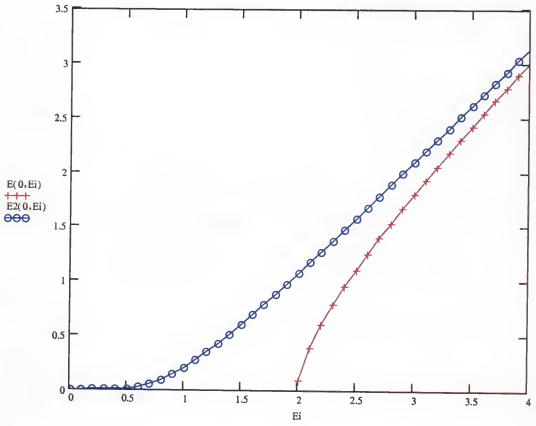


This is a plot of the electron's energy after traveling through the coating as a funciton of incident beam energy. The red curve is based on the calculation using the stopping power equation of Rao-Sahib and Wittry. The blue curve is based on the new fitted energy loss equation.

$a0 := -7.199181492707440^4$

$a1 := 1.387684088007920^5$

fitting coefficients for a power law fit to the uncoated phosphor luminescence, taken from SlideWrite program

$a2 := 1.22985327091371$

$L(\theta, Ei) := a0 + a1 \cdot (E(\theta, Ei))^{a2}$ luminescence of coated material based on Rao-Sahib and Wittry energy loss equation

$L2(\theta, Ei) := a0 + a1 \cdot (E2(\theta, Ei))^{a2}$ luminescence of coated material based on new energy loss equation

$Li(\theta, Ei) := a0 + a1 \cdot (Ei)^{a2}$ luminescence of uncoated material

$am0 := -4.334616588058460^4$

$am1 := 2.642103001733640^4$

fitting parameters for measured luminescence from coated material, taken from SlideWrite program

$am2 := 2.18952712892998$

$Lm(\theta, Ei) := am0 + am1 \cdot (Ei)^{am2}$ measured luminescence from the coated phosphor

The following graph shows the cathodoluminescence intensity as a function of beam energy. The black curve is the uncoated phosphor. The green curve is the measured luminescence from the coated phosphor. The red curve is the luminescence as calculated based on the Rao-Sahib modification of the Bethe stopping power equation. The blue curve is the luminescence based on the new energy loss equation. From the graph, it can be seen that the Rao-Sahib and Wittry equation overestimates the attenuation of the luminescence at low energies. The new energy loss equation accurately predicts the luminescence over the entire energy range up to 4 keV. Measurement of the thickness of the coating on the phosphor is the largest source of error for the calculation. To provide a more accurate analysis, it was assumed that the Rao-Sahib and Wittry equation is valid for the high energy region of the curve. The thickness value was then optimized to give agreement between the calculated and measured curves around 4 keV. For further discussion of this correction, see the discussion of the second model in Chapter 6.

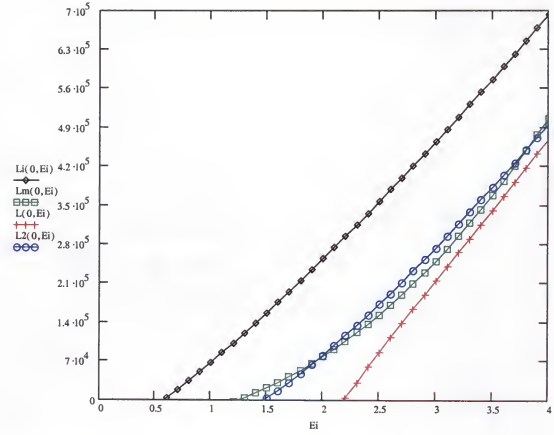


The following is the SlideWrite plot used to determine the curve fiting coefficeints for the measured luminescence from the coated and uncoated phosphor.

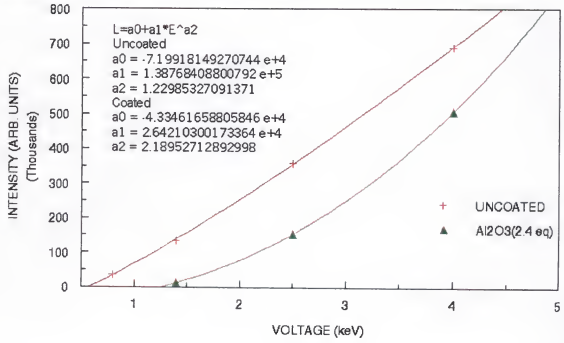

APPENDIX M
MATHCAD PROGRAM FOR $Al_2O_3$ (5 min) / $Y_2SiO_5$:Tb

This is a Mathcad program to compute the luminescence as a function of beam energy from a 5 minute coating of $Al_2O_3$ on $Y_2SiO_5$:Tb. The coating was applied by pulsed laser deposition. Due to the thickness of the coating, no accurate fit could be obtained. However, the following shows a fit based solely on the new energy loss equation.

$t := .23$ thickness in microns of coating at top of particle

$R := 5$ radius of phosphor particle in microns

$\rho := 3.97$ density

$Z := 10$ atomic number

$A := 20.3922$ average atomic weight

$\theta := 0, 1 .. 90$ angle from center axis to coating's surface

$$\gamma(\theta) := \operatorname{asin}\left[\frac{(R + t\cdot\cos(\theta\cdot deg))\,\sin(\theta\cdot deg)}{R}\right]$$ angle from center axis to phosphor's surface

$r(\theta) := (R)\cdot\sin(\gamma(\theta))$ distance from center axis

$h(\theta) := R\cdot\cos(\gamma(\theta))$ height of phosphor particle

$c(\theta) := (R + t\cdot\cos(\theta\cdot deg))\cdot\cos(\theta\cdot deg)$ height of phosphor and coating

$d(\theta) := c(\theta) - h(\theta)$ distance traveled through the coating at given $\theta$

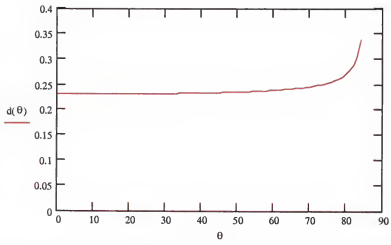


Thickness is nearly constant for all $\theta$, so take $\theta = 0$ for subsequent calculations.

$Ei := 0, .1 .. 4$ incident beam energy

$J := (11.5 \cdot Z) \cdot 10^{-3}$ mean ionization potential in keV

$k := 0.85$ fitting parameter for ionization potential correction

$$J2(Ei) := \frac{J}{1 + k \cdot \left( \frac{J}{Ei + 10^{-50}} \right)}$$ low energy correction of ionization potential

$$D(Ei) := \frac{100 \cdot 1.262 \cdot A \cdot (J2(Ei))^{\frac{1}{2}} \cdot (Ei)^{\frac{3}{2}}}{2355 \cdot \rho \cdot Z}$$ range in bulk of coating material at given incident energy Ei based on Rao-Sahib & Wittry

$D(1.4) = 0.03$

$D(2.5) = 0.072$ range in microns at beam energy (keV) inside brackets

$D(4) = 0.147$

$$E(\theta, Ei) := Ei \cdot \left(1 - \frac{d(\theta)}{D(Ei)}\right)^{\frac{2}{3}}$$

energy after traversing coating from Rao-Sahib & Wittry

$$E2(\theta, Ei) := Ei \cdot \exp\left[-2 \cdot \frac{d(\theta)}{0.064 \cdot (Ei)^{1.36}}\right]$$

fitted energy dependence

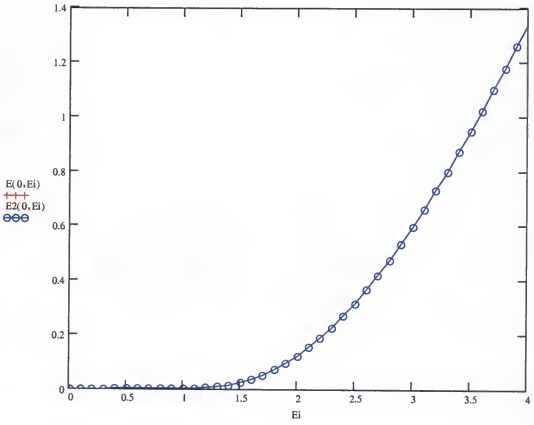


This is a plot of the electron's energy after traveling through the coating as a funciton of incident beam energy. The red curve is based on the calculation using the stopping power equation of Rao-Sahib and Wittry. The blue curve is based on the new fitted energy loss equation.

$a0 := -1.751877451725191 \cdot 10^{3}$

$a1 := 5.745739491515631 \cdot 10^{4}$

fitting coefficients for a power law fit to the uncoated phosphor luminescence, taken from SlideWrite program

$a2 := 1.67325236613149$

$L(\theta, Ei) := a0 + a1 \cdot (E(\theta, Ei))^{a2}$ luminescence of coated material based on Rao-Sahib and Wittry energy loss equation

$L2(\theta, Ei) := a0 + a1 \cdot (E2(\theta, Ei))^{a2}$ luminescence of coated material based on new energy loss equation

$Li(\theta, Ei) := a0 + a1 \cdot (Ei)^{a2}$ luminescence of uncoated material

$am0 := -3.397609887344021 \cdot 10^{2}$

$am1 := 9.224812108440511 \cdot 10^{2}$

fitting parameters for measured luminescence from coated material, taken from SlideWrite program

$am2 := 3.28254555216493$

$Lm(\theta, Ei) := am0 + am1 \cdot (Ei)^{am2}$ measured luminescence from the coated phosphor

The following graph shows the cathodoluminescence intensity as a function of beam energy. The black curve is the uncoated phosphor. The green curve is the measured luminescence from the coated phosphor. The luminescence as calculated based on the Rao-Sahib modification of the Bethe stopping power equation is not present over this energy range. The blue curve is the luminescence based on the new energy loss equation. To find a thickness value for this calculation, the same energy loss equation as in the other fitting programs was used. The thickness was then varied until agreement was obtained between the predicted and measured luminescence from the coated phosphor. Due to the thickness of this coating and the limit of the beam energy imposed by the electron gun, no accurate prediction is possible for this sample.

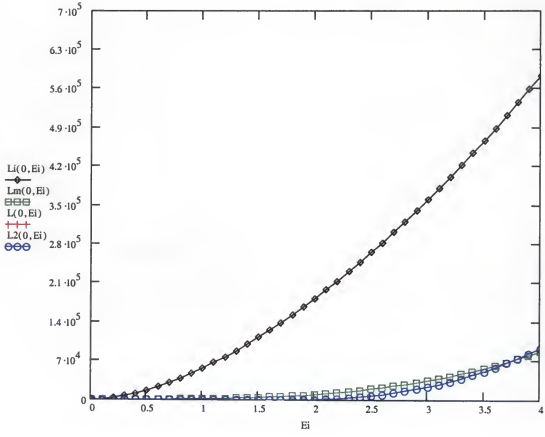


The following is the SlideWrite plot used to determine the curve fiting coefficeints for the measured luminescence from the coated and uncoated phosphor.

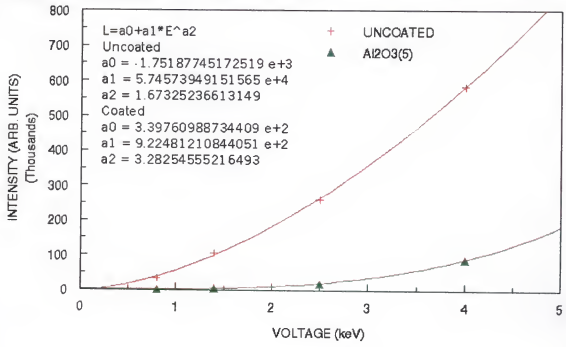

BIBLIOGRAPHY


1 P. Fargis and S. Bykofsky, "The New York Public Library Desk Reference," New York: Webster's New World, p. 836, 1989.

2 M. Leskelä, "Rare Earths in Electroluminescent and Field Emission Display Phosphors," *J. of Alloys and Comp.*, **275-277**, pp. 702-708, 1998.

3 P. H. Holloway, T. A. Trottier, B. Abrams, C. Kondoleon, S. L. Jones, J. S. Sebastian, W. J. Thomes, and H. Swart, "Advances in Field Emission Display Phosphors," *J. Vac. Sci. Tech. B*, **17**, 2, pp. 758-764, 1999.

4 R. L. Fink, Z. L. Tolt, and Z. Yaniv, "The Status and Future of Diamond Thin Film FED," *Surf. and Coat. Tech.*, **108-109**, pp. 570-576, 1998.

5 J. D. Lee, "FPD Market and Technology Trends," *Channel,* **10**, 2, February-March, 1997.

6 C. Curtin and C. Infante, "Fundamentals of Emissive Displays," Candescent Technologies Corp., pp. 1-80, 1997.

7 B. R. Chalamala, Y. Wei, and B. E. Gnade, "FED up with Fat Tubes," in *IEEE Spectrum*, pp. 42-51, April, 1998.

8 J. E. Mancusi, W. D. Palmer, and G. E. McGuire, "Workshop on a Comparative Study of Emerging Inage Display Technologies," MCNC, Research Triangle Park, NC, 1997.

9 K. Tjaden, "CMP in FED Manufacturing," AVS Chemical Mechanical Polishing Workshop, 1996.

10 A. Sobel, "Television's Bright New Technology," in *Scientific American*, pp. 75-77, 1998.

11 H. Yamamoto and S. Okamoto, "The State of the Art of Phosphor Development for Field Emission Displays," *in press*, 1998.

12 J. Ouellette, "Young Researcher Pushes Display Technology," in *The Industrial Physicist*, pp. 12-15, 1999.

13 P. H. Holloway, T. A. Trottier, J. Sebastian, S. Jones, X.-M. Zhang, J.-S. Bang, B. Abrams, W. J. Thomes, and T.-J. Kim, "Degradation of Field Emission Display Phosphors," *J. Appl. Phys.*, **88**, 1, 2000.

14 T. A. Trottier, "Characterization of the Cathodoluminescent Degradation of $Y_2O_2S:Eu^{3+}$ Powder CRT Phosphor," Ph.D. Dissertation, Gainesville, FL: University of Florida, 1997.

15 W. Park, B. K. Wagner, G. Russell, K. Yasuda, C. J. Summers, Y. R. Do, and H. G. Yang, "Enhanced Low Voltage Cathodoluminescence Performance of ZnS Phosphors Coated with $SiO_2$," The Fifth International Conference on the Science and Technology of Display Phosphors, San Diego, California, 1999.

16 C. Dekker, "Carbon Nanotubes as Molecular Quantum Wires," *Physics Today*, **May**, pp. 22-28, 1999.

17 J. Y. Shim, E. J. Chi, H. K. Baik, and K. M. Song, "Field Emission Characteristics of Diamond Films Grown by Electron Assisted Chemical Vapor Deposition," *Thin Solid Films*, **355-356**, pp. 223-228, 1999.

18 B. S. Files and B. M. Mayeaux, "Carbon Nanotubes," in *Advanced Materials & Processes*, vol. 10, pp. 47-49, 1999.

19 P. H. Cutler, J. He, N. M. Miskovsky, T. E. Sullivan, and B. Weiss, "Theory of Electron Emission in High Fields from Atomically Sharp Emitters: Validity of the Fowler-Nordheim Equation," *J. Vac. Sci. Technol. B*, **11**, 2, pp. 387-391, 1993.

20 S. Zimmerman, "Field-Emission Displays," Extended Abstracts from SID, 1997.

21 I. Brodie and C. A. Spindt, *Vacuum Microelectronics*, vol. 83: Academic Press, Inc., 1992.

22 J. B. Hudson, *Surface Science: An Introduction*. Boston, MA: Butterworth-Heinemann, 1992.

23 J. Itoh and S. Kanemaru, "Adding "Intelligence" to Field-Emission Displays," *Information Display*, **8**, pp. 12-14, 1998.

24 B. G. Yacobi and D. B. Holt, *Cathodoluminescence Microscopy of Inorganic Solids*. New York, NY: Plenum Press, 1990.

25 G. Blasse and B. C. Grabmaier, *Luminescent Materials*. Berlin: Springer-Verlag, 1994.

26 E. T. Goldburt, V. A. Bolchouchine, B. N. Levonovitch, and N. P. Sochtine, "Highly Efficient Cathodoluminescent Phosphors and Screens for Mid- and High-Voltage Field Emission Displays," *J. Vac. Sci. Technol. B*, **17**, 2, pp. 765-768, 1999.

27 Y. M. Gueorguiev, D. I. Ivanov, and G. M. Mladenov, "A Program for Monte Carlo Simulation of Penetration and Scattering of Accelerated Electrons in Multicomponent Multilayer Targets," *Vacuum*, **47**, 10, pp. 1227-1230, 1996.

28 T. E. Everhart and P. H. Hoff, "Determination of Kilovolt Electron Energy Dissipation vs Penetration Distance in Solid Materials," *J. Appl. Phys.*, **42**, 13, pp. 5837-5846, 1971.

29 D. C. Joy and S. Luo, "An Empirical Stopping Power Relationship for Low-Energy Electrons," *Scanning*, **11**, pp. 176-180, 1989.

30 T. S. Rao-Sahib and D. B. Wittry, "X-ray Continuum from Thick Elemental Targets for 10-50-keV Electrons," *J. Appl. Phys.*, **45**, 11, pp. 5060-5068, 1974.

31 Z. Czyzewski, D. O. N. MacCallum, A. Romig, and D. C. Joy, "Calculations of Mott Scattering Cross Section," *J. Appl. Phys.*, **68**, 7, pp. 3066-3072, 1990.

32 G. I. Cohn and H. M. Musal, "Transient Response of Phosphors," in *Electron Tubes I*, pp. 825-845, 1956.

33 G. F. J. Garlick, "The Kinetics and Efficiency of Cathodoluminescence," *Brit. J. Appl. Phys.*, **13**, pp. 541-547, 1962.

34 H. W. Leverenz, *An Introduction to Luminescence of Solids*. New York: Dover Publications, 1968.

35 L. Ozawa, *Cathodoluminescence: Theory and Applications*. New York: VCH Publishers, 1990.

36 C. R. Brundle, J. Charles A. Evans, and S. Wilson, *Encyclopedia of Materials Characterization: Surfaces, Interfaces, Thin Films*. Boston: Butterworth-Heinemann, 1992.

37 J. Kramer, "Low Energy Ion-Electron Luminescence: A New Technique for the Excitation of Inorganic Phosphors," *J. Electrochem. Soc.*, **123**, 1, pp. 85-93, 1976.

38 S. M. Jacobsen, C. Stoffers, S. Yang, and C. J. Summers, *Low Voltage Phosphor Data Sheets*, Jan ed. Atlanta, GA: Georgia Institute of Technology, 1996.

39 S. L. Jones, "Enhanced Luminescence from Europium Doped Yttrium Oxide Thin Films Grown via Pulsed Laser Deposition," Ph.D. Dissertation, Gainesville, FL: University of Florida, 1997.

40 R. B. Hunt and R. G. Pappalardo, "Fast Excited-State Relaxation of Eu-Eu Pairs in Commercial $Y_2O_3$:Eu Phosphors," *J. Luminescence*, **34**, pp. 133-146, 1985.

41 K. G. Cho, D. Kumar, S. L. Jones, D. G. Lee, P. H. Holloway, and R. K. Singh, "Growth and Characterization of Eu:$Y_2O_3$ Thin-Film Phosphors on Silicon and Diamond-Coated Silicon Substrates," *J. Electrochem. Soc.*, **145**, 10, pp. 3456-3462, 1998.

42 E. T. Goldburt and R. N. Bhargava, "Doped Semiconductor and Insulator Nanocrystalline Phosphors," Extended Abstracts from the Electrochemical Society Meeting, 1998.

43 M. T. Anderson, M. L. F. Phillips, and R. J. Walko, "Low-Voltage Cathodoluminescent Properties of Europium-Activated Anion-Deficient Fluorites," Mat. Res. Soc. Symp. Proc., 1994.

44 C. R. Ronda, T. Jüstel, and H. Nikol, "Rare Earth Phosphors: Fundamentals and Applications," *J. of Alloys and Comp.*, **275-277**, pp. 669-676, 1998.

45 M. Zachau, "Photocalorimetric Measurement of the Quantum Efficiencies of Phosphors," *J. Luminescence*, **72-74**, pp. 792-793, 1997.

46 Y. C. Kang, I. W. Lenggoro, K. Okuyama, and S. B. Park, "Luminescence Characteristics of $Y_2SiO_5$:Tb Phosphor Particles Directly Prepared by the Spray Pyrolysis Method," *J. Electrochem. Soc.*, **146**, 3, pp. 1227-1230, 1999.

47 E. T. Goldburt and R. N. Bhargava, "Terbium-doped nanocrystalline phosphors," *J. SID*, **4**, 4, pp. 365-369, 1996.

48 X. Ouyang, A. H. Kitai, and R. Siegele, "Rare-Earth-Doped Transparent Yttrium Silicate Thin Film Phosphors for Colour Displays," *Thin Solid Films*, **254**, pp. 268-272, 1995.

49 C. Stoffers, R. Y. Lee, J. Penczek, B. K. Wagner, and C. J. Summers, "Saturation Effects in $Y_2SiO_5$:Tb Under Low-Voltage Excitation," *Appl. Phys. Lett.*, **76**, 8, pp. 949-951, 2000.

50 C. J. Summers, "Phosphors for Flat-Panel Displays," Extended Abstracts from SID, 1997.

51 H. Bechtel, W. Czarnojan, M. Haase, W. Mayr, and H. Nikol, "Phosphor Screens for Flat Cathode Ray Tubes," *Philips Jour. Res.*, **50**, pp. 433-462, 1996.

52 C. H. Seager, W. L. Warren, and D. R. Tallant, "Electron-Beam-Induced-Charging of Phosphors for Low Voltage Display Applications," *J. Appl. Phys.*, **81**, p. 7994, 1997.

53 S. W. Kang and S. H. Kwon, "Photolithographic Patterning of Phosphors Screen by Electrophoretic Deposition for Field Emission Display Application," Seoul National University, Seoul, Korea, 1998 Annual Research Report February 16-17 1998.

54 W. Lehmann, "Particle Size and Efficiency of Electroluminescent Zinc Sulfide Phosphors," *J. Electrochem. Soc.*, **105**, No. 10, pp. 585-588, 1958.

55 E. T. Goldburt, B. Kulkarni, R. N. Bhargava, J. Taylor, and M. Libera, "Size dependent efficiency in Tb doped $Y_2O_3$ Nanocrystalline Phosphor," *J. Luminescence*, **72-74**, pp. 190-192, 1997.

56 S. Fafard, "Quantum Dots: Promise a New Dimension for Semiconductor Lasers," *Photonics Spectra*, pp. 160-164, May, 1997.

57 J. von Behren, T. van Buuren, M. Zacharias, E. H. Chimowitz, and P. M. Fauchet, "Quantum Confinement in Nanoscale Silicon: The Correlation of Size with Bandgap and Luminescence," *Solid State Communications*, **105**, 5, pp. 317-322, 1998.

58 E. T. Goldburt, B. Kulkarni, R. N. Bhargava, J. Taylor, and M. Libera, "Variation of Luminescent Efficiency with Size of Doped Nanocrystalline $Y_2O_3$:Tb Phosphor," *Mat. Res. Soc. Symp.*, **424**, pp. 441-451, 1997.

59 D. Gallagher, W. E. Heady, J. M. Racz, and R. N. Bhargava, "Doped Zinc Sulfide Nanocrystals Precipitated within a Poly(Ethylene Oxide) Matrix - processing and optical characteristics," *J. Crystal Growth*, **138**, pp. 970-975, 1994.

60 R. N. Bhargava, "The Role of Impurity in Doped Nanocrystals," *J. Luminescence*, **72-74**, pp. 46-48, 1997.

61 A. P. Alivisatos, "Electrical Studies of Semiconductor-Nanocrystal Colloids," *MRS Bulletin*, **23**, 2, pp. 18-23, 1998.

62 R. N. Bhargava, D. Gallagher, X. Hong, and A. Nurmikko, "Optical Properties of Manganese-Doped Nanocrystals of ZnS," *Phys. Rev. Lett.*, **72**, 3, pp. 416-419, 1994.

63 J. S. Yoo and J. D. Lee, "The Effects of Particle Size and Surface Recombination Rate on the Brightness of Low-Voltage Phosphor," *J. Appl. Phys.*, **81**, 6, pp. 2810-2813, 1997.

64 R. Bennewitz, D. Smith, M. Reichling, E. Matthias, N. Itoh, and R. M. Wilson, "Electron Stimulated Desorption from $CaF_2$: Penetration Depth of Electrons and Sample Charging," *Nucl. Instr. and Meth. in Phys. Res. B*, **101**, pp. 118-121, 1995.

65 C. H. Seager, "Electric Field Control of Cathodoluminescence from Phosphors Excited at Low Electron Energies," *Appl. Phys. Lett.*, **73**, 1, p. 85, 1998.

66 C. H. Seager, "Electric Field Effects on Phosphor Cathodoluminescence at Low Electron Beam Energies," The Fifth International Conference on the Science and Technology of Display Phosphors, San Diego, California, 1999.

67 J. Cazaux, "Some Considerations on the Electric Field Induced in Insulators by Electron Bombardment," *J. Appl. Phys.*, **59**, p. 1418, 1986.

68 C. G. Pantano, A. S. D'Souza, and A. M. Then, "Electron Beam Damage at Solid Surfaces," in *Beam Effects, Surface Topography, and Depth Profiling in Surface Analysis*, A. W. Czanderna, T. E. Madey, and C. J. Powell, Eds. New York: Plenum Press, 1998.

69 D. J. Griffiths, *Introduction to Electrodynamics*, second ed. Englewood Cliffs: Prentice-Hall, Inc., 1981.

70 J. P. Schaffer, A. Saxena, S. D. Antolovich, T. H. Sanders Jr., and S. B. Warner, *The Science and Design of Engineering Materials*. Chicago: Richard D. Irwin, Inc., 1995.

71 M. Kykta, "Phosphor Requirements for FEDs and CRTs," in *Information Display*, pp. 24-27, 1999.

72 A. G. Chakhovskoi, C. E. Hunt, and M. E. Malinowski, "Gas Desorption Electron Stimulated During Operation of Field Emitter-Phosphor Screen Pairs," *Displays*, **19**, pp. 179-184, 1999.

73 C. E. Hunt and A. G. Chakhovskoi, "Phosphor and Field-Emission Cathode Interactions in Flat-Panel Displays," PTCOE Science and Technology Group Meeting, 1998.

74 C. H. Seager, D. R. Tallant, L. Shea, K. R. Zavadil, B. Gnade, P. H. Holloway, J. S. Bang, X. M. Zhang, A. Vecht, C. S. Gibbons, P. Trwoga, C. Summers, B. Wagner, and J. Penczek, "Influence of Vacuum Environment on the Aging of Phosphors at Low Electron Energies," *J. Vac. Sci. Technol. A*, **17**, 6, pp. 3509-3515, 1999.

75 C. H. Seager, D. R. Tallant, and W. L. Warren, "Cathodoluminescence, Reflectivity Changes, and Accumulation of Graphitic Carbon during Electron Beam Aging of Phosphors," *J. Appl. Phys.*, **82**, 9, p. 4515, 1997.

76 C. A. Kondoleon, "The Effects of Carbon Deposit on Electron Beam Degradation of Oxide Thin Film Phosphors," M.S. Thesis, Gainesville, FL: University of Florida, 1999.

77 D. B. M. Klaassen, D. M. de Leeuw, and T. Welker, "Degradation of Phosphors under Cathode-Ray Excitation," *J. Lumin.*, **37**, pp. 21-28, 1987.

78 J. Sebastian, S. Jones, T. Trottier, H. Swart, and P. Holloway, "Electron-Stimulated Surface Reactions between Residual Vacuum Gas and ZnS Field-Emission-Display Phosphors," *SID*, **27**, pp. 627-630, 1995.

79 S. Itoh, T. Tonegawa, K. Morimoto, and H. Kukimoto, "Surface Analysis of $Zn_{1-x}Cd_xS$ Phosphors Exposed to UV Light Irradiation," *J. Electrochem. Soc.*, **134**, 10, pp. 2628-2631, 1987.

80 H. C. Swart, L. Oosthuizen, P. H. Holloway, and G. L. P. Berning, "Degradation Behaviour of ZnS Phosphor Powders under Different Experimental Conditions," in *Surface and Interface Analysis*, vol. 26: John Wiley & Sons, Ltd., 1998.

81 S. Itoh, T. Kimizuka, and T. Tonegawa, "Degradation Mechanism for Low Voltage Cathodoluminescene of Sulfide Phosphors," *J. Electrochem. Soc.*, **136**, 6, pp. 1819-1823, 1989.

82 H. C. Swart, A. P. Greeff, P. H. Holloway, and G. L. P. Berning, "The Difference in Degredation Behaviour of ZnS:Cu, Al, Au and ZnS:Ag, Cl Phosphor Powders," *Appl. Surf. Sci.*, p. 5468, 1998.

83 Polak, "Electron-Beam-Induced Effects on $CuInS_2$ Surfaces," *Thin Solid Films*, **90**, pp. 345-351, 1982.

84 C. R. Ronda, H. Bechtel, U. Kynast, and T. Welker, "The Degradation Behaviour of LaOBr:Tb under Cathode-Ray Excitation," *J. Appl. Phys.*, **75**, 9, pp. 4636-4641, 1994.

85 H. Bechtel, "Phosphor Degradation under Electron Excitation with Varying Anode Voltage," The First International Conference on the Science and Technology of Display Phosphors, 1995.

86 A. Vecht, "Seminar of Phosphor Aging," Extended Abstracts from SID, 1996.

87 P. R. Schwoebel, "Lifetime Extension of Cathodoluminescent Phosphors," SRI International, Menlo Park, CA 1996.

88 H. Bechtel, W. Czarnojan, M. Haase, and D. Wadow, "Phosphor Degradation under Electron Excitation with Varying Anode Voltage," *J. SID*, **4**, 3, pp. 219-222, 1996.

89 R. Cappels and T. La, "The Hue Shift in Color CRTs with Lifetime: Causes and Corrections," *SID Digest*, **38**, 3, pp. 875-878, 1996.

90 S. Itoh, H. Toki, Y. Sato, K. Morimoto, and T. Kishino, "The $ZnGa_2O_4$ Phosphor for Low-Voltage Blue Cathodoluminescence," *J. Electrochem. Soc.*, **138**, 5, pp. 1509-1512, 1991.

91 S. Itoh, T. Watanabe, T. Yamaura, and K. Yano, "A Challenge to Field Emission Displays," Asia Display, Fifteenth International Display Research Conference, Hamamatsu, Japan, 1995.

92 A. Vecht, C. Gibbons, D. Davies, X. Jing, P. Marsh, T. Ireland, J. Silver, A. Newport, and D. Barber, "Engineering Phosphors for Field Emission Displays," *J. Vac. Sci. Technol. B*, **17**, 2, pp. 750-757, 1999.

93 B. K. Wagner, "Current Status of FED Phosphors," The Fifth International Conference of the Science and Technology of Display Phosphors, San Diego, California, 1999.

94 B. R. Chalamala, "The Physics of Gaseous Exposures on Active Field Emission Microcathode Arrays," Ph.D. Dissertation, Denton, Texas: University of North Texas, 1996.

95 Y.-S. Fran and T.-Y. Tseng, "Preparation of Aluminum Film on Phosphor Screen for Field Emission Display," *Mater. Chem. and Phys.*, **61**, pp. 166-168, 1999.

96 J. D. Kingsley and J. S. Prener, "Voltage Dependence of Cathode-Ray Efficiency of Phosphors: Phosphor Particles with Nonluminescent Coatings," *J. Appl. Phys.*, **43**, 7, pp. 3073-3079, 1972.

97 H. Bechtel, W. Czarnojan, W. Mayr, and H. Nikol, "Life Performance of Color Phosphor Screens for Flat Cathode-Ray Displays," Extended Abstracts from SID, 1997.

98 A. O. Dmitrienko, B. I. Gorfinkel, V. V. Mikhailova, I. V. Burmatova, and J. M. Kim, "RGB Phosphors for FED: Surface Properties and Low-Energy Cathodoluminescence," presented at IVMC, Kyongju, Korea, 1997.

99 J. M. Fitz-Gerald, T. A. Trottier, R. K. Singh, and P. H. Holloway, "Significant Reduction of Cathodoluminescent Degradation in Sulfide-Based Phosphors," *Appl. Phys. Lett.*, **72**, 15, pp. 1838-1839, 1998.

100 S.-H. Yang and M. Yokoyama, "Blue $Cu_xS$ Coated ZnS:Ag,Cl Phosphor as Potential Field Emission Display Material," *J. Vac. Sci. Tech. A*, **16**, 6, p. 3443, 1997.

101 A. O. Dmitrienko, V. Y. Filipchenko, B. I. Gorfinkel, and S. L. Shmakov, "Luminous Efficiency of Phosphors Excited by Low-Engergy Electrons in Vacuum Fluorescent Displays and Field Emission Displays," International Display Research Conf., 1993.

102 H. Kominami, T. Nakamura, K. Sowa, Y. Nakanishi, Y. Hatanaka, and G. Shimaoka, "Low Voltage Cathodoluminescent Properties of Phosphors Coated with $In_2O_3$ by sol-gel method," *Appl. Surf. Sci.*, **113/114**, pp.519-522, 1997.

103 G. R. Villalobos, J. S. Sanghera, S. S. Bayya, and I. D. Aggarwal, "ZnS:Ag Phosphors Coated with $SiO_2$ Film Showing Improved Efficiency and Aging Behavior," The Fifth International Conference on the Science and Technology of Display Phosphors, San Diego, California, 1999.

104 B. K. Wagner, F. Zhang, Y. Jiang, P. A. Manigault, G. Russell, and C. J. Summers, "Development of Low-Voltage Phosphors for Field Emission Displays," Phosphor Technology Center of Excellence, Atlanta, GA, 23rd Quarter Report Feb. 4 - May 3 1999.

105 S. Itoh, T. Tonegawa, T. L. Pykosz, K. Morimoto, and H. Kukimoto, "Influence of Grinding and Baking Processes on the Luminescent Properties of Zinc Cadmium Sulfide Phosphors for Vacuum Fluorescent Displays," *J. Electrochem. Soc.*, **134**, 12, pp. 3178-3181, 1987.

106 S. M. Jacobsen, S. Yang, F. L. Zhang, and C. J. Summers, "Improved Performance of Low-Voltage Phosphors for Field-Emission Displays," *SID 95 Digest*, pp. 631-633, 1995.

107 J. H. Gwak, S. H. Park, J. E. Jang, Y. W. Jin, S. J. Lee, N. S. Lee, J. E. Jung, J. M. Kim, V. A. Vorobyov, and E. G. Morozov, "Cathodoluminescence of Surface-Treated $Y_2O_3$:$Eu^{3+}$ Phosphor Before and After Screening for FED Applications," The Fifth International Conference on the Science and Technology of Display Phosphors, San Diego, California, 1999.

108 E. Agostinelli, S. Alessandrini, D. Fiorani, A. G. Santiago, A. M. Testa, M. Angiolini, and M. Vittori-Antisari, "Structural and Magnetic Properties of Granular Co-Ag Thin Films Depostied by Pulsed Laser Deposition," *NanoStructured Materials*, **10**, 2, pp. 217-233, 1998.

109 D. Kumar, R. K. Singh, and J. Fitz-Gerald, "Synthesis of High-Temperature Superconductive and Colossal Magnetoresistive Surfaces of Insulating Particles," *Appl. Phys. Lett*, **72**, 12, pp. 1451-1453, 1998.

110 D. H. Lowndes, D. B. Geohegan, A. A. Puretzky, D. P. Norton, and C. M. Rouleau, "Synthesis of Novel Thin-Film Materials by Pulsed Laser Deposition," *Science*, **273**, 16 August, pp. 898-903, 1996.

111 J. M. Fitz-Gerald, "Synthesis and Characterization of Engineered Particles with Controlled Surace Architecture," Ph.D. Dissertation, Gainesville, FL: University of Florida, 1998.

112 S. J. Guilfoyle, M. D. Crapper, M. Lovelady, and M. Petty, "Modelling of Pulsed Laser Deposition of Large Area Films," *J. Magnetism and Magnetic Mater.*, **198-199**, pp. 113-115, 1999.

113 H. S. Kwok, X. W. Sun, and D. H. Kim, "Pulsed Laser Deposited Crystalline Ultrathin Indium Tin Oxide Films and Their Conduction Mechanisms," *Thin Solid Films*, **335**, pp. 299-302, 1998.

114 C. N. Afonso and J. Gonzalo, "Pulsed Laser Deposition fo Thin Films for Optical Applications," *Nuclear Instr. and Methods in Phys. Res. B*, **116**, pp. 404-409, 1996.

115 P. H. Holloway and S. L. Jones, "Nanostructure Effects in Luminescent Materials," *J. Surface Analysis*, **3**, No. 2, pp. 226-231, 1998.

116 T. Koyama, S. Ohtsuka, H. Nagata, and S. Tanaka, "Fabrication of microcrystallites of II-VI compound semiconductors by laser ablation method," *J. Crystal Growth*, **117**, pp. 156-160, 1992.

117 M. E. Taylor and H. A. Atwater, "Monte Carlo Simulations of Epitaxial Growth: Comparison of Pulsed Laser Deposition and Molecular Beam Epitaxy," *Appl. Surf. Sci.*, **127-129**, pp. 159-163, 1998.

118 K. G. Cho, D. Kumar, D. G. Lee, S. L. Jones, P. H. Holloway, and R. K. Singh, "Improved Luminescence Properties of Pulsed Laser Deposited Eu:$Y_2O_3$ Thin Films on Diamond Coated Silicon Substrates," *Appl. Phys. Lett.*, **71**, 23, pp. 3335-3337, 1997.

119 K. G. Cho, D. Kumar, P. H. Holloway, and R. K. Singh, "Luminescence Behavior of Pulsed Laser Deposited Eu:$Y_2O_3$ Thin Film Phosphors on Sapphire Substrates," *Appl. Phys. Lett.*, **73**, 21, pp. 3058-3060, 1998.

120 H.-J. Gao, D. Kumar, K. G. Cho, P. H. Holloway, R. K. Singh, X. D. Fan, Y. Yan, and S. J. Pennycook, "Epitaxial Growth of $Y_2O_3$:Eu Thin Films on $LaAlO_3$," *Appl. Phys. Lett.*, **75**, 15, pp. 2223-2225, 1999.

121 J. M. Fitz-Gerald, R. K. Singh, H. Gao, D. Wright, M. Ollinger, J. W. Marcinka, and S. J. Pennycook, "Novel Method for the Synthesis of Thin Film Coatings on Particulate Materials," *J. Mater. Res.*, **14**, 8, pp. 3281-3291, 1999.

122 J. M. Fitz-Gerald, P. D. Rack, T. A. Trottier, M. Ollinger, S. J. Pennycook, H. Gao, and R. K. Singh, "Synthesis of Spherical Luminescent Particulate Coatings," *J. Appl. Phys.*, **86**, 3, pp. 1759-1761, 1999.

123 J. Fitz-Gerald, S. Pennycook, H. Gao, and R. K. Singh, "Synthesis and Properties of Nanofunctionalized Particulate Materials," *Nanostructured Materials*, **12**, 8, pp. 1167-1171, 1999.

124 D. Kumar, K. G. Cho, Z. Chen, V. Craciun, P. H. Holloway, and R. K. Singh, "Cathodoluminescent Properties of Pulsed Laser Deposited Eu-Activated $Y_2O_3$ Epitaxial Films," *Physical Review B*, **60**, 19, pp.13331-13334, 1999.

125 J. T. Cheung, in *Pulsed Laser Deposition of Thin Films*, D. Crisey and G. K. Hubler, Eds. New York, NY: John Wiley and Sons, 1994.

126 M. Ohring, *The Materials Science of Thin Films.* Boston: Academic Press, Inc., 1992.

127 J. H. Simmons and K. S. Potter, *Optical Materials.* San Diego, CA: Academic, 2000.

128 Gaertner Scientific Corporation, *Ellipsometer Operating Instructions*, 1968.

129 R. M. A. Azzam and N. M. Bashara, *Ellipsometry and Polarized Light.* Amsterdam: North-Holland, 1989.

130 Y.-H. Tseng, B.-S. Chiou, C.-C. Peng, and L. Ozawa, "Spectral Properties of $Eu^{3+}$-Activated Yttrium Oxysulfide Red Phosphor," *Thin Solid Films*, **330**, pp. 173-177, 1998.

131 M. Kotera, K. Murata, and K. Nagami, "Monte Carlo Simulation of 1-10-KeV Electron Scattering in a Gold Target," *J. Appl. Phys.*, **52**, 2, pp. 997-1003, 1981.

132 D. D. C. Joy, "Monte Carlo Simulations of Electron Beam - Solid Interactions," Programs for MS-DOS machines, 1997.

133 K. Kanda, "Windows based Monte Carlo Simulations," vol. 1999: downloaded from http://www.nsctoronto.com/joy_se/, 1998.

134 S. Larach and A. E. Hardy, "Cathode-Ray-Tube Phosphors:Principles and Applications," *Proceedings of the IEEE*, **61**, 7, pp. 915-926, 1973.

135 P. A. Tipler, *College Physics.* New York, NY: Worth Publishers, Inc., 1987.

136 R. E. Hummel, *Electronic Properties of Materials.* Second Edition, New York, NY: Springer-Verlag, 1993.

137 R. Browning, T. Z. Li, B. Chui, J. Ye, R. F. W. Pease, Z. Czyzewski, and D. C. Joy, "Empirical Forms for the Electron/Atom Elastic Scattering Cross Sections from 0.1 to 30 keV," *J. Appl. Phys.*, **76**, 4, pp. 2016-2022, 1994.

## BIOGRAPHICAL SKETCH

William Joseph Thomes, Jr. was born on July 21, 1974, in Richmond, Virginia. He attended John Randolph Tucker High School, where he graduated with honors in 1992. The next four years were spent at the College of William and Mary in Williamsburg, Virginia, where he obtained his Bachelor of Science degree in physics and mathematics. His senior thesis, entitled "Development of a Small Scale Gridded Energy Analyzer," was awarded honors by the Physics department. Upon completion of his undergraduate education in May 1996, he came to the University of Florida to study under the guidance of Dr. Paul Holloway. The next several years were spent learning about the field of Materials Science. He received his Master of Science degree in May 1999. That summer, he traveled to Albuquerque, New Mexico to do collaborative research with Dr. Carl Seager and Dr. Dave Tallant at Sandia National Laboratories.

I certify that I have read this study and that in my opinion it conforms to acceptable standards of scholarly presentation and is fully adequate, in scope and quality, as a dissertation for the degree of Doctor of Philosophy.

Paul H. Holloway, Chairman
Professor of Materials Science and Engineering

I certify that I have read this study and that in my opinion it conforms to acceptable standards of scholarly presentation and is fully adequate, in scope and quality, as a dissertation for the degree of Doctor of Philosophy.

Joseph H. Simmons
Professor of Materials Science and Engineering

I certify that I have read this study and that in my opinion it conforms to acceptable standards of scholarly presentation and is fully adequate, in scope and quality, as a dissertation for the degree of Doctor of Philosophy.

Rajiv K. Singh
Professor of Materials Science and Engineering

I certify that I have read this study and that in my opinion it conforms to acceptable standards of scholarly presentation and is fully adequate, in scope and quality, as a dissertation for the degree of Doctor of Philosophy.

Rolf E. Hummel
Professor of Materials Science and Engineering

I certify that I have read this study and that in my opinion it conforms to acceptable standards of scholarly presentation and is fully adequate, in scope and quality, as a dissertation for the degree of Doctor of Philosophy.

Fred Sharifi
Associate Professor of Physics

This dissertation was submitted to the Graduate Faculty of the College of Engineering and to the Graduate School and was accepted as partial fulfillment of the requirements for the degree of Doctor of Philosophy.

August 2000

M. J. Ohanian
Dean, College of Engineering

Winfred M. Phillips
Dean, Graduate School

LD
1780
2000
.T465

UNIVERSITY OF FLORIDA

3 1262 08555 1801